

École doctorale n° 364 : Sciences Fondamentales et Appliquées

Doctorat ParisTech

THÈSE

pour obtenir le grade de docteur délivré par

l'École Nationale Supérieure des Mines de Paris

Spécialité doctorale “Science et Génie des Matériaux”

présentée et soutenue publiquement par

Ali SAAD

le DAY MONTH 2015

NUMERICAL MODELLING OF MACROSEGREGATION FORMED DURING SOLIDIFICATION WITH SHRINKAGE USING A LEVEL SET APPROACH

Directeurs de thèse: **Michel BELLET**
Charles-André GANDIN

Jury

M. jury 1,	affiliation	Rapporteur
M. jury 2,	affiliation	Rapporteur
M. jury 3,	affiliation	Examinateur
M. jury 4,	affiliation	Examinateur
M. jury 5,	affiliation	Examinateur

T
H
E
S
S
E

MINES ParisTech

Centre de Mise en Forme des Matériaux (CEMEF)
UMR CNRS 7635, F-06904 Sophia Antipolis, France

Acknowledgement

Dedicated to humanity ...

Contents

1 General Introduction	1
1.1 Solidification notions	2
1.1.1 Solute partitioning	2
1.1.2 Dendritic growth	4
1.1.3 Mush permeability	6
1.2 Macrosegregation	7
1.2.1 Liquid thermosolutal convection	8
1.2.2 Solidification shrinkage	9
1.2.3 Movement of equiaxed grains	9
1.2.4 Solid deformation	9
1.3 Other defects	9
1.4 Industrial Worries	11
1.5 Project context and objectives	12
1.5.1 Context	12
1.5.2 Objectives and outline	14
2 Modelling Review	19
2.1 Modelling macrosegregation	20
2.1.1 Macroscopic solidification model: monodomain	21
2.2 Eulerian and Lagrangian motion description	27
2.2.1 Overview	27
2.2.2 Interface capturing	30
2.3 Solidification models with level set	30
2.4 The level set method	31
2.4.1 Diffuse interface	32
2.4.2 Mixing Laws	34
2.5 Interface motion	35
2.5.1 Level set transport	36

Contents

2.5.2	Level set regularisation	37
2.6	Mesh adaptation	41
2.6.1	Metrics and anisotropy	41
2.6.2	<i>Remesh2</i> : Interface remeshing	43
2.6.3	<i>Remesh4</i> : Multi-criteria remeshing	44
3	Energy balance with thermodynamic tabulations	47
3.1	State of the art	48
3.2	Thermodynamic considerations	49
3.2.1	Volume averaging	49
3.2.2	The temperature-enthalpy relationship	50
3.2.3	Tabulation of properties	50
3.3	Numerical method	52
3.3.1	Enthalpy-based approach	56
3.3.2	Temperature-based approach	56
3.3.3	Convergence	57
3.4	Validation	58
3.5	Application: multicomponent alloy solidification	61
3.5.1	Tabulations	63
3.5.2	Discussion	65
3.6	Limitations	70
4	Macrosegregation with liquid metal motion	73
4.1	Introduction	75
4.2	Formulation stability	75
4.2.1	Stable mixed finite elements	76
4.2.2	Variational multiscale (VMS)	76
4.3	Navier-Stokes solver	77
4.3.1	Strong and weak formulations	77
4.3.2	Stabilisation parameters	81
4.3.3	Implementation	82
4.4	Application to multicomponent alloys	83
4.4.1	<i>Tsolver</i> validation with fluid flow	83
4.4.2	Results	86
4.5	Macroscopic prediction of channel segregates	92
4.5.1	Introduction	92
4.5.2	Experimental work	93
4.5.3	Macroscopic scale simulations	93

4.6 Meso-Macro prediction of channel segregates	102
4.6.1 Numerical method	102
4.6.2 Configuration	103
4.6.3 Effect of vertical temperature gradient	107
4.6.4 Effect of cooling rate	109
4.6.5 Effect of lateral temperature gradient	111
4.6.6 Mono-grain freckles	112
5 Macrosegregation with solidification shrinkage	115
5.1 Solidification shrinkage	117
5.2 Choice of boundary tracking	117
5.3 Multidomain formalism	119
5.3.1 Assumptions	121
5.4 FE partitioned model	122
5.4.1 In the metal	122
5.4.2 In the air	126
5.5 FE monolithic model	128
5.5.1 Monolithic equations	128
5.6 1D application: solidification with inverse segregation	133
5.6.1 Geometry and boundary conditions	133
5.6.2 Shrinkage without macrosegregation	133
5.6.3 Shrinkage with macrosegregation	143
5.7 2D application: controlled solidification benchmark	153
5.7.1 Boundary condition effect	153
5.7.2 Computational configuration	155
5.7.3 Results	156
5.8 3D application: reduced-gravity solidification	161
5.8.1 Previous work	161
5.8.2 Computational configuration	164
5.8.3 Texus binary alloy	171
5.8.4 Texus ternary and quaternary alloys	179
Bibliography	185

Contents

List of Acronyms

Acronym	Standing for
ALE	Arbitrary Lagrangian-Eulerian
BTR	Brittle temperature range
CAFD	Cellular Automata Finite Difference
CAFE	Cellular Automata Finite Element
CBB	Circumventing Babuška-Brezzi
CCEMLCC	Chill Cooling for the Electro-Magnetic Levitator in relation with Continuous Casting of steel
CEMEF	Centre de Mise en Forme des Matériaux
CFL	Courant–Friedrichs–Lewy
C.FL.	Computing and FLuids
CSF	Continuum Surface Force
DLR	Deutsches Zentrum für Luft- und Raumfahrt
DSPG	Darcy-Stabilising/Petrov-Galerkin
EML	Electromagnetic levitation
ESA	European Space Agency
FEM	Finite Element Method
FVM	Finite Volume Method
GMAW	Gas Metal Arc Welding
ISS	International Space Station
IWT	Institut für Werkstofftechnik
LHS	Left-hand side
LSIC	Least squares on incompressibility constraint
LSM	Level set method
MAC	Marker-and-cell
PF	Phase field
PSPG	Pressure-Stabilising/Petrov-Galerkin
RHS	Right-hand side
RUB	Ruhr Universität Bochum
RVE	Representative Elementary Volume
SBB	Satisfying Babuška-Brezzi
SUPG	Streamline-Upwind/Petrov-Galerkin
VMS	Variational MultiScale
VOF	Volume Of Fluid

Contents

Contents

Chapter 2

Modelling Review

Contents

2.1 Modelling macrosegregation	20
2.1.1 Macroscopic solidification model: monodomain	21
2.2 Eulerian and Lagrangian motion description	27
2.2.1 Overview	27
2.2.2 Interface capturing	30
2.3 Solidification models with level set	30
2.4 The level set method	31
2.4.1 Diffuse interface	32
2.4.2 Mixing Laws	34
2.5 Interface motion	35
2.5.1 Level set transport	36
2.5.2 Level set regularisation	37
2.6 Mesh adaptation	41
2.6.1 Metrics and anisotropy	41
2.6.2 <i>Remesh2</i> : Interface remeshing	43
2.6.3 <i>Remesh4</i> : Multi-criteria remeshing	44

2.1 Modelling macrosegregation

Microsegregation models

Solid formation depends greatly on the ability of chemicals species to diffuse within each of the solid and liquid phases, but also across the solid-liquid interface. Furthermore, chemical diffusion like all other diffusional processes, is a time-dependent phenomenon. One can thus conclude that two factors influence the amount of solid formation: cooling rate and diffusion coefficients. However, convection and other mechanical mixing sources, homogenise the composition much faster than atomic diffusion. As such, *complete mixing* in the liquid is always an acceptable assumption, regardless of the solidification time. Thus, we speak of infinite diffusion in the liquid. Nevertheless, diffusion in the solid, also known as *back diffusion*, is the only transport mechanism with very low diffusion coefficients. Therefore, chemical species require a long time, i.e. low cooling rate, to completely diffuse within the solid. The difference in diffusional behaviour at the scale of a secondary dendrite arm, is summarised by two limiting segregation models of perfect equilibrium and nonequilibrium, which are the lever rule and Gulliver-Scheil models, respectively. Afterwards, models with finite back diffusion are presented.

Lever rule

The lever rule considers an ideal equilibrium in all phases, i.e. solidification is extremely slow, hence phase compositions are homogeneous ($w^{l*} = w^l$ and $w^{s*} = w^s$) at all times as a consequence of complete mixing. These compositions are given by:

$$w^l = w^{l*} = k^{-1}w^{s*} = k^{-1}w^s \quad (2.1)$$

$$w^s = w^{s*} = \frac{kw_0}{kf^s + (1 - f^s)} \quad (2.2)$$

At the end of solidification, the composition of the solid phase is equal to the nominal composition, $w^s = w_0$.

Gulliver-Scheil

The other limiting case is the absence of diffusion in the solid. That includes also the diffusion at the interface, so nothing diffuses in or out. The consequence is a steady increase of the homogeneous liquid composition while the solid composition remains non-uniform. Compared to a full equilibrium approach, higher fractions of liquid will remain. In eutectic systems, liquid may exist until eutectic composition is reached,

triggering a eutectic solidification. The phase compositions with this approach are given by:

$$w^l = w^{l*} = k^{-1}w^{s*} \quad (2.3)$$

$$w^{s*} = kw_0(1 - f^s)^{k-1} \quad (2.4)$$

Finite back diffusion

It has been concluded that the assumption of a negligable back diffusion overestimates the liquid composition and the resulting eutectic fraction. Therefore, many models studied the limited diffusion in the solid. One of the earliest models is the Brody-Flemings models [Khan et al. 2014] that is based on a differential solute balance equation for a parabolic growth rate, as follows:

$$w^l = w^{l*} = k^{-1}w^{s*} \quad (2.5)$$

$$w^{s*} = kw_0 [1 - (1 - 2\text{Fo}^s k) f^s]^{\frac{k-1}{1-2\text{Fo}^s k}} \quad (2.6)$$

where Fo^s is the dimensionless *Fourier number* for diffusion in the solid [Dantzig and Rappaz 2009]. It depends on the solid diffusion coefficient D^s , solidification time t_s and the secondary dendrite arm spacing, as follows:

$$\text{Fo}^s = \frac{D^s t_s}{(\lambda_2/2)^2} \quad (2.7)$$

Several other models were since suggested and used. The interested reader is referred to the following non exhaustive list of publications: Clyne and Kurz [1981], Kobayashi [1988], Ni and Beckermann [1991], Wang and Beckermann [1993], Combeau et al. [1996], Martorano et al. [2003], and Tourret and Gandin [2009]. It is noted that some of these publications consider also a finite diffusion in the liquid phase.

2.1.1 Macroscopic solidification model: monodomain

In this section, we will present the macroscopic conservations equations that enable us to predict macrosegregation in single multiphase metal system.

Volume averaging

It is crucial for a solidification model to represent phenomena on the microscale, then scale up to predict macroscopic phenomena. Nevertheless, the characteristic length of a small scale in solidification may represent a dendrite arm spacing, for instance

the mushy zone permeability, as it may also represent an atomic distance if one is interested, for instance, in the growth competition between diffusion and surface energy of the solid-liquid interface.

Modelling infinitely small-scale phenomena could be prohibitively expensive in computation time, if we target industrial scales. The volume averaging is a technique that allows bypassing this barrier by averaging small-scale variations on a so-called *representative volume element* (RVE) [Dantzig and Rappaz 2009] of volume V_E , with the following dimensional constraints: the element should be large enough to "see" and average microscopic fluctuations whilst being smaller than the scale of macroscopic variations.

Solid and liquid may exist simultaneously in the RVE, but no gas phase is considered (volume saturation: $V^s + V^l = V_E$). Moreover, temperature is assumed uniform and equal for all the phases. The formalism, introduced by Ni and Beckermann [1991], is summarised by the following equations for any physical quantity ψ :

$$\langle \psi \rangle = \frac{1}{V_E} \int_{V_E} \psi \, d\Omega = \langle \psi^s \rangle + \langle \psi^l \rangle \quad (2.8)$$

where $\langle \psi \rangle^s$ and $\langle \psi \rangle^l$ are phase averages of ψ . Then, for any phase ϕ , one can introduce the *phase intrinsic average* of ψ , denoted $\langle \psi \rangle^\phi$, by writing:

$$\langle \psi^\phi \rangle = \frac{1}{V_E} \int_{V^\phi} \psi \, d\Omega = g^\phi \langle \psi \rangle^\phi \quad (2.9)$$

where g^ϕ is the volume fraction of phase ϕ with $g^\phi = V_\phi/V_E$. To finalize, the averaging is applied to temporal and spatial derivation operators:

$$\left\langle \frac{\partial \psi^\phi}{\partial t} \right\rangle = \frac{\partial \langle \psi^\phi \rangle}{\partial t} - \int_{\Gamma^*} \psi^\phi \mathbf{v}^* \cdot \mathbf{n}^\phi \, dA \quad (2.10)$$

$$\left\langle \nabla \cdot \psi^\phi \right\rangle = \nabla \cdot \langle \psi^\phi \rangle + \int_{\Gamma^*} \psi^\phi \cdot \mathbf{n}^\phi \, dA \quad (2.11)$$

where \mathbf{v}^* is the local relative interface velocity and Γ^* is the solid-liquid interface, while \mathbf{n}^ϕ is the normal to Γ^* , directed outwards. The surface integral terms in eqs. (2.10) and (2.11) are *interfacial averages* that express exchanges between the phases across the interface.

The previous equations will be used to derive a set macroscopic conservation equations. It is noted that the intrinsic average $\langle \psi \rangle^\phi$ may be replaced by ψ^ϕ for notation simplicity, whenever the averaging technique applies.

Macroscopic equations

A monodomain macroscopic model relies on four main conservation equations to predict macrosegregation in a single alloy without any solidification shrinkage. It follows that no ambient gas will be taken into account. To determine an general averaged macroscopic equation, we must write a phase-averaged conservation equation, for any physical quantity ψ :

$$\left\langle \frac{\partial \psi^\phi}{\partial t} \right\rangle + \left\langle \nabla \cdot \psi^\phi \mathbf{v}^\phi \right\rangle + \left\langle \nabla \cdot \mathbf{j}_{\psi^\phi} \right\rangle = \left\langle Q_{\psi^\phi} \right\rangle \quad (2.12)$$

The first LHS term in eq. (2.12) represents the time variation of ψ , the second term accounts for transport by advection while the third term accounts for diffusive transport of ψ , knowing its flux, \mathbf{j}_ψ . The RHS term represents a volumetric source. The considered equations are mass, energy, species conservation and momentum. The latter equation is averaged only for the liquid phase, as we assume a fixed and rigid solid phase ($\mathbf{v}^s = 0$), thus the corresponding equation vanishes.

We may then write each averaged macroscopic conservation equation as the sum of local conservation equations for each phase in the RVE. This will introduce the interfacial average terms defined earlier in eqs. (2.10) and (2.11). For instance, if we replace ψ by ρ for each phase $\phi \in \{l, s\}$, eq. (2.12) gives two phase-averaged mass balances, with interfacial terms:

$$\frac{\partial}{\partial t} \left(g^l \langle \rho \rangle^l \right) + \nabla \cdot \left(g^l \langle \rho \rangle^l \mathbf{v}^l \right) = S_V \langle \langle \rho \rangle^l \mathbf{v}^{l*} \cdot \mathbf{n} \rangle^* - S_V \langle \langle \rho \rangle^l \mathbf{v}^* \cdot \mathbf{n} \rangle^* \quad (2.13a)$$

$$\frac{\partial}{\partial t} \left(g^s \langle \rho \rangle^s \right) + \nabla \cdot \left(g^s \langle \rho \rangle^s \mathbf{v}^s \right) = -S_V \langle \langle \rho \rangle^s \mathbf{v}^{s*} \cdot \mathbf{n} \rangle^* + S_V \langle \langle \rho \rangle^s \mathbf{v}^* \cdot \mathbf{n} \rangle^* \quad (2.13b)$$

where $S_V = A_{sl}/V_E$ is the specific surface area, \mathbf{v}^{l*} and \mathbf{v}^{s*} are respectively, the liquid and solid phase velocity at the interface and \mathbf{v}^* is the previously introduced solid-liquid interface velocity. The $\langle \rangle^*$ notation in the RHS of eq. (2.13a) is expanded as follows [Dantzig and Rappaz 2009]:

$$S_V \langle \langle \rho \rangle^l \mathbf{v}^{l*} \cdot \mathbf{n} \rangle^* = \frac{A_{sl}}{V_E} \left(\frac{1}{A_{sl}} \int_{A_{sl}} \langle \rho \rangle^l \mathbf{v}^{l*} \cdot \mathbf{n} \, dA \right) \quad (2.14a)$$

$$= \frac{1}{V_E} \int_{A_{sl}} \langle \rho \rangle^l \mathbf{v}^{l*} \cdot \mathbf{n} \, dA \quad (2.14b)$$

Chapter 2. Modelling Review

Summing equations (2.13a) and (2.13b), results in the overall mass balance in the RVE:

$$\frac{\partial}{\partial t} \left(g^l \langle \rho \rangle^l + g^s \langle \rho \rangle^s \right) + \nabla \cdot \left(g^l \langle \rho \rangle^l \mathbf{v}^l + g^s \langle \rho \rangle^s \mathbf{v}^s \right) = S_V \left\langle \langle \rho \rangle^l \left(\mathbf{v}^{l*} - \mathbf{v}^* \right) \cdot \mathbf{n} \right\rangle^* - S_V \left\langle \langle \rho \rangle^s \left(\mathbf{v}^{s*} - \mathbf{v}^* \right) \cdot \mathbf{n} \right\rangle^* \quad (2.15)$$

where the RHS cancels to zero as shown by [Ni and Beckermann \[1991\]](#). Moreover, the authors show that with their averaging technique, interfacial exchanges for energy, chemical species and momentum cancel out as they are equal in absolute value but opposite in sign. Regarding the LHS terms, their sum is defined along other variables as follows:

$$\langle \rho \rangle = g^l \langle \rho \rangle^l + g^s \langle \rho \rangle^s \quad (2.16)$$

$$\langle \rho \mathbf{v} \rangle = g^l \langle \rho \rangle^l \mathbf{v}^l + \cancel{g^s \langle \rho \rangle^s \mathbf{v}^s} \quad (2.17)$$

$$\langle \rho h \rangle = g^l \langle \rho \rangle^l \langle h \rangle^l + g^s \langle \rho \rangle^s \langle h \rangle^s \quad (2.18)$$

$$\langle \rho h \mathbf{v} \rangle = g^l \langle \rho \rangle^l \langle h \rangle^l \mathbf{v}^l + \cancel{g^s \langle \rho \rangle^s \langle h \rangle^s \mathbf{v}^s} \quad (2.19)$$

$$\langle \rho w_i \rangle = g^l \langle \rho \rangle^l w_i^l + g^s \langle \rho \rangle^s w_i^s \quad (2.20)$$

$$\langle \rho w_i \mathbf{v} \rangle = g^l \langle \rho \rangle^l w_i^l \mathbf{v}^l + \cancel{g^s \langle \rho \rangle^s w_i^s \mathbf{v}^s} \quad (2.21)$$

$$\left\langle \langle \rho \rangle^l \mathbf{v}^l \right\rangle = \left\langle \langle \rho \rangle^l \mathbf{v}^l \right\rangle^l = g^l \langle \rho \rangle^l \mathbf{v}^l \quad (2.22)$$

$$\left\langle \langle \rho \rangle^l \mathbf{v}^l \times \mathbf{v} \right\rangle = g^l \langle \rho \rangle^l \mathbf{v}^l \times \mathbf{v}^l + \cancel{g^s \langle \rho \rangle^s \mathbf{v}^l \times \mathbf{v}^s} \quad (2.23)$$

The average diffusive fluxes are represented by $\langle \mathbf{q} \rangle$ for energy and $\langle \mathbf{j}_i \rangle$ for each solute species. They are respectively modelled using Fourier's thermal conduction law and Fick's first mass diffusion law:

$$\langle \mathbf{q} \rangle = -g^l \langle \kappa \rangle^l \nabla T - g^s \langle \kappa \rangle^s \nabla T = -\langle \kappa \rangle \nabla T \quad (2.24)$$

$$\langle \mathbf{j}_i \rangle = -g^l D^l \nabla \left(\langle \rho \rangle^l w_i^l \right) - \cancel{g^s D^s \nabla \left(\langle \rho \rangle^s w_i^s \right)} \quad (2.25)$$

In eq. (2.25), the macroscopic diffusion coefficient in the solid is neglected, by considering that for macroscopic scales, the average composition of the alloy is much more influenced by advective and diffusive transport in the liquid.

In eq. (2.24), we assume that phases are at thermal equilibrium, that is, temperature is uniform in the RVE. Using eqs. (2.16) to (2.25) and following the same procedure done in eq. (2.15), the averaged equations for mass, energy and species conservation hence

respectively write:

$$\frac{\partial \langle \rho \rangle}{\partial t} + \nabla \cdot \langle \rho \mathbf{v} \rangle = 0 \quad (2.26)$$

$$\frac{\partial \langle \rho h \rangle}{\partial t} + \nabla \cdot \langle \rho h \mathbf{v} \rangle - \nabla \cdot (\langle \kappa \rangle \nabla T) = 0 \quad (2.27)$$

$$\frac{\partial \langle \rho w_i \rangle}{\partial t} + \nabla \cdot \langle \rho w_i \mathbf{v} \rangle - \nabla \cdot \left(g^l D^l \nabla \left(\langle \rho \rangle^l w_i^l \right) \right) = 0 \quad (2.28)$$

As stated previously, the momentum balance in the solid phase is not taken into consideration, hence we do not sum the corresponding local conservation equations. This has consequences on the advection terms in energy and species conservation, and later on we will show the consequences on the momentum conservation in the liquid.

First, the advection terms in eqs. (2.27) and (2.28) shall be redefined by considering that the fluid is incompressible ($\nabla \cdot \langle \mathbf{v}^l \rangle = 0$), which yields:

$$\nabla \cdot \langle \rho h \mathbf{v} \rangle = \langle \mathbf{v}^l \rangle \cdot \nabla \left(\langle \rho \rangle^l \langle h \rangle^l \right) \quad (2.29)$$

$$\nabla \cdot \langle \rho w_i \mathbf{v} \rangle = \langle \mathbf{v}^l \rangle \cdot \nabla \left(\langle \rho \rangle^l w_i^l \right) \quad (2.30)$$

As for the liquid momentum balance, we write:

$$\frac{\partial}{\partial t} \left(\langle \rho \rangle^l g^l \mathbf{v}^l \right) + \nabla \cdot \left(\langle \rho \rangle^l g^l \mathbf{v}^l \times \mathbf{v}^l \right) = \nabla \cdot \left(g^l \bar{\boldsymbol{\sigma}}^l \right) + g^l \mathbf{F}_v^l + \boldsymbol{\Gamma}^l \quad (2.31)$$

where \mathbf{F}_v^l is the vector of external body forces exerted on the liquid phase. In our case, it accounts for the fluid's weight:

$$\mathbf{F}_v^l = \langle \rho \rangle^l \mathbf{g} \quad (2.32)$$

The interfacial momentum transfer between the solid and liquid phases in eq. (2.31) is modelled by a momentum flux vector $\boldsymbol{\Gamma}^l$, consisting of hydrostatic and deviatoric parts, such that:

$$\boldsymbol{\Gamma}^l = \boldsymbol{\Gamma}_p^l + \boldsymbol{\Gamma}_{\mathbb{S}}^l \quad (2.33)$$

$$\boldsymbol{\Gamma}_p^l = p^{l*} \nabla g^l = p^l \nabla g^l \quad (2.34)$$

$$\boldsymbol{\Gamma}_{\mathbb{S}}^l = -g^{l2} \mu^l \mathbb{K}^{-1} (\mathbf{v}^l - \boldsymbol{\varphi}^s) \quad (2.35)$$

where p^{l*} is the pressure at the interface, considered to be equal to the liquid hydrostatic pressure p^l , \mathbb{K} is a permeability scalar (isotropic) computed using eq. (1.2) and μ^l is the liquid's dynamic viscosity. The general form of the Cauchy liquid stress tensor

in eq. (2.31) is decomposed as follows:

$$\left\langle \overline{\overline{\sigma}}^l \right\rangle = g^l \overline{\overline{\sigma}}^l = - \left(\left\langle p^l \right\rangle - \lambda \nabla \cdot \left\langle \mathbf{v}^l \right\rangle \right) \bar{\mathbf{I}} + \left\langle \overline{\overline{\mathbb{S}}}^l \right\rangle \quad (2.36)$$

where λ is a dilatational viscosity [Dantzig and Rappaz 2009] and $\overline{\overline{\mathbb{S}}}^l$ is the liquid strain deviator tensor.

In the literature, the coefficient λ is taken proportional to the viscosity: $\lambda = \frac{2}{3}\mu^l$. However, as we consider an incompressible flow, the divergence term vanishes, thus rewriting eq. (2.36) as follows:

$$\left\langle \overline{\overline{\sigma}}^l \right\rangle = - \left\langle p^l \right\rangle \bar{\mathbf{I}} + \left\langle \overline{\overline{\mathbb{S}}}^l \right\rangle \quad (2.37a)$$

$$\left\langle \overline{\overline{\sigma}}^l \right\rangle = - \left\langle p^l \right\rangle \bar{\mathbf{I}} + 2\mu^l \left\langle \overline{\dot{\epsilon}}^l \right\rangle \quad (2.37b)$$

where the transition from eq. (2.37a) to eq. (2.37b) is made possible by assuming a Newtonian behaviour for the liquid phase. The strain rate tensor, $\left\langle \overline{\dot{\epsilon}}^l \right\rangle$, depends on the average liquid velocity:

$$\left\langle \overline{\overline{\dot{\epsilon}}}^l \right\rangle = \frac{1}{2} \left(\overline{\nabla} \left\langle \mathbf{v}^l \right\rangle + \overline{\nabla^t} \left\langle \mathbf{v}^l \right\rangle \right) \quad (2.38)$$

Finally, we obtain the final form of momentum conservation in the liquid phase coupled with the averaged mass balance, by injecting eqs. (2.32), (2.34), (2.35), (2.37b) and (2.38) in eq. (2.31):

$$\begin{aligned} \frac{\partial}{\partial t} \left(\langle \rho \rangle^l \left\langle \mathbf{v}^l \right\rangle \right) + \frac{1}{g^l} \nabla \cdot \left(\langle \rho \rangle^l \left\langle \mathbf{v}^l \right\rangle \times \left\langle \mathbf{v}^l \right\rangle \right) = \\ - g^l \nabla p^l - 2\mu^l \nabla \cdot \left(\overline{\nabla} \left\langle \mathbf{v}^l \right\rangle + \overline{\nabla^t} \left\langle \mathbf{v}^l \right\rangle \right) - g^l \mu^l \mathbb{K}^{-1} \left\langle \mathbf{v}^l \right\rangle + g^l \langle \rho \rangle^l \mathbf{g} \end{aligned} \quad (2.39)$$

where we intentionally employed the *superficial velocity*, $\langle \mathbf{v}^l \rangle = g^l \mathbf{v}^l$, as the main unknown, together with the liquid pressure p^l . This system, when modelled in 3D, has a total of 4 unknowns (velocity vector and pressure) and 3 equations (X, Y and Z projections for the velocity vector). A fourth equation provided by the mass balance (eq. (2.26)) is therefore added for closure, giving the following system of equations :

$$\left\{ \begin{array}{l} \frac{\partial}{\partial t} (\langle \rho \rangle^l \langle \mathbf{v}^l \rangle) + \frac{1}{g^l} \nabla \cdot (\langle \rho \rangle^l \langle \mathbf{v}^l \rangle \times \langle \mathbf{v}^l \rangle) = \\ - g^l \nabla p^l - 2\mu^l \nabla \cdot (\bar{\nabla} \langle \mathbf{v}^l \rangle + \bar{\nabla}^t \langle \mathbf{v}^l \rangle) - g^l \mu^l \mathbb{K}^{-1} \langle \mathbf{v}^l \rangle + g^l \langle \rho \rangle^l \mathbf{g} \\ \nabla \cdot \langle \mathbf{v}^l \rangle = 0 \end{array} \right. \quad (2.40)$$

Last, the Boussinesq approximation allows taking a constant density in the inertial terms of [eq. \(2.40\)](#) while the variations responsible for buoyancy forces can be deduced from temperature and liquid concentration using thermodynamic databases or directly using known thermal and solutal expansion coefficients, respectively β_T and $\beta_{w_i^l}$, and the reference density value ρ_0^l :

$$\langle \rho \rangle^l = \rho_0^l \left(1 - \beta_T (T - T_0) - \sum_i \beta_{w_i^l} (w_i^l - \langle w_i \rangle_0^l) \right) \quad (2.41)$$

Hence, the final set of equations is better known as the incompressible *Navier-Stokes* equations, applied to a solidifying melt:

$$\left\{ \begin{array}{l} \rho_0^l \left(\frac{\partial \langle \mathbf{v}^l \rangle}{\partial t} + \frac{1}{g^l} \nabla \cdot (\langle \mathbf{v}^l \rangle \times \langle \mathbf{v}^l \rangle) \right) = \\ - g^l \nabla p^l - 2\mu^l \nabla \cdot (\bar{\nabla} \langle \mathbf{v}^l \rangle + \bar{\nabla}^t \langle \mathbf{v}^l \rangle) - g^l \mu^l \mathbb{K}^{-1} \langle \mathbf{v}^l \rangle + g^l \langle \rho \rangle^l \mathbf{g} \\ \nabla \cdot \langle \mathbf{v}^l \rangle = 0 \end{array} \right. \quad (2.42)$$

Since all conservation equations were presented and simplified by the main assumption of a static solid phase, we may include them in a graphical summary in [section 2.1.1](#)

2.2 Eulerian and Lagrangian motion description

2.2.1 Overview

In mechanics, it is possible to describe motion using two well-known motion description: Eulerian and Lagrangian descriptions. To start with the latter, it describes the motion of a particle by attributing a reference frame that moves with the particle. In other words, the particle itself is the center of a reference frame moving at the same

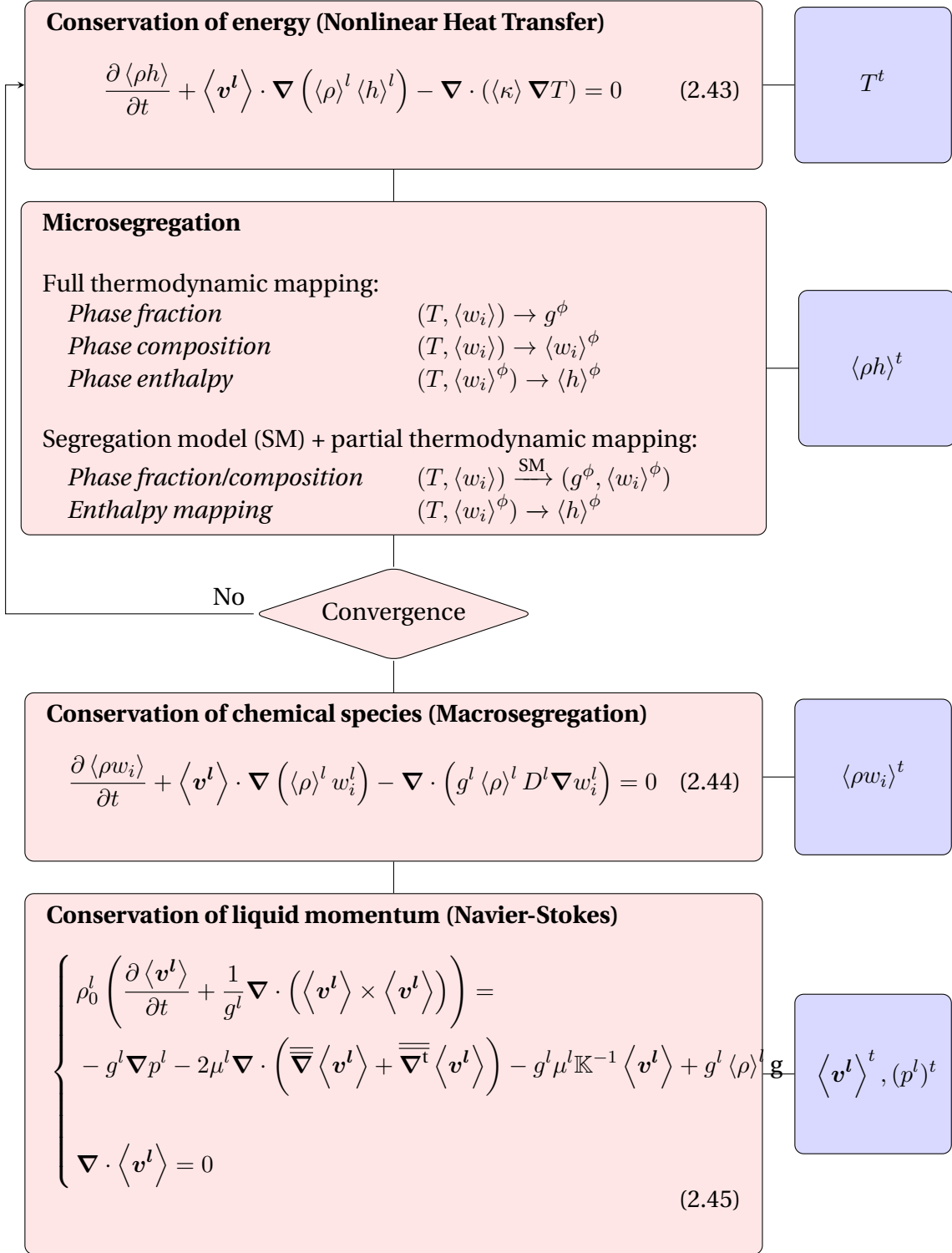


Fig. 2.1 – Graphical resolution algorithm of the conservation equations used in a monodomain macroscopic model to predict macrosegregation for a time increment t . The blue boxes represent the output of each equation.

2.2. Eulerian and Lagrangian motion description

speed during time. The position vector, denoted by \mathbf{x} , is hence updated as follows:

$$\mathbf{x}^{(t+1)} = \mathbf{x}^{(t)} + \mathbf{v}\Delta t \quad (2.46)$$

As such, the total variation of any physical quantity ψ related to the particle can be found by deriving with respect to time, $\frac{d\psi}{dt}$. In contrast to the Lagrangian description, the Eulerian description considers a fixed reference frame and independent of the particle's trajectory. The total variation of ψ cannot be simply described by a temporal derivative, since the particle's velocity is not known to the reference frame, and thus the velocity effect, namely the advective transport of ψ , should also be considered as follows:

$$\frac{d\psi}{dt} = \frac{\partial\psi}{\partial t} + \underbrace{\mathbf{v} \cdot \nabla \psi}_{\text{Advection Transport}} \quad (2.47)$$

In this case, the LHS term is also known as *total* or *material derivative*. The importance of these motion descriptions is essential to solve mechanics, whether for fluids or solids, using a numerical method like the finite element method (FEM). One of the main steps of this method is to spatially discretise a continuum into a grid of points (nodes, vertices ...), where any physical field shall be accordingly discretised. Now, if we focus on a node where velocity has a non zero value and following the previously made analysis, two outcomes are possible: either the node would be fixed (Eulerian) or it would move by a distance proportional to the prescribed velocity (Lagrangian). In the latter case, points located on the boundaries constantly require an update of the imposed boundary conditions.

From these explanations, one can deduce that an Eulerian framework is suited for fluid mechanics problems where velocities are high and may distort the mesh points, whereas the Lagrangian framework is better suited for solid mechanics problems where deformation velocities are relatively low and should well behave when predicting strains.

Another motion description has emerged some decades ago, [Hirt \[1971\]](#) call it the Arbitrary Langrangian-Eulerian (ALE) method. ALE combines advantages from both previous descriptions as it dictates a Lagrangian behaviour at "solid" nodes where solid is deforming, and an Eulerian behaviour at "fluid" nodes.

2.2.2 Interface capturing

As no solid deformation is considered in this work, the Eulerian framework is a convenient choice. Solidification shrinkage is to be considered in our current scope, so it will deform the alloy's outer surface in contact with the air. We intend to track this interface and its motion over time via a numerical method. A wide variety of methods accomplish this task while they yield different advantages and disadvantages.

Such methods fall into two main classes, either interface tracking or interface capturing, among which we cite: marker-and-cell (MAC) [Harlow and Welch 1965], volume of fluid (VOF) [Hirt and Nichols 1981], phase field methods (PF), level set method (LSM) [Osher and Sethian 1988], coupled level set - VOF method and others. The interested reader may refer to quick references by Prosperetti [2002] and Maitre [2006] about these methods.

In the past years, the level set method received a considerable attention in many computational fields, specifically in solidification. For this reason, we will focus on this method henceforth, giving a brief literature review and technical details in the next sections.

2.3 Solidification models with level set

In classic solidification problems, the need to track an interface occurs usually at the solid-liquid interface, that is why the phase field method [Karma and Rappel 1996; Boettinger et al. 2002] and the level set method [Chen et al. 1997; Gibou et al. 2003; Tan and Zabaras 2007] were applied at a microscale to follow mainly the dendritic growth of a single crystal in an undercooled melt. In our case however, when we mention "solidification models using LSM", we do not mean the solid-liquid interface inside the alloy, but it is the alloy(liquid)-air interface that we intend to track, assuming that microscale phenomena between the phases within the alloy, are averaged using the previously defined technique in section 2.1.1.

Very few models were found in the literature, combining solidification and level set as stated previously. Du et al. [2001] applied it to track the interface between two molten alloys in a double casting technique. Welding research, on another hand, has been more active adapting the level set methodology to corresponding applications. In CEMEF, two projects made use of the metal-air level set methodology in welding simulations and showed promising results. Desmaison et al. [2014] employed this methodology to simulate a hybrid arc and laser beam welding used in high thickness steel sheet welding. Later, Chen [2014] applied it to gas metal arc welding (GMAW)

to predict the grain structure in the heat affected zone essentially. More recently, Courtois et al. [2014] used the same methodology but this time to predict keyhole defect formation in spot laser welding. The tracked interface in this case was that between the molten alloy and the corresponding vapor phase.

2.4 The level set method

Firstly introduced by Osher and Sethian [1988], this method became very popular in studying multiphase flows. It is reminded that the term *multiphase* in computational domains usually refers to multiple fluids, and thus should not be mixed with definition of a phase in the current solidification context. For disambiguation, we shall use *multifluid flow* when needed.

The great advantage lies in the way the interface between two fluids, F_1 and F_2 is implicitly captured, unlike other methods where the exact interface position is needed. In a discrete domain, the concept is to assign for each mesh node of position vector \mathbf{x} , the minimum distance $d_\Gamma(\mathbf{x})$ separating it from an interface Γ . The distance function, denoted α and defined in eq. (2.48), is then signed positive or negative, based on the fluid or domain to which the node belongs.

$$\alpha(\mathbf{x}) = \begin{cases} d_\Gamma(\mathbf{x}) & \text{if } \mathbf{x} \in F_1 \\ -d_\Gamma(\mathbf{x}) & \text{if } \mathbf{x} \in F_2 \\ 0 & \text{if } \mathbf{x} \in \Gamma_{F1,F2} \end{cases} \quad (2.48)$$

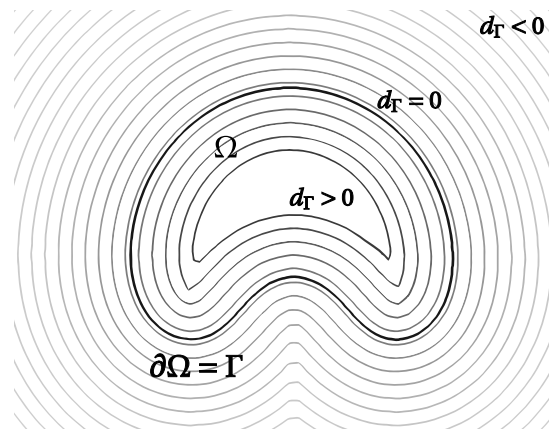


Fig. 2.2 – Schematic of the interface Γ (thick black line) of a rising air bubble (Ω) in water. The other contours represent isovalues of the distance function around and inside the interface contour. Those outside are signed negative whereas inside they are signed positive.

2.4.1 Diffuse interface

The level set has many attractive properties that allows seamless implementation in 2D and 3D models. It is a continuously differentiable C^1 -function. The Heaviside function is also continuous but non differentiable, with an abrupt transition from 0 to 1 across the sharp interface, as follows:

$$H = H(\alpha(\mathbf{x})) = \begin{cases} 0 & \text{if } \alpha(\mathbf{x}) < 0 \\ 1 & \text{if } \alpha(\mathbf{x}) \geq 0 \end{cases} \quad (2.49)$$

With the help of eq. (2.49), we can define the geometric "presence" of a domain with respect to the interface. As such, material properties depend upon this function, which will be discussed later in section 2.4.2. It is established that a steep transition can lead to numerical problems, so the Heaviside function should be smoothed in a volume of fixed thickness around the interface.

Sinusoidal smoothing in eq. (2.50) is widely used with level set formulations.

$$H = \begin{cases} 0 & \text{if } \alpha(\mathbf{x}) < -\varepsilon \\ 1 & \text{if } \alpha(\mathbf{x}) > \varepsilon \\ \frac{1}{2} \left(1 + \frac{\alpha(\mathbf{x})}{\varepsilon} + \frac{1}{\pi} \sin \left(\frac{\pi \alpha(\mathbf{x})}{\varepsilon} \right) \right) & \text{if } -\varepsilon \leq \alpha(\mathbf{x}) \leq \varepsilon \end{cases} \quad (2.50)$$

where the interval $[-\varepsilon; +\varepsilon]$ is an artificial interface thickness around the zero distance.

Defining a diffuse interface rather than a sharp one, is also a common approach in phase field methods [Beckermann et al. 1999; Sun and Beckermann 2004]. It is emphasized that the latter methods give physically meaningful analysis of a diffuse interface and the optimal thickness by thoroughly studying the intricate phenomena happening at the scale of the interface. However, for level set methods, there has not been a formal work leading the same type of analysis. For this reason, many aspects of the level set method lack physical meanings but remain computationally useful. In a recent paper by Gada and Sharma [2009], the authors respond partially to this problem by analysing and deriving conservation equations using a level set in a more meaningful way, but do not discuss the diffuse interface aspect.

The Dirac delta function is also an important property to convert surface integrals to volume terms, which could turn useful when modelling surface tension effects for instance, using the *continuum surface force* method (CSF) [Brackbill et al. 1992]. The Dirac function, plotted in fig. 2.3 along with the Heaviside function within an interface

thickness of $[-\varepsilon; +\varepsilon]$, is derived from the Heaviside as follows:

$$\delta(\alpha) = \delta(\alpha(\mathbf{x})) = \frac{\partial H}{\partial \alpha(\mathbf{x})} = \begin{cases} \frac{1}{2\varepsilon} \left(1 + \cos\left(\frac{\pi\alpha(\mathbf{x})}{\varepsilon}\right)\right) & \text{if } |\alpha(\mathbf{x})| \leq \varepsilon \\ 0 & \text{if } |\alpha(\mathbf{x})| > \varepsilon \end{cases} \quad (2.51)$$

The Heaviside and delta Dirac functions can be readily processed to obtain other geometric properties from the level set, which are extremely useful. In the context of a system Ω , containing two domains metal (M) and gas (G) separated by an interface Γ , the following properties are interesting to study [Peng et al. 1999]:

$$\text{normal vector : } \mathbf{n} = \frac{\nabla \alpha}{\|\nabla \alpha\|} \quad (2.52)$$

$$\text{curvature : } \zeta = -\nabla \cdot \mathbf{n} \quad (2.53)$$

$$\text{surface area of the air-metal interface : } A^\Gamma = \int_{\Omega} \delta(\alpha) \|\nabla \alpha\| d\Omega \quad (2.54)$$

$$\text{metal volume : } V^M = \int_{\Omega} H^M d\Omega \quad (2.55)$$

It is reminded that for a 2D case, eq. (2.54) evaluates a length instead of the area while eq. (2.55) gives the area instead of volume. Finally, within the diffuse interface, fluids properties may vary linearly or not, depending on the mixing law, which is presented in the next section.

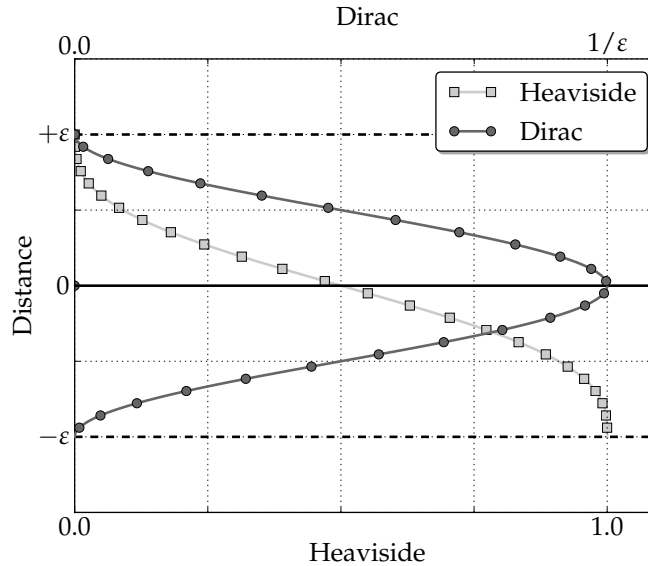


Fig. 2.3 – Schematic of two level properties inside the diffuse interface: Heaviside (lower x-axis) and Dirac delta (upper x-axis) functions. Note that the peak of the Dirac function depends on the interface thickness to ensure a unity integral of the delta function over Ω .

2.4.2 Mixing Laws

A *monolithic* resolution style, as opposed to a *partitioned* resolution, is based on solving a single set of equations for both fluids separated by an interface, as if a single fluid were considered. Level set is one among many methods that use the monolithic style to derive a single set of conservation equations for both fluids. The switch from one material to the other is implicitly taken care of by using the Heaviside function as well as mixing laws. These laws are crucial to define how properties vary across the diffuse interface in view of a more accurate resolution. The most frequently used mixing law in the literature is the arithmetic law. Other transitions are less known such as the harmonic and logarithmic mixing. The first law is maybe the most intuitive and most used for properties mixture as it emanates from VOF-based methods. If we consider any property ψ (for instance the fluid's dynamic viscosity μ) then the arithmetic law will give a mixed property $\hat{\psi}$ as follows:

$$\hat{\psi} = H^{F_1}\psi^{F_1} + H^{F_2}\psi^{F_2} \quad (2.56)$$

Basically, the result is an average property that follows the same trend as the Heaviside function. As for the harmonic law, it writes:

$$\hat{\psi} = \left(\frac{H^{F_1}}{\psi^{F_1}} + \frac{H^{F_2}}{\psi^{F_2}} \right)^{-1} \quad (2.57)$$

and last, the logarithmic law writes:

$$\hat{\psi} = n^{(H^{F_1} \log_n \psi^{F_1} + H^{F_2} \log_n \psi^{F_2})} \quad (2.58)$$

where n is any real number serving as a logarithm base, which often is either the exponential e or 10. The mixture result with this law is the same, regardless of the value of n . By looking to [fig. 2.4](#), we clearly see that the difference between all three approaches is the property weight given to each side of the level set in the mixture. The arithmetic law, being symmetric, has equal weights, ψ^{F_1} and ψ^{F_2} , in the final mixture. Nevertheless, the asymmetric harmonic mixing varies inside the diffuse interface with a dominant weight of one property over the other. As for the logarithmic mixture, it can be seen as an intermediate transition between the preceding laws. As long as the interface thickness is small enough, the choice of a mixing law should not drastically change the result, inasmuch as it depends on the discretisation resolution of the interface. This fact made the arithmetic mixing the most applied one, because it is symmetric and easy to implement (no handling of potential division problems like

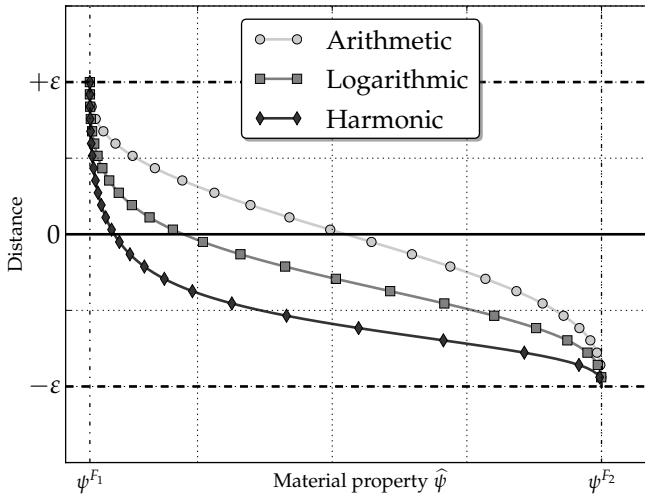


Fig. 2.4 – Three mixing laws, arithmetic, logarithmic and harmonic commonly used in monolithic formulations.

harmonic laws for instance). However, Strotos et al. [2008] claim that the harmonic law proves to conserve better diffusive fluxes at the interface. More recently, an interesting study made by Ettrich et al. [2014] focused on mixing thermal properties using a phase field method. They define a diffuse interface in which they separately mix the thermal conductivity, κ , and the heat capacity, C_p , then compute the thermal diffusivity as the ratio of these properties. Later, the authors compare the temperature field obtained by diffusion to a reference case in order to decide which combination of mixing laws gives the best result. Despite not being directly related to a level set method, this work gives an insight of the mixture possibilities and their effect on a pure thermal diffusion. Otherwise, little work has been found in the literature on the broad effects of mixture types on simulation results in a level set context.

2.5 Interface motion

When a physical interface needs to have topology changes because of fluid structure interaction or surface tension for instance, the level set model can follow these changes by a transport step. The idea is to advect the signed distance function, its zero isovalue representing the interface and all other distant isovales, with the velocity field as input. The motion of the interface is thus expressed by:

$$\frac{d\alpha}{dt} = \frac{\partial\alpha}{\partial t} + \mathbf{v} \cdot \nabla\alpha = 0 \quad (2.59)$$

2.5.1 Level set transport

The finite element method gives the fully discretised weak form of [eq. \(2.59\)](#) by using a convenient set of test functions α^* belonging the Hilbertian *Sobolev* space:

$$\int_{\Omega} \alpha^* \frac{\partial \alpha}{\partial t} d\Omega + \int_{\Omega} \alpha^* \mathbf{v} \cdot \nabla \alpha d\Omega = 0 \quad \forall \alpha^* \in \mathcal{H}^1(\Omega) \quad (2.60)$$

The spatial discretisation of α assigns, for each of the total N nodes of a simplex, the following values:

$$\alpha = \sum_N P_j \alpha_j \quad (2.61)$$

Furthermore, with the standard Galerkin method, we replace test functions by the interpolation functions P_j , then we apply a temporal discretisation for the main unknowns by a forward (implicit) finite difference in time. Consequently, [eq. \(2.60\)](#) can be recast as follows:

$$i, j : 1 \rightarrow \text{Nnodes}$$

$$\frac{1}{\Delta t} (\alpha_j^t - \alpha_j^{t-\Delta t}) \int_{\Omega} P_i P_j d\Omega + \alpha_j^t \int_{\Omega} \mathbf{v}^t \cdot \nabla P_j d\Omega = 0 \quad (2.62a)$$

$$\left[\frac{1}{\Delta t} \int_{\Omega} P_i P_j d\Omega + \int_{\Omega} \mathbf{v}^t \cdot \nabla P_j d\Omega \right] \alpha_j^t = \frac{1}{\Delta t} \int_{\Omega} \alpha^{t-\Delta t} P_i d\Omega \quad (2.62b)$$

$$[\mathcal{M}_{ij} + \mathcal{A}_{ij}] \alpha_j^t = \mathcal{F}_i \quad (2.62c)$$

where \mathcal{M}_{ij} and \mathcal{A}_{ij} are respectively the mass (or capacity) matrix and advection matrix, both written within a local finite element, whereas \mathcal{F}_i is a local vector of known quantities from the previous time step. The solution of the linear system in [eq. \(2.62c\)](#) is the transported distance function.

When the convection regime becomes more dominant diffusion (for high Reynolds number), the standard Galerkin method may lead to instabilities in the solution. In this case, stabilisation is crucial to avoid these oscillations, unless very fine remeshing is done "such that convection no longer dominates on an element level", as stated by [Brooks and Hughes \[1982\]](#). The authors give a brief explanation of how numerically a convection-dominated equation can lead to oscillatory solutions with the standard Galerkin approximation. They proposed a stabilisation scheme, the Streamline Upwind Petrov-Galerkin, better known as SUPG, to stabilise advection dominated Navier-Stokes equations. However, their technique applies to any convection-diffusion equation. The SUPG method consists of modifying the test functions (like a classical Petrov-

Galerkin method) by adding artificial diffusion in the flow direction. The modified test function writes:

$$\alpha_{SUPG}^* = \alpha^* + \underbrace{C_{SUPG}^E (\mathbf{v}_{\text{transport}} \cdot \nabla \alpha^*)}_{\text{Upwind contribution}} \quad (2.63)$$

where the upwind contribution for each finite element E depends on a stabilisation parameter C_{SUPG}^E that is expressed as follows:

$$C_{SUPG}^E = \frac{h^E}{v_{\text{flow}}^E} \quad (2.64)$$

[Equation \(2.64\)](#) shows that the SUPG parameter represents a time constant relative to an element mesh size, h^E , and an average velocity that should represent the magnitude in the flow direction. In the present work, all convection-diffusion equations are stabilised with the SUPG method, namely the conservation of mass, energy, momentum and chemical species as well as the level set transport.

2.5.2 Level set regularisation

Upon transport the distance function field, a crucial property of the level set may be partially or totally lost over the domain, which is:

$$\begin{cases} \|\nabla \alpha\| = 1 \\ \alpha(x, t) = 0 & \text{if } x \in \Gamma(t) \end{cases} \quad (2.65)$$

The closer this L^2 -norm to one, the more regular the level set. An irregular distance function induces cumulative numerical errors while transporting distance values far from the interface, resulting in wrong distance information, and loss of properties that make up a "distance function". To show one the benefit of level set regularisation, [Basset \[2006\]](#) states after showing several tests of distance function transport, that regularised distance functions transported with a standard Galerkin method (i.e. without any stabilisation) show better "quality" globally in the domain, compared to initially non-regularised ones. When the transport equation in [eq. \(2.59\)](#) is discretised in time then solved, a *regularisation* (also known as *reinitialisation*) is necessary to conserve as much as possible the property in [eq. \(2.65\)](#).

[Figure 2.5](#) shows the need of regularisation in two different simulations of the same phenomenon: rising air bubble inside water. The importance of this well studied case [[Sussman et al. 1994](#); [Hysing et al. 2009](#)] is that the interface between two fluids is

highly deformable as the bubble rises because of buoyancy, and therefore the task of tracking the dynamic interface while maintaining an accurate distance function is a considerable numerical task. In the first simulation, the distance contours are squeezed against the zero-distance contour marked by the thick black line. A closer look to the interface reveals undesired distortions, with a "wavy" shape at some points. This effect is evidently an artefact of a level set transport lacking subsequent reinitialisation, inasmuch as the surface tension tends to minimise the total surface area and make it as smooth as possible. Nevertheless, the second simulation unveils much better results, especially how the interface shows no sign of destabilisation. We also note the regular spacing between contours, which is a consequence of conserving the property defined in [eq. \(2.65\)](#). This improvement is attributed to the regularization done at each time step after the transport. In the forthcoming sections, we present three regularisation methods, then show their strong and weak points.

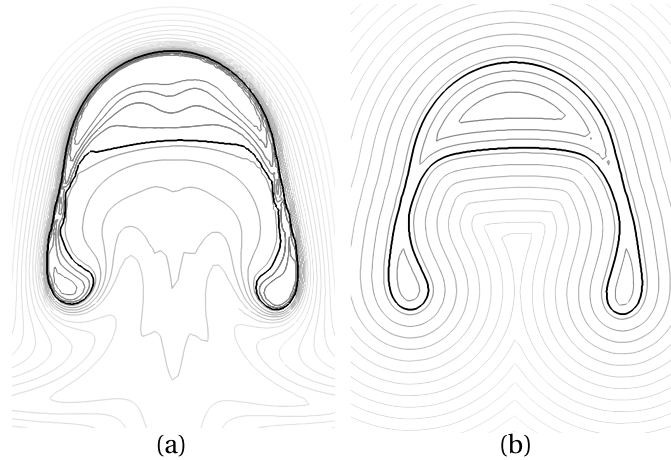


Fig. 2.5 – Schematic of the influence of level set regularisation on the distance function at the same time frame: a) without any regularisation step, the isovalue contours are distorted in the wake of the rising air bubble while being squeezed ahead of it, b) in contrast to regularising the distance function, where the contours maintain their spacing and geometric properties with respect to the tracked interface.

Classic Hamilton-Jacobi reinitialisation

In order to repair a distance function impaired by convective transport, [Sussman et al. \[1994\]](#) proposed solving a classic *Hamilton-Jacobi* equation, given in its most general form:

$$\frac{\partial \alpha}{\partial t} + \mathbb{H}(\alpha, x, t) = 0 \quad x \in \Omega, t > 0 \quad (2.66)$$

where $\alpha(x, t = 0) = \alpha_0$ is the initial value of the distance function. The term \mathbb{H} is known as the *Hamiltonian*. When the sign of the level set and its metric property ($\|\nabla\alpha\| = 1$) are considered, eq. (2.66) reduces to:

$$\frac{\partial\alpha}{\partial t} + S(\alpha)(\|\nabla\alpha\| - 1) = 0 \quad (2.67)$$

where $S(\alpha)$ is a step function giving the sign of the level set as follows:

$$S(\alpha) = \frac{\alpha}{|\alpha|} = \begin{cases} -1 & \text{if } \alpha < 0 \\ 0 & \text{if } \alpha = 0 \\ +1 & \text{if } \alpha > 0 \end{cases} \quad (2.68)$$

The sign function defined in eq. (2.68) is often smoothed to avoid numerical problems, as proposed for instance by [Sussman et al. \[1994\]](#):

$$S(\alpha) = S_\varepsilon(\alpha) = \frac{\alpha}{\sqrt{\alpha^2 + \varepsilon^2}} \quad (2.69)$$

where ε is a smoothing parameter that depends on the mesh size around the interface. However, one should be aware that within the smoothing thickness, the regularised function may suffer from local oscillations because of the reciprocal reinitialisation taking place at each side of the level set. [Peng et al. \[1999\]](#) states that this problem is more likely to happen if the initial level set shows very weak or very steep gradients, and therefore is not regular enough. The authors eventually propose a new sign function which would reinitialise the distance function, as close as possible to the interface without modifying the latter, as follows:

$$S(\alpha) = S_\varepsilon(\alpha) = \frac{\alpha}{\sqrt{\alpha^2 + \|\nabla\alpha\|^2\varepsilon^2}} \quad (2.70)$$

Convective reinitialization

A recent work by [Ville et al. \[2011\]](#) introduced another concept for reinitialisation called the *convective reinitialisation*. The idea lies in combining both level set advection and regularisation in a single equation, saving resolution time. The key components of their method starts by defining a pseudo time step, $\Delta\tau$, that is linked to the main time variable through a numerical parameter λ_τ , as follows:

$$\lambda_\tau = \frac{\partial\tau}{\partial t} \quad (2.71)$$

The order of magnitude of λ_τ , which can be seen as a relaxation parameter [see [Vigneaux 2007](#), p. 89], is close to the ratio $h/\Delta t$. Then, the classic Hamilton-Jacobi [eq. \(2.66\)](#) is combined into the convection step by writing:

$$\frac{\partial \alpha}{\partial t} + (\mathbf{v} + \lambda_\tau \mathbf{U}) \cdot \nabla \alpha = \lambda_\tau S(\alpha) \quad (2.72)$$

where \mathbf{U} is a velocity vector in the normal direction to the interface, defined by $\mathbf{U} = S(\alpha)\mathbf{n}$, the normal vector \mathbf{n} being previously defined in [eq. \(2.52\)](#). The obvious shortcoming of convective reinitialisation is that it depends on a numerical parameter λ_τ . Another limitation of the method is the use of a sinusoidal filter to modify the distance function by truncating its values beyond a thickness threshold, which is also another parameter to calibrate the resolution. The drawback of truncating the level set is the loss of information far from the interface and the inability to fully reconstruct the distance function. If we denote this threshold by E and the modified level set by $\tilde{\alpha}$ inside the thickness, then [eq. \(2.72\)](#) is recast as:

$$\frac{\partial \alpha}{\partial t} + (\mathbf{v} + \lambda_\tau \mathbf{U}) \cdot \nabla \alpha = \lambda_\tau S(\alpha) \sqrt{1 - \left(\frac{\pi}{2E}\tilde{\alpha}\right)^2} \quad (2.73)$$

[Equation \(2.73\)](#) describes the transport and partial reconstruction of the distance function α , knowing its value $\tilde{\alpha}$ inside the thickness E .

Geometric reinitialization

This category of methods go from the level set's basic geometric principle to construct a distance function, instead of solving a partial differential system of equations as in the classic Hamilton-Jacobi reinitialisation. A widely known instance of this category is the *fast marching method* developed by [Sethian \[1996\]](#) and influenced by the [Dijkstra \[1959\]](#)'s method to compute the shortest path in a network of nodes. The method aims to solve the eikonal equation in [eq. \(2.65\)](#) to propagate the distance function in a single direction by *upwinding*, i.e. going from low to high values of the distance function, while preserving a unitary distance gradient.

Direct reinitialisation is another interesting method in the geometric reinitialise category. However, it has not gained noticeable attention in the literature given the terrible cost in terms of computation time and efficiency if not optimised. The main idea is very simple: reconstruct the distance function over Ω or a subset of Ω , by computing the minimum distance between each mesh node and the interface. It means that, for

any point $x \in \Omega$, the following constraint should be satisfied [Osher and Fedkiw \[2003\]](#):

$$d_\Gamma(x) = \min \|x - x_\Gamma\| \quad \forall x_\Gamma \in \partial\Omega = \Gamma, \quad (2.74)$$

A efficient and optimised implementation of this method is done by [Shakoor et al. \[2015\]](#) making use of k - d trees to limit the search operations of elements and the subsequent distance evaluations in each of these elements. Moreover, the authors give a comparison of the previously stated methods on 2D and 3D cases, showing the great performance of direction reinitialisation when used with k-d trees algorithm, hence we use it in the present work.

2.6 Mesh adaptation

2.6.1 Metrics and anisotropy

The key to reduce spatial discretisation errors and obtain better results is a fine mesh. The optimal mesh resolution depends on the equations being discretised and solved on the FE grid, which consists of an array of structured triangles ([fig. 2.6a](#)), in the most basic situation. However, the potential of the Finite Element Method over other methods like the Finite Volume Method (FVM) is the use of unstructured grids. The easiest meshing solution one can choose is to create unstructured homogeneous and isotropic grid ([fig. 2.6b](#)), while respecting some constraints regarding the time step (temporal discretisation) stemming from physical or numerical conditions, e.g. diffusion shock constraint in diffusional transient equations or Courant–Friedrichs–Lewy (CFL) condition in transient advective equations. In such a case, errors due to interpolation are minimised, which guarantees good results but with expensive time cost.

Heterogeneous meshes ([fig. 2.6c](#)) that consist of fine isotropic elements in areas of interest along with coarser isotropic elements in other areas, may reduce the needed time to solve each conservation equation. Although this is an interesting alternative, it is less powerful than anisotropic meshing. In the latter ([fig. 2.6d](#)), elements adapt to a physical quantity, such as enthalpy or velocity, reducing the elemental length in the direction where the gradient is higher, while stretching the element in the orthogonal direction. This allows more accurate resolution with less elements than needed by isotropic meshing. Moreover, this type of meshing is well adapted to the context of this thesis as it allows getting a fine mesh in the normal direction to the interface, that is in its transport direction, while reducing the number of elements in other directions. Regions undergoing solidification are also important to remesh since microsegregation starts in the mushy zone, i.e. between the liquidus and solidus temperatures

given by a local average composition, where fluid flow may transport species, leading eventually to macrosegregation.

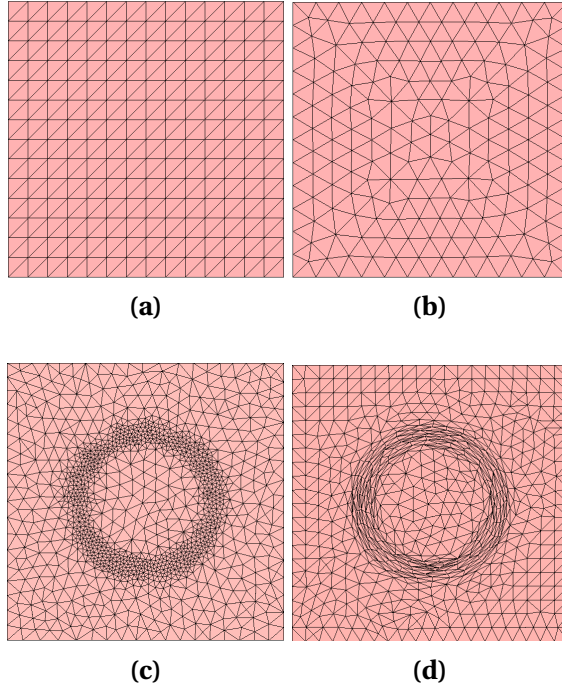


Fig. 2.6 – Alternatives for initial finite element grid generation: (a) structured homogeneous, (b) unstructured homogeneous isotropic, (c) unstructured heterogeneous isotropic and (d) unstructured heterogeneous anisotropic meshes.

Since mesh adaptation involves advanced mathematical notions, readers interested in the basics are referred to the following references: [Coupez 1991; Coupez 2000; Gruau and Coupez 2005; Jannoun 2014]. In this study, we show and compare different remeshing methods relevant to macrosegregation prediction, and based on previous work done at CEMEF. These techniques rely on metric tensors, and some of them belong to *a posteriori* error estimators category. A metric or a metric tensor \mathcal{M} , also known as *Riemannian* metric, is a positive symmetric definite matrix that relates to an element's size in \mathbb{R}^3 via:

$$\mathcal{M} = \begin{pmatrix} M_{11} & M_{12} & M_{13} \\ M_{12} & M_{22} & M_{23} \\ M_{13} & M_{23} & M_{33} \end{pmatrix} = \mathcal{R} \begin{pmatrix} 1/h_x^2 & 0 & 0 \\ 0 & 1/h_y^2 & 0 \\ 0 & 0 & 1/h_z^2 \end{pmatrix} \mathcal{R}^T \quad (2.75)$$

where \mathcal{R} is a rotation matrix and h_x , h_y and h_z are the respective dilatation scalars defined by the metric in the (x, y, z) space, describing a three-dimensional anisotropy. The metric information is then passed to a mesh generation tool, called *MTC*, which is based on an iterative procedure of local topology optimisations. We focus hereafter

on two adaptive remeshing techniques, then discuss the functional details and show some examples.

2.6.2 Remesh2: Interface remeshing

Remesh2 is an explicit method to compute an anisotropic metric around the zero surface of a distance function. The idea is, as mentioned previously, to reduce the elements cost in the tangential directions to level set by stretching the elements, leaving small element lengths in the normal direction, where the level set gradient is the greatest. This method is not based on error estimators, but rather on explicit input from the user who chooses the mesh size in normal and tangential directions to the interface, as well as in the positive and negative regions delimited by the level set. The following parameters are used as input data to determine the final node-wise metric:

- h_n mesh size in the normal direction of the level set
- h_τ mesh size in the tangential directions of the level set
- h_M mesh size in the metal
- h_A mesh size in the air
- α distance function (level set)
- ε level set mixing thickness
- V arbitrary vector

Algorithm 1: *Remesh2* metric construction

Data: $n \quad h_M \quad h_A \quad h_n \quad h_\tau \quad \alpha$
Result: \mathcal{M}_2

 Initialise node index: $j = 0$;

while $j \leq j_{end}$ **do**
if $\alpha_j < \varepsilon$ **then**

 Compute normal direction to level set: $n = \nabla\alpha / \|\nabla\alpha\|$;

 Compute the first tangential direction: $\tau_1 = V - (V \cdot n) \cdot n$;

 Deduce the second tangential direction: $\tau_2 = n \wedge \tau_1$;

 Compute rotation matrix and its transpose: \mathcal{R}_j and \mathcal{R}_j^{-1} ;

 Deduce P1 metric at node j : $(\mathcal{M}_2)_j = \mathcal{R}_j \Lambda \mathcal{R}_j^{-1}$
else

go back to the beginning of current section;

 Increment j ;

2.6.3 *Remesh4*: Multi-criteria remeshing

It is a metric construction method based on edge-based error distribution

What i concluded from Z-FAST-SMACS cases A and B, where remesh4 was used in two different ways (LS and velocity/100 , LS and ConcentrationPosNeg) is that for diffuse interface thickness less than 2e-4 m, mass conservation gets all sorts of problems, because of low element resolution around interface while higher resolution at the tips of the transition region

To do ?

Interface Remeshing: Importance when using a static level set and more importantly when LS is transported, influence of mixing area *thickness* and *resolution* (i.e. nb of nodes with the area), Isotropic or anisotropic ? the first is more important to composition calculation while the second is more relevant if we mean do thermohydraulics without macrosegregation

Résumé chapitre 2

Chapter 5

Macrosegregation with solidification shrinkage

Contents

5.1	Solidification shrinkage	117
5.2	Choice of boundary tracking	117
5.3	Multidomain formalism	119
5.3.1	Assumptions	121
5.4	FE partitioned model	122
5.4.1	In the metal	122
5.4.2	In the air	126
5.5	FE monolithic model	128
5.5.1	Monolithic equations	128
5.6	1D application: solidification with inverse segregation	133
5.6.1	Geometry and boundary conditions	133
5.6.2	Shrinkage without macrosegregation	133
5.6.3	Shrinkage with macrosegregation	143
5.7	2D application: controlled solidification benchmark	153
5.7.1	Boundary condition effect	153
5.7.2	Computational configuration	155
5.7.3	Results	156
5.8	3D application: reduced-gravity solidification	161
5.8.1	Previous work	161
5.8.2	Computational configuration	164
5.8.3	Texus binary alloy	171

Chapter 5. Macrosegregation with solidification shrinkage

5.8.4 Texus ternary and quaternary alloys 179

5.1 Solidification shrinkage

Solidification shrinkage is, by definition, the effect of relative density change between the liquid and solid phases. In general, it results in a progressive volume change during solidification, until the phase change has finished. The four stages in [figs. 5.1a](#) to [5.1d](#) depict the volume change with respect to solidification time. First, at the level of the first solid crust, near the local solidus temperature, the solid forms with a density greater than the liquid. The subsequent volume decrease forces the fluid to be sucked in the direction of the volume change (cf. [fig. 5.1b](#)). As a direct result of the inward feeding flow, the ingot free surface with the air tends to gradually deform to follow the feeding direction, forming the so-called *shrinkage pipe*, shown in [fig. 5.2](#). Since the mass of the alloy and its chemical species is conserved, a density difference between the phases ($\langle \rho \rangle^l < \langle \rho \rangle^s \implies \frac{\langle \rho \rangle^l}{\langle \rho \rangle^s} < 1$) eventually leads to a different overall volume ($V^s < V^l$) once solidification is complete, as confirm the following mass conservation equations, from initial (LHS term) to final (RHS term) state:

$$\langle \rho \rangle^l V^l = \langle \rho \rangle^s V^s \quad (5.1a)$$

$$V^s = \frac{\langle \rho \rangle^l}{\langle \rho \rangle^s} V^l \quad (5.1b)$$

Solidification shrinkage is not the only factor responsible for volume decrease. Shrinkage due to temperature and composition variations in both solid and liquid phases, are also common causes in a casting process. Thermal shrinkage is very important to apprehend in steel casting, as the temperature decrease usually exceeds a 1000 °C, thus causing substantial density variations.

5.2 Choice of boundary tracking

In chapter 2, several methods of boundary tracking/capturing methods were presented along with their similarities and differences. In the case of solidification shrinkage, the metal-air boundary can be tracked with any method from the previously mentioned. However, several reasons motivate us to settle on the level set method. First, the easiest solution is testing a method which already exists in *CimLib* library. The level set method was implemented as a framework for monolithic resolution. Since this work, the method has been extensively used and improved in several projects mainly for multiphase flows, which is the main competence of the Computing and FLuids (C.FL.) group at CEMEF. Another motivation is the compatibility between *CimLib* and *THERCAST*®, where the latter is the final destination of the code developed

Chapter 5. Macrosegregation with solidification shrinkage

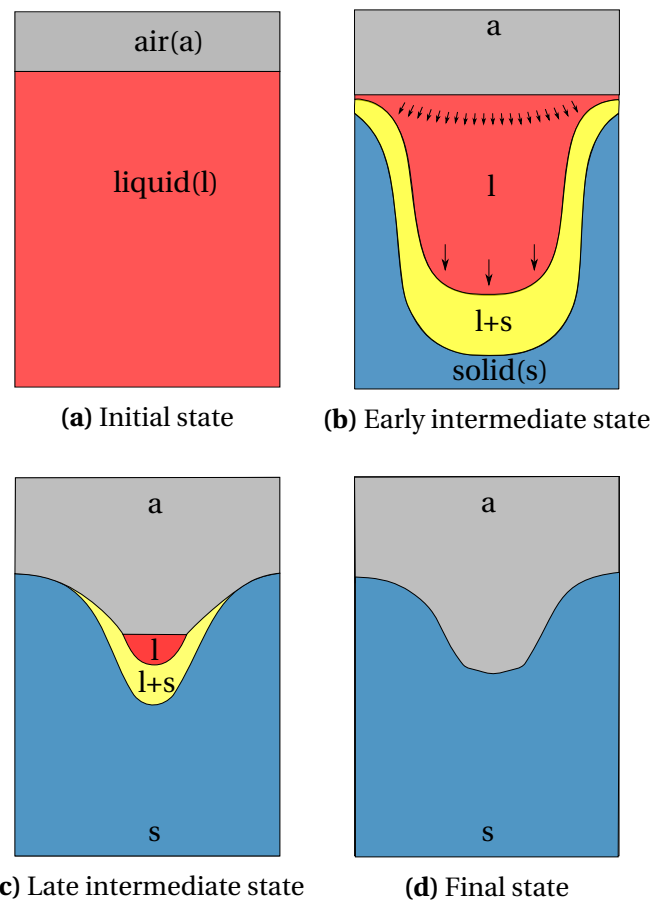


Fig. 5.1 – Schematic of the main cooling stages of an ingot against side and bottom mould walls (not shown)

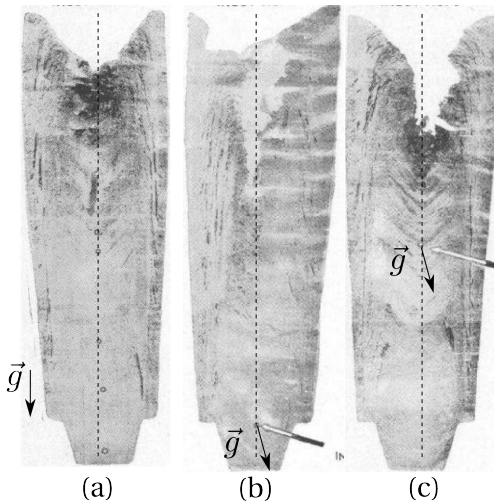


Fig. 5.2 – Sulphur prints of three ingots showing pipe formation at the top as a result of solidification shrinkage, marked with dark areas corresponding to higher sulphur content, while varying ingot inclination during casting. Ingot orientation changes from (a) vertical position to (b) 25° -inclination after 34 minutes of vertical (dashed line) casting and finally (c) 25° -inclination after 3 hours of vertical casting. The white arrow indicates the inclination onset [Onodera and Arakida 1959]. The black arrow indicates the gravity direction.

during this Ph.D. thesis. In its recent versions, *THERCAST®* handles laminar and turbulent ingot filling where the level set method is used to capture the free surface of the molten metal. Aside from the practical motivations, some technical aspects of the level set method make it very attractive to apply it to macroscopic surface tracking (in contrast to microscopic interface tracking, for instance the solid-liquid interface), such as topological properties that are readily available (e.g. curvature) and accurate position compared to volume-based methods like VOF.

5.3 Multidomain formalism

In the previous chapters, we considered in our simulations the metallic alloy as a saturated mixture of solid and liquid during solidification. It means that no gas phase may appear during the process. The reason is that we chose to describe our model in Eulerian description, for which we have considered a fixed grid to discretise the averaged conservation equations governing the phase change between the liquid and solid phases. Furthermore, with the introduction of shrinkage, an increase in global density of the metallic alloy means that a gas phase should enter the domain to replace the shrunk volume.

At this point, several interfaces may be distinguished: liquid-solid ($l-s$), liquid-air ($l-a$) and solid-air ($s-a$), where we defined 2 phases (l and s) belonging to the "Metal"

Chapter 5. Macrosegregation with solidification shrinkage

domain denoted M , while the "Air" domain, denoted A , is made up of a unique gas phase, (a), with the same name. As a standard for this formalism, we consider that upper case letters are used for domains, while lower case letters are used for phases. The main idea behind the multidomain formalism is to go from the classic conservations equations introduced by volume averaging in chapter 2 in the context of a solidifying two-phase system to generalise it by taking into account a third gas phase, such as:

$$V^l + V^s + V^a = V_E \quad (5.2)$$

$$g^l + g^s + g^a = 1 \quad (5.3)$$

where g^ϕ is the volume fraction of each phase $\phi = [l, s, a]$. Then, one is free to choose a suitable numerical method to define and track the physical interfaces between the several phases. In our applications, we are particularly interested in keeping an indirect representation of the l - s interface (dotted line in fig. 5.3) using the volume averaging theory, while employing a different method to track the l - a and s - a interfaces (dashed lines in fig. 5.3) with the level set method. This allows switching to the latter method in a physically representative manner.

In this context, each domain can be seen as a material having a physical interface with the other domains. As a consequence of our interpretation, the gas phase should not exist in the metal, which may naturally occur if the thermodynamic conditions are in favour of nucleating and growing a new phase, or in the case of a gas that was trapped inside mould grooves.

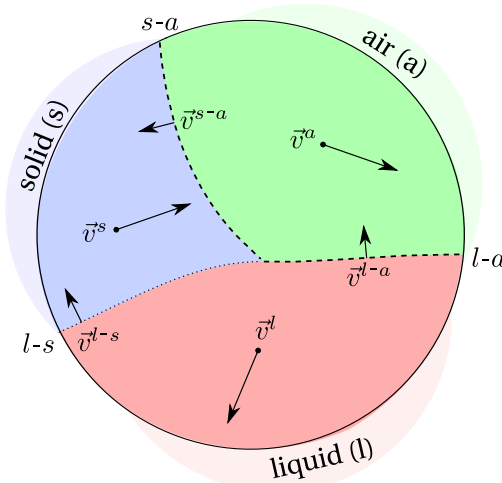


Fig. 5.3 – Schematic of a representative volume element containing 3 phases with distinct velocities, separated by 3 interfaces. The dotted line is the indirectly tracked solid-liquid interface while the other dashed lines, air-liquid and air-solid interfaces, are directly tracked.

5.3.1 Assumptions

Each phase in the system has its own velocity, v^l , v^s and v^a , while the respective interfaces $l-s$, $l-a$ and $s-a$ have different and independent velocities, represented by v^{l-s} , v^{l-a} and v^{s-a} . Note that the solid-liquid interface velocity was denoted v^* in the previous chapters as no more than two phases were considered. The first major assumption is that the solid phase, once formed from the liquid, is fixed and rigid, hence $v^s = 0$. It means that no subsequent deformation or contraction/dilatation of the solid phase ($\langle \rho \rangle^s = \text{constant}$) may occur and therefore v^{s-a} reduces to vector zero. Moreover, we use the already introduced volume averaging principles to write locally for any quantity ψ :

$$\langle \psi \rangle = \langle \psi^l \rangle + \langle \psi^s \rangle + \langle \psi^a \rangle \quad (5.4a)$$

$$= g^l \psi^l + g^s \psi^s + g^a \psi^a \quad (5.4b)$$

where volume fractions, g^ϕ , for each phase ϕ were used. Rappaz et al. [2003] define the volume fraction by writing a general expression inside the representative volume V_E :

$$g^\phi = \frac{1}{V_E} \int_{V_E} \chi^\phi(x, t) d\Omega = \langle \chi^\phi \rangle \quad (5.5)$$

where the integrated quantity is an indicator (or presence) function relative to phase ϕ , which defines the volume of this phase in the system, Ω^ϕ , as follows:

$$\chi^\phi(x, t) = \begin{cases} 1 & \text{if } x \in \Omega^\phi \\ 0 & \text{otherwise} \end{cases} \quad (5.6)$$

Any phenomenon that may displace an interface, whether by phase change or a phase motion, is mathematically translated by variations of the presence function, such that its total derivative for each phase satisfies the following:

$$\frac{d\chi^\phi}{dt} = \frac{\partial \chi^\phi}{\partial t} + \mathbf{v}^* \cdot \nabla \chi^\phi = 0 \quad (5.7)$$

Chapter 5. Macrosegregation with solidification shrinkage

If we consider the liquid phase, the variations of any quantity, named ψ , are given by:

$$\left\langle \frac{\partial \psi^l}{\partial t} \right\rangle = \frac{\partial \langle \psi^l \rangle}{\partial t} - \frac{1}{V_E} \int_{l-a} \psi^l \mathbf{v}^{l-a} \cdot \mathbf{n}^{l-a} dA - \frac{1}{V_E} \int_{l-s} \psi^l \mathbf{v}^{l-s} \cdot \mathbf{n}^{l-s} dA \quad (5.8)$$

$$\langle \nabla \psi^l \rangle = \nabla \langle \psi^l \rangle + \frac{1}{V_E} \int_{l-a} \psi^l \mathbf{n}^{l-a} dA + \frac{1}{V_E} \int_{l-s} \psi^l \mathbf{n}^{l-s} dA \quad (5.9)$$

$$\langle \nabla \cdot \psi^l \rangle = \nabla \cdot \langle \psi^l \rangle + \frac{1}{V_E} \int_{l-a} \psi^l \cdot \mathbf{n}^{l-a} dA + \frac{1}{V_E} \int_{l-s} \psi^l \cdot \mathbf{n}^{l-s} dA \quad (5.10)$$

[Equation \(5.7\)](#) can be recast with the level set method by using the smoothed Heaviside function in the metal. For the metal, this function is equal to one and decreases to zero in the air in a smooth way across both interfaces, solid-air and liquid-air. Since the solid phase is assumed fixed without possible deformation, and knowing that air is assumed incompressible, the solid-air interface does not move, leading to the following equation:

$$\frac{dH^M}{dt} = \frac{\partial H^M}{\partial t} + \mathbf{v}^{l-a} \cdot \nabla H^M = 0 \quad (5.11)$$

5.4 FE partitioned model

In this section, we start from a the monodomain finite element model presented in [section 2.1.1](#) that was relevant to the metal only, referred to by the superscript M , then present the essential assumptions and formulations that allow predicting solidification shrinkage in a Eulerian context that introduces another domain, the air, referred to by the superscript A .

5.4.1 In the metal

Mass and momentum conservation

By assuming a fixed solid phase ($\mathbf{v}^s = \mathbf{0}$), the average velocity in the metal reduces only to liquid's average velocity. Therefore, we can write:

$$\langle \mathbf{v} \rangle^M = \langle \mathbf{v}^l \rangle = g^l \mathbf{v}^l \quad (5.12)$$

With eq. (5.12), the mass balance in the metal writes:

$$\frac{\partial \langle \rho \rangle^M}{\partial t} + \nabla \cdot \langle \rho \mathbf{v} \rangle^M = 0 \quad (5.13a)$$

$$\frac{\partial \langle \rho \rangle^M}{\partial t} + \nabla \cdot \left(g^l \langle \rho \rangle^l \mathbf{v}^l \right) = 0 \quad (5.13b)$$

$$\frac{\partial \langle \rho \rangle^M}{\partial t} + \langle \rho \rangle^l \nabla \cdot \left(g^l \mathbf{v}^l \right) + g^l \mathbf{v}^l \cdot \nabla \langle \rho \rangle^l = 0 \quad (5.13c)$$

$$\nabla \cdot \langle \mathbf{v}^l \rangle = -\frac{1}{\langle \rho \rangle^l} \left(\frac{\partial \langle \rho \rangle^M}{\partial t} + \langle \mathbf{v}^l \rangle \cdot \nabla \langle \rho \rangle^l \right) \quad (5.13d)$$

Equation (5.13d) explains the flow due to shrinkage. A negative divergence term means that a liquid feeding is necessary to compensate for the density difference, hence acting as a flow driving force in the melt. Additional terms should appear in the other conservation equations, balancing the volume change in the heat and species transport.

When the metal's density was considered constant during solidification, the assumption of an incompressible system made it possible to use the Boussinesq approximation. However, in the case of solidification shrinkage, the average density $\langle \rho \rangle^M$ varies, as it depends on the solidification path as well as on $\langle \rho \rangle^s$ and $\langle \rho \rangle^l$ which are not equal nor constant. Therefore, the incompressibility condition may not be applicable. In such case, the earlier given system eq. (2.42) is reformulated without any reference value for density:

$$\begin{cases} \langle \rho \rangle^l \left(\frac{\partial \langle \mathbf{v}^l \rangle}{\partial t} + \frac{1}{g^l} \nabla \cdot (\langle \mathbf{v}^l \rangle \times \langle \mathbf{v}^l \rangle) \right) = \\ -g^l \nabla p^l - 2\mu^l \nabla \cdot (\bar{\nabla} \langle \mathbf{v}^l \rangle + \bar{\nabla}^t \langle \mathbf{v}^l \rangle) - g^l \mu^l \mathbb{K}^{-1} \langle \mathbf{v}^l \rangle + g^l \langle \rho \rangle^l \mathbf{g} \\ \nabla \cdot \langle \mathbf{v}^l \rangle = -\frac{1}{\langle \rho \rangle^l} \left(\frac{\partial \langle \rho \rangle^M}{\partial t} + \langle \mathbf{v}^l \rangle \cdot \nabla \langle \rho \rangle^l \right) \end{cases} \quad (5.14)$$

Energy conservation

In the energy equation, a volumetric source term accounts for the heat dissipation caused by the shrinking metal volume. Before writing the new equation, we make the following assumptions:

- consequence of the static solid phase: $\langle \rho h \mathbf{v} \rangle = g^l \langle \rho \rangle^l \langle h \rangle^l \mathbf{v}^l + \cancel{g^s \langle \rho \rangle^s \langle h \rangle^s \mathbf{v}^s} = g^l \langle \rho \rangle^l \langle h \rangle^l \mathbf{v}^l$

Chapter 5. Macrosegregation with solidification shrinkage

- the heat generated by mechanical deformation, $\mathbb{S} : \dot{\varepsilon}$, is neglected

The unknowns in the energy conservation are the average volumetric enthalpy $\langle \rho h \rangle^M$ and temperature T . The energy conservation equation writes:

$$\frac{\partial \langle \rho h \rangle^M}{\partial t} + \nabla \cdot (\rho h \mathbf{v})^M = \nabla \cdot (\langle \kappa \rangle^M \nabla T) \quad (5.15a)$$

$$\frac{\partial \langle \rho h \rangle^M}{\partial t} + \nabla \cdot (g^l \langle \rho \rangle^l \langle h \rangle^l \mathbf{v}^l) = \nabla \cdot (\langle \kappa \rangle^M \nabla T) \quad (5.15b)$$

$$\frac{\partial \langle \rho h \rangle^M}{\partial t} + \langle \mathbf{v}^l \rangle \cdot \nabla (\langle \rho \rangle^l \langle h \rangle^l) = \nabla \cdot (\langle \kappa \rangle^M \nabla T) - \langle \rho \rangle^l \langle h \rangle^l \nabla \cdot \langle \mathbf{v}^l \rangle \quad (5.15c)$$

$$\frac{\partial \langle \rho h \rangle^M}{\partial t} + \langle \mathbf{v}^l \rangle \cdot \nabla (\langle \rho \rangle^l \langle h \rangle^l) = \nabla \cdot (\langle \kappa \rangle^M \nabla T) + \langle h \rangle^l \left(\frac{\partial \langle \rho \rangle^M}{\partial t} + \langle \mathbf{v}^l \rangle \cdot \nabla \langle \rho \rangle^l \right) \quad (5.15d)$$

The second term in the RHS of eq. (5.15d) is a heat power (of unit $W m^{-3}$) that adds to the system in the mushy zone. This term is proportional to the solidification rate and expresses the heat generated in regions where the average density is changing and/or a gradient of liquid density is being advected.

Species conservation

The last conservation principle is applied to the chemical species or solutes. This principle allows predicting macrosegregation when applied to a solidification system, along with the mass, momentum and energy balances. However, the conservation equation should be reformulated in the case of a melt flow driven by shrinkage. Assumptions

- the solidification path is tabulated using thermodynamic data at equilibrium
- the macroscopic solute diffusion coefficient D^s in the solid phase is neglected in the mass diffusive flux term.
- consequence of the static solid phase: $\langle \rho w \mathbf{v} \rangle^M = g^l \langle \rho \rangle^l \langle w \rangle^l \mathbf{v}^l + \underline{g^s \langle \rho \rangle^s \langle w \rangle^s \mathbf{v}^s} = g^l \langle \rho \rangle^l \langle w \rangle^l \mathbf{v}^l$

The species conservation is pretty similar the energy conservation formulated in the previous section. The main difference is the breakup of the volumetric variable $\langle \rho w \rangle^M$ into a product of density $\langle \rho \rangle^M$ and the mass concentration $\langle w \rangle^M$. For a binary alloy,

we write:

$$\frac{\partial \langle \rho w \rangle^M}{\partial t} + \nabla \cdot \langle \rho w \mathbf{v} \rangle^M - \nabla \cdot \left(\langle D^l \rangle \nabla \left(\langle \rho \rangle^l \langle w \rangle^l \right) \right) = 0 \quad (5.16a)$$

$$\langle \rho \rangle^M \frac{\partial \langle w \rangle^M}{\partial t} + \langle w \rangle^M \frac{\partial \langle \rho \rangle^M}{\partial t} + \nabla \cdot \left(g^l \langle \rho \rangle^l \langle w \rangle^l \mathbf{v}^l \right) - \nabla \cdot \left(g^l D^l \nabla \left(\langle \rho \rangle^l \langle w \rangle^l \right) \right) = 0 \quad (5.16b)$$

$$\begin{aligned} & \langle \rho \rangle^M \frac{\partial \langle w \rangle^M}{\partial t} + \langle w \rangle^M \frac{\partial \langle \rho \rangle^M}{\partial t} + \left(\langle \rho \rangle^l \langle w \rangle^l \right) \nabla \cdot \langle \mathbf{v}^l \rangle + \langle \mathbf{v}^l \rangle \cdot \nabla \left(\langle \rho \rangle^l \langle w \rangle^l \right) \\ & - \nabla \cdot \left(g^l D^l \nabla \left(\langle \rho \rangle^l \langle w \rangle^l \right) \right) = 0 \end{aligned} \quad (5.16c)$$

The mass balance gives the following relation when the liquid density is constant:

$$\nabla \cdot \langle \mathbf{v}^l \rangle = -\frac{1}{\langle \rho \rangle^l} \left(\frac{\partial \langle \rho \rangle^M}{\partial t} \right) \quad (5.17)$$

If we use the result of eq. (5.17) in eq. (5.16c), then we get the following equation:

$$\langle \rho \rangle^M \frac{\partial \langle w \rangle^M}{\partial t} + \langle w \rangle^M \frac{\partial \langle \rho \rangle^M}{\partial t} = \langle w \rangle^l \frac{\partial \langle \rho \rangle^M}{\partial t} - \langle \mathbf{v}^l \rangle \cdot \nabla \left(\langle \rho \rangle^l \langle w \rangle^l \right) + \nabla \cdot \left(g^l D^l \nabla \left(\langle \rho \rangle^l \langle w \rangle^l \right) \right) \quad (5.18)$$

Applying Voller-Prakash [Voller et al. 1989] variable splitting, the system ends up with only one variable, $\langle w \rangle^M$. The splitting is done as follows:

$$\langle w \rangle^l = \left(\langle w \rangle^l \right)^t + \langle w \rangle^M - \left(\langle w \rangle^M \right)^t \quad (5.19)$$

where the superscript t refers to the previous time step. The chemical species conservation writes:

$$\begin{aligned} & \langle \rho \rangle^M \frac{\partial \langle w \rangle^M}{\partial t} + \cancel{\langle w \rangle^M \frac{\partial \langle \rho \rangle^M}{\partial t}} = \\ & \cancel{\langle w \rangle^M \frac{\partial \langle \rho \rangle^M}{\partial t}} - \langle \rho \rangle^l \langle \mathbf{v}^l \rangle \cdot \nabla \langle w \rangle^M + \nabla \cdot \left(g^l \langle \rho \rangle^l D^l \nabla \langle w \rangle^M \right) \end{aligned} \quad (5.20a)$$

$$+ \frac{\partial \langle \rho \rangle^M}{\partial t} \left[\left(\langle w \rangle^l \right)^t - \left(\langle w \rangle^M \right)^t \right] - \langle \rho \rangle^l \langle \mathbf{v}^l \rangle \cdot \nabla \left(\left(\langle w \rangle^M \right)^t - \left(\langle w \rangle^l \right)^t \right)$$

$$\begin{aligned} & \langle \rho \rangle^M \frac{\partial \langle w \rangle^M}{\partial t} + \langle \rho \rangle^l \langle \mathbf{v}^l \rangle \cdot \nabla \langle w \rangle^M - \nabla \cdot \left(g^l \langle \rho \rangle^l D^l \nabla \langle w \rangle^M \right) = \\ & - \frac{\partial \langle \rho \rangle^M}{\partial t} \left[\left(\langle w \rangle^M \right)^t - \left(\langle w \rangle^l \right)^t \right] + \langle \rho \rangle^l \langle \mathbf{v}^l \rangle \cdot \nabla \left(\left(\langle w \rangle^M \right)^t - \left(\langle w \rangle^l \right)^t \right) \\ & - \nabla \cdot \left[g^l \langle \rho \rangle^l D^l \nabla \left(\left(\langle w \rangle^M \right)^t - \left(\langle w \rangle^l \right)^t \right) \right] \end{aligned} \quad (5.20b)$$

$$\begin{aligned}
 & \langle \rho \rangle^M \frac{\partial \langle w \rangle^M}{\partial t} + \langle \rho \rangle^l \langle \mathbf{v}^l \rangle \cdot \nabla \langle w \rangle^M - \nabla \cdot (g^l \langle \rho \rangle^l D^l \nabla \langle w \rangle^M) = \\
 & - \frac{\partial \langle \rho \rangle^M}{\partial t} \left[(\langle w \rangle^M)^t - (\langle w \rangle^l)^t \right] \\
 & + \langle \rho \rangle^l \langle \mathbf{v}^l \rangle \cdot \nabla \left((\langle w \rangle^M)^t - (\langle w \rangle^l)^t \right) - \nabla \cdot \left[g^l \langle \rho \rangle^l D^l \nabla \left((\langle w \rangle^M)^t - (\langle w \rangle^l)^t \right) \right]
 \end{aligned} \tag{5.21}$$

It is noted that eq. (5.21) is valid only if both densities $\langle \rho \rangle^l$ and $\langle \rho \rangle^s$ are constant but have different values. Since density changes are incorporated in this equation, inverse segregation following solidification shrinkage is predicted. For the case where macrosegregation is solely due to fluid flow generated by natural or forced convection, i.e. no shrinkage occurs whether due to thermal-solutal contraction or phase change, the overall volume remains constant, hence density is constant. In this situation, $\langle \rho \rangle^s = \langle \rho \rangle^l = \langle \rho \rangle$ and the term $\partial \langle \rho \rangle / \partial t$ therefore vanishes. After dividing both sides by $\langle \rho \rangle = \langle \rho \rangle^l$, eq. (5.21) reduces to:

$$\begin{aligned}
 & \frac{\partial \langle w \rangle^M}{\partial t} + \langle \mathbf{v}^l \rangle \cdot \nabla \langle w \rangle^M - \nabla \cdot (g^l D^l \nabla \langle w \rangle^M) \\
 & = \langle \mathbf{v}^l \rangle \cdot \nabla \left((\langle w \rangle^M)^t - (\langle w \rangle^l)^t \right) - \nabla \cdot \left[g^l D^l \nabla \left((\langle w \rangle^M)^t - (\langle w \rangle^l)^t \right) \right]
 \end{aligned} \tag{5.22}$$

5.4.2 In the air

The presence of an air domain in our approach is important to follow the free surface of the solidifying metal. For this particular reason, some assumptions are introduced and explained in this section in order to limit unnecessary treatment within the air, since it does not undergo phase change. It should be reminded that we consider air as a single-phase system, hence superscripts A and a are interchangeably used.

Mass and momentum conservation

To simplify fluid flow resolution in the air, we consider it as incompressible. This assumption is acceptable in the context of casting processes where air velocity has an insignificant order of magnitude. Therefore, the free metal surface is not disturbed by air flow in its vicinity. With the incompressibility of air, we are saying that any deformation of the free surface is solely due to an air mass increase, coming from the system boundaries. The mass balance hence writes:

$$\nabla \cdot \langle \mathbf{v} \rangle^A = \nabla \cdot \mathbf{v}^a = 0 \tag{5.23}$$

The air flow is governed by time-dependent incompressible Navier-Stokes equations, as previously done for the metal:

$$\begin{cases} \langle \rho \rangle^a \left(\frac{\partial \mathbf{v}^a}{\partial t} + \nabla \cdot (\mathbf{v}^a \times \mathbf{v}^a) \right) = \\ - \nabla p^a - 2\mu^a \nabla \cdot \left(\bar{\nabla} \mathbf{v}^a + \bar{\nabla}^t \mathbf{v}^a \right) + \langle \rho \rangle^a \mathbf{g} \\ \nabla \cdot \mathbf{v}^a = 0 \end{cases} \quad (5.24)$$

The air density $\langle \rho \rangle^a$ is considered constant along the casting process, therefore thermal gradients in the air that arise due to the low thermal conductivity, do not generate any flow, i.e. no Boussinesq approximation is made on the term $\langle \rho \rangle^a \mathbf{g}$ in eq. (5.24).

Energy conservation

It was mentioned in the introduction of the current section that air is a single-phase system that cannot undergo any phase change. Therefore, heat transfer in this domain simplifies to pure thermal conduction with a low thermal conductivity coefficient, $\langle \kappa \rangle^a$. The energy balance governs the air enthalpy $\langle \rho h \rangle^A$ (which is equal to $\langle \rho \rangle^a \langle h \rangle^a$ in the current context) as follows:

$$\frac{\partial \langle \rho h \rangle^A}{\partial t} + \nabla \cdot \langle \rho h \mathbf{v} \rangle^A = \nabla \cdot (\langle \kappa \rangle^A \nabla T) \quad (5.25a)$$

$$\frac{\partial \langle \rho h \rangle^A}{\partial t} + \nabla \cdot (\langle \rho \rangle^a \langle h \rangle^a \mathbf{v}^a) = \nabla \cdot (\langle \kappa \rangle^a \nabla T) \quad (5.25b)$$

$$\frac{\partial \langle \rho h \rangle^A}{\partial t} + \mathbf{v}^a \cdot \nabla (\langle \rho \rangle^a \langle h \rangle^a) = \nabla \cdot (\langle \kappa \rangle^a \nabla T) \quad (5.25c)$$

Species conservation

The composition of alloying elements is crucial quantity to predict in this work. Nevertheless, such prediction is only relevant in the metallic alloy, even if the air is also made up of other chemical species (nitrogen, oxygen ...). For this obvious reason, the species conservation equation should not be solved in the air, but that of course is contradictory to the principle of a monolithic approach. Consequently, we should compute the conservation of chemical species in both the metal and the air, considering the latter as a *fictitious metal*, thus having initially the same solute mass composition, $\langle w_0 \rangle^M = \langle w_0 \rangle^A$. Then, we limit as much as possible solute transport between these domains by limiting solute advection and diffusion. The computed air velocity, \mathbf{v}^a ,

will not be used but rather a zero-velocity vector instead, thus suppressing the solute advection term influence. As for solute diffusion, a very low macroscopic solute diffusion coefficient is used, ensuring that its order of magnitude is at most a thousand times less than that in the melt, $D^a \ll D^l$. The low artificial diffusion in the air may slightly violate the wanted no-exchange condition at the air-liquid interface, but it is acceptable since suppressing the diffusion term in the air would result in a numerically stiff partial differential equation.

$$\langle \rho \rangle^A \frac{\partial \langle w \rangle^A}{\partial t} - \nabla \cdot (D^a \nabla (\langle \rho \rangle^a \langle w \rangle^a)) = 0 \quad (5.26)$$

In contrast to [eq. \(5.21\)](#) for the metal, solute balance in the air, given by [eq. \(5.26\)](#), provides a linear equation as we consider a special case where the domain is monophase, therefore: $\langle w \rangle^A = \langle w \rangle^a$ at all times. Otherwise, we would have applied the variable decomposition done earlier in [eq. \(5.19\)](#) to linearise the equation.

5.5 FE monolithic model

5.5.1 Monolithic equations

The monolithic model combines all conservation equations derived for metal and air in a unique set of equations, to be solved on a fixed mesh. This can be accomplished by using the Heaviside function (defined in [section 2.4.1](#)) relative to each domain, creating a mixture of properties that vary across the interface according to a specified mixing law. However, one of the main technical difficulties of the monolithic resolution is that the obtained equation should be consistent with each domain's original equation regarding its shape and terms, making its resolution easier. While for energy and solute balances the procedure is straightforward, the presence of the Darcy dissipative term in the metal's Navier-Stokes system makes it more difficult to formulate a single monolithic equation, which is discussed after writing the equations of the monolithic model.

Mass and momentum conservation

For the system's velocity, $\langle v^F \rangle$, is given by an arithmetic mixing between each domain's relative average fluid velocity, i.e. we need the relative fluid velocity with respect to other fixed/rigid phases in each domain. In the present context, the metal domain consists of a single fluid phase (liquid) and solid phases that form in fixed and rigid structures (assuming that solidification results in an undeformable columnar den-

dritic and eutectic structures, without any free equiaxed dendritic structure), while the latter domain entirely consists of a fluid phase (air). With this notation, we express the monolithic mass balance as:

$$\nabla \cdot \langle \mathbf{v}^F \rangle = \nabla \cdot \left(H^M \langle \mathbf{v} \rangle^M + H^A \langle \mathbf{v} \rangle^A \right) \quad (5.27)$$

$$\nabla \cdot \langle \mathbf{v}^F \rangle = H^M \nabla \cdot \langle \mathbf{v} \rangle^M + H^A \nabla \cdot \langle \mathbf{v} \rangle^A + \nabla H^M \cdot \left(\langle \mathbf{v} \rangle^M - \langle \mathbf{v} \rangle^A \right) \quad (5.28)$$

$$\nabla \cdot \langle \mathbf{v}^F \rangle = H^M \nabla \cdot \langle \mathbf{v}^l \rangle \quad (5.29)$$

where we used the relation [eq. \(5.12\)](#) in the case of a fixed rigid solid to obtain [eq. \(5.29\)](#). As for the second term in [eq. \(5.28\)](#), we have made the assumption that air is incompressible. Therefore any volume variation of the metal domain, will trigger an air inflow or suction effect through the surface boundaries of the air domain. The third and last term in the same equation expresses a velocity jump at the interface. In our case, we neglect this contribution by assuming that both velocities tend to be equal when the interface thickness tends to zero. Finally, the monolithic mass balance writes:

$$\nabla \cdot \langle \mathbf{v}^F \rangle = H^M \left(-\frac{1}{\langle \rho \rangle^l} \left(\frac{\partial \langle \rho \rangle^M}{\partial t} + \langle \mathbf{v}^l \rangle \cdot \nabla \langle \rho \rangle^l \right) \right) \quad (5.30)$$

The momentum balance looks like the one derived for the metal, but using level set mixed properties, we get the following:

$$\begin{cases} \hat{\rho} \left(\frac{\partial \langle \mathbf{v}^F \rangle}{\partial t} + \frac{1}{g^F} \nabla \cdot (\langle \mathbf{v}^F \rangle \times \langle \mathbf{v}^F \rangle) \right) = \\ - g^F \nabla p - 2\hat{\mu} \nabla \cdot \left(\overline{\nabla} \langle \mathbf{v}^F \rangle + \overline{\nabla}^t \langle \mathbf{v}^F \rangle \right) - g^F \hat{\mu} \tilde{\mathbb{K}}^{-1} \langle \mathbf{v}^F \rangle + \hat{\rho} g \mathbf{g} \\ \nabla \cdot \langle \mathbf{v}^F \rangle = H^M \left(-\frac{1}{\langle \rho \rangle^l} \left(\frac{\partial \langle \rho \rangle^M}{\partial t} + \langle \mathbf{v}^l \rangle \cdot \nabla \langle \rho \rangle^l \right) \right) \end{cases} \quad (5.31)$$

Chapter 5. Macrosegregation with solidification shrinkage

Note that the Darcy term has a special treatment explained in the next section. The mechanical properties are mixed as follows:

$$\text{Fluid fraction : } g^F = H^M g^l + H^A g^a = H^M g^l + H^A \quad (5.32)$$

$$\text{Density : } \hat{\rho} = H^M \langle \rho \rangle^l + H^A \langle \rho \rangle^a \quad (5.33)$$

$$\text{Dynamic viscosity : } \hat{\mu} = H^M \mu^l + H^A \mu^a \quad (5.34)$$

$$\text{Weight force : } \hat{\rho} \hat{g} \mathbf{g} = H^M g^l \langle \rho \rangle^l \mathbf{g} + H^A g^a \langle \rho \rangle^a \mathbf{g} = H^M g^l \langle \rho \rangle^l \mathbf{g} + H^A \langle \rho \rangle^a \mathbf{g} \quad (5.35)$$

We defined a fluid fraction, g^F , as an arithmetic mixing between liquid and air fractions across the interface. This quantity will be essential for the monolithic Darcy term. As for the weight force in both domains, it is taken into account via eq. (5.35). The phase densities may vary as functions of other parameters such as temperature or phase composition ($\langle \rho \rangle^l$ depends on both), creating buoyancy forces of convection inside the fluid. In our approach, since we are only interested in liquid's flow, we keep the air phase density $\langle \rho \rangle^a$ constant, so as to prevent a mixture of forces around the level set, which helps stabilise the fluid flow resolution.

Energy conservation

Deriving the monolithic energy conservation equation is straightforward. The monolithic system writes:

$$\frac{\partial \widehat{\langle \rho h \rangle}}{\partial t} + \langle \mathbf{v}^F \rangle \cdot \nabla \widehat{(\rho h)^F} = \nabla \cdot (\widehat{\langle \kappa \rangle} \nabla T) + \widehat{\Phi} \quad (5.36)$$

The solution of eq. (5.36) is $\widehat{\langle \rho h \rangle}$, a mixed field between both domains average volumetric enthalpies. The other parameters are $\widehat{(\rho h)^F}$ and $\widehat{\langle \kappa \rangle}$ which denote respectively the fluids' mixture volume enthalpy and the mixture of average thermal conductivities. The last term, $\widehat{\Phi}$, is an average heat source accounting for energy change caused by the alloy's shrinking volume. As no volume change was considered for the air, $\widehat{\Phi}$ is present only in the metal's energy balance. These quantities are defined in the following equa-

tions:

$$\text{Total enthalpy : } \widehat{\langle \rho h \rangle} = H^M \langle \rho h \rangle^M + H^A \langle \rho h \rangle^A \quad (5.37)$$

$$\text{Fluid phases enthalpy : } \widehat{\langle \rho h \rangle^F} = H^M \langle \rho \rangle^l \langle h \rangle^l + H^A \langle \rho \rangle^a \langle h \rangle^a \quad (5.38)$$

$$\text{Average thermal conductivity : } \widehat{\langle \kappa \rangle} = H^M \langle \kappa \rangle^M + H^A \langle \kappa \rangle^A \quad (5.39)$$

$$\text{Average heat change : } \widehat{\Phi} = H^M \langle \rho \rangle^l \langle h \rangle^l \nabla \cdot \langle \mathbf{v}^l \rangle \quad (5.40)$$

Species conservation

As previously explained in [section 5.4.2](#), we consider that species conservation is solved over both domains, as follows:

$$\begin{aligned} & \langle \rho \rangle^M \frac{\partial \widehat{\langle w \rangle}}{\partial t} + \langle \rho \rangle^l \langle \mathbf{v}^l \rangle \cdot \nabla \widehat{\langle w \rangle} - \nabla \cdot \left(g^l \langle \rho \rangle^l D^l \nabla \widehat{\langle w \rangle} \right) = \\ & - \frac{\partial \langle \rho \rangle^M}{\partial t} \left[\left(\langle w \rangle^M \right)^t - \left(\langle w \rangle^l \right)^t \right] \\ & + \langle \rho \rangle^l \langle \mathbf{v}^l \rangle \cdot \nabla \left(\left(\langle w \rangle^M \right)^t - \left(\langle w \rangle^l \right)^t \right) - \nabla \cdot \left[g^l \langle \rho \rangle^l D^l \nabla \left(\left(\langle w \rangle^M \right)^t - \left(\langle w \rangle^l \right)^t \right) \right] \end{aligned} \quad (5.41)$$

then we deduce the metal's solute composition by postprocessing the obtained solution.

We have seen in the previous chapter that adding the Darcy term into Navier-Stokes system modifies the shape of the equation, dividing all terms by the liquid fraction, g^l (REF VMS SOLVER CHAPTER 4). The presence of this dissipation term in one domain, obliges us to keep it in both domains but "deactivate" it where it is useless, i.e. in the air. This is done by computing a fictitious permeability in the air as function of the air fraction using the Carman-Kozeny model, as used previously for the metal in [eq. \(1.3\)](#). We may speak of level set mixing for the Darcy term. It has a double advantage:

1. the consistency in shape is kept between both domains equations, thus easily deriving the monolithic system;
2. since the monolithic system retains the shape of the monodomain equation, the VMS solver does not require further implementation updates and subsequent validation.

$$\tilde{\mathbb{K}} = \frac{\lambda_2^2 g^{F^3}}{180 (1 - g^F)^2} \quad (5.42)$$

Chapter 5. Macrosegregation with solidification shrinkage

then from the fluid fraction (eq. (5.32)), we deduce a modified permeability, \tilde{K} . Depending on the values of this quantity, the extent to which the Darcy becomes imposing in Navier-Stokes varies as follows:

- $\tilde{K}^{-1} \rightarrow 0$ (completely permeable), then Darcy's term is negligible in Navier-Stokes resolution,
- $\tilde{K}^{-1} > 0$ (slightly permeable), then fluid flow is greatly dissipated due to a decreasing permeability,
- $\tilde{K}^{-1} \rightarrow \infty$ (non permeable), then no fluid flow may exist.

These 3 cases are graphically represented in fig. 5.4, showing the different values along with the transitions with respect to phases and domains distribution. It is clear that neither in liquid nor air, the flow is dissipated by the presence of the Darcy term in the monolithic system, which is confirmed in REF FIGURE DRAW DARCY/PERMEABILITY FROM LIQUID FRACTION RESULT.

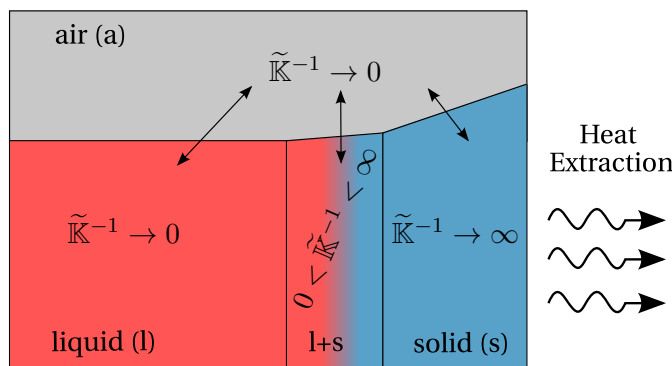


Fig. 5.4 – Schematic representation of an ingot undergoing solidification while shrinking. The inverse of the modified permeability, \tilde{K}^{-1} , falls to zero in the air and liquid phases, indicating that the Darcy term is only activated in the solid and liquid+solid regions. The arrows indicate three different transitions of the Darcy term between the air and metal domains.

5.6 1D application: solidification with inverse segregation

5.6.1 Geometry and boundary conditions

A simple but very efficient way of analysing the model is to test it through a 1D flow configuration with energy and species conservation. For this purpose, we take an aluminium-silicon alloy with the same properties used for the thermal solver validation in [table 3.2](#). The major difference with respect to the former validation setup is the air domain that should also be included in the mesh. We consider a 2D rod having as dimensions $0.14\text{ m} \times 0.001\text{ m}$, where initially the air column's height is only 0.04 m and the remainder of the length is for the metal. **FIGURE** shows the geometry, mesh used for this section simulations, while **FIGURE** shows the thermal and mechanical boundary conditions. In the latter, velocity-slip conditions were imposed on the lateral boundaries while a no-slip was used at the bottom where heat is extracted, to ensure a 1D air flow from the free air inlet at the top.

In this case, imposing slip conditions on lateral sides is two-fold: on one hand, we need to ensure that the fluid flow solution remain one-dimensional, hence symmetry on the boundaries solves the issue, while on the other hand during solidification, the resulting feeding flow should be able to transport the interface intersecting with boundary nodes. If boundary velocities are zero, then the interface transport will face problems at these boundary nodes. This is indeed an important and relevant point in the next 2D test case.

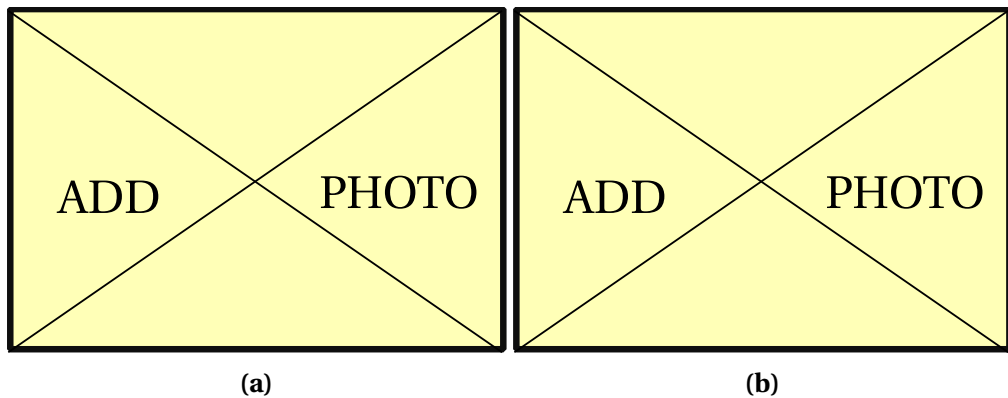


Fig. 5.5 – Geo and boundary conditions

5.6.2 Shrinkage without macrosegregation

The first simulation is the solidification without any segregation, hence a unique solidification path is considered at $w_0 = \text{Al-7 wt.\% Si}$, shown in [fig. 5.7](#). This case is

interesting as a reference case, where we can study volume shrinkage and level set behaviour in a simple segregation-free configuration. We first use a homogeneous isotropic mesh of constant size $h = 200 \mu\text{m}$. The liquid and solid phase densities are assumed constant and respectively equal to 2600 kg m^{-3} and 2800 kg m^{-3} . This density difference is equivalent to a ratio of $\beta_{SS} = (\langle \rho \rangle^s - \langle \rho \rangle^l) / \langle \rho \rangle^s$, also termed as *solidification shrinkage* by [Flemings and Nereo \[1967\]](#). In the current conditions, β_{SS} is constant and equal to 7.14 %. The domain is initially meshed before any resolution, as shown in [fig. 5.6](#), in a way to reduce interpolation errors that may cause coarse elements within the transition of fluids density and dynamic viscosity, reminding that these parameters are crucial for the stability of the velocity solution used later in the transport step. The chosen mixing laws are arithmetic for the density and logarithmic for the viscosity. The choice is based on tests done in former Ph.D. projects at CEMEF. The initial mesh sizes are given in [table 5.1](#).

Table 5.1 – Summary of the different mesh sizes used to generate an adaptive anisotropic mesh, along with the level mixing thickness, ε . Refer to [section 2.6.2](#) for the definition of each mesh parameter.

Mesh parameter	Size [m]
ε	2.5×10^{-4}
h_n	2.5×10^{-5}
h_τ	2×10^{-4}
h_M	1.5×10^{-4}
h_A	2.5×10^{-4}

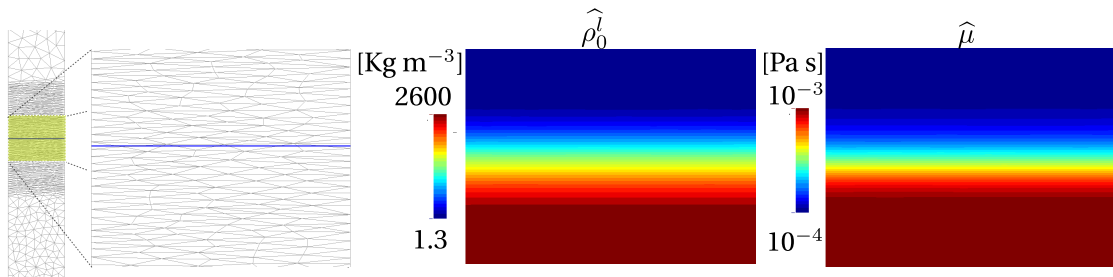


Fig. 5.6 – Snapshots of the initial adapted mesh around the interface with different mesh sizes in the air and the metal. The adapted region is stretched beyond the level set mixing thickness to ensure better interpolation around the interface, in case of emergence of diffusion instabilities. To the right, the reference fluid density and viscosity are plotted in the transition zone, showing a symmetric mixing for the former and a shifted mixing for the latter, as a consequence of the mixing laws. The thick blue line represents the zero isovalue of the distance function.

At a first glance, results show that the interface stability is compromised by a chosen

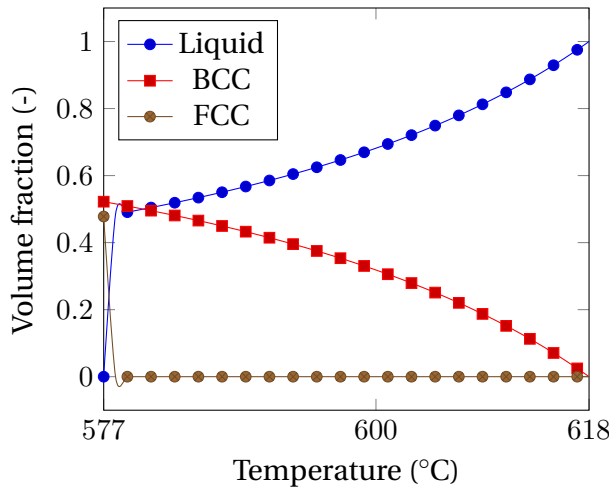


Fig. 5.7 – Unique solidification path at nominal composition for the shrinkage case without macrosegregation.

time step for a given mesh size, and that the interface dynamics require attention even before investigating the feeding flow created by solidification. As a demonstration, [fig. 5.8](#) shows different time steps with the same adaptive meshing parameters. For time steps greater than 0.01 s, Navier-Stokes computations did not converge resulting in an high artificial flow quickly destabilising the interface. It should be noted that the frame corresponding to 0.02 s was taken at an earlier time than the two other frames. Although no solidification has yet started at 100 s, a two-dimensional flow is observed around the interface, while tends to 10^{-8} m s^{-1} elsewhere in the ingot. [Figure 5.8](#) confirms that this flow is still predicted at smaller time steps. This flow seems like a pure numerical response to the properties jump across the interface, namely density and dynamic viscosity. It is also noted that the interface position is not modified by the neighbouring currents, that reach a maximum magnitude of 10^{-4} m s^{-1} . Therefore, the optimal time step for this simulation is set to 0.01 s, and we refer to it as case R, which stands for "real" air.

The fact that properties transition is crucial in the solution stability, is investigated by 2 reference cases, having equal properties (density and dynamic viscosity) but with different time steps, 0.01 (case A1) and 0.1 s (case A2), where "A" stands for artificial. All simulation cases are grouped in [table 5.2](#).

When the air subdomain is given the metal's properties, it becomes denser and more viscous by several orders of magnitude. [Figure 5.9](#), in which cases A1 and A2 are compared, shows no noticeable sign of velocity instability near the interface before 200 s. It can be explained by the fact that the air behaves mechanically like a fluid metal given similar properties, therefore no steep transitions are computed at the

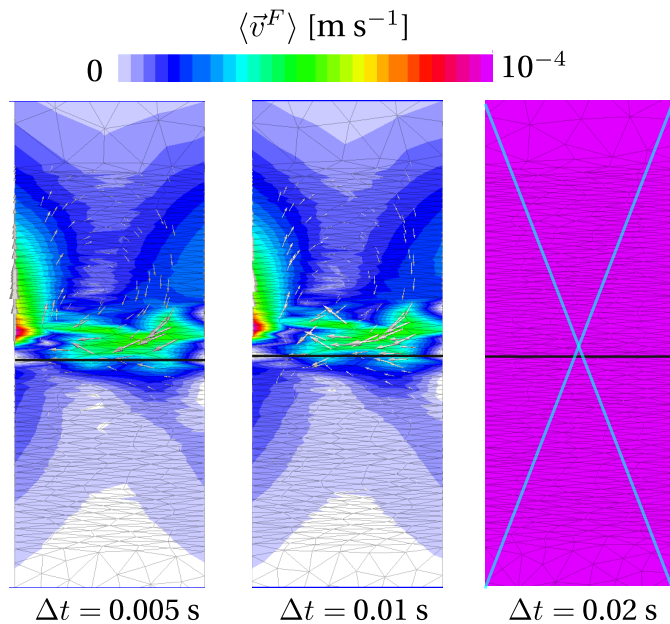


Fig. 5.8 – Three average fluid velocity frames at different time steps: 0.005 s, 0.01 s and 0.02 s. The first and second frame are taken after 50 seconds of cooling while for the last frame, the frame was taken after only 1 second of cooling, thus it is crossed to show non-convergence. The thick black line represents the zero isovalue of the distance function.

Table 5.2 – Summary of the comparative shrinkage simulations without macrosegregation.

Case	Air viscosity [Pa s]	Air density [kg m^{-3}]	Time step [s]
A1	10^{-3}	2600	0.01
A2	10^{-3}	2600	0.1
R	10^{-4}	1.3	0.01

5.6. 1D application: solidification with inverse segregation

interface. However, it is interesting to compare results of [fig. 5.9a](#) and [fig. 5.9b](#) at 600 s. For case A1, the interfaces is slightly skewed due to slower flow at the left side of the interface, while for case A2, the flow disturbs the interface deforming it until the end of solidification, as seen at 1000 s. This shows the importance of the chosen time step in both the Navier-Stokes solver. We can also notice a common issue for all three case, A1, A2 and R, approximately at 400 s, the mushy zone enters within the diffuse interface, affecting the level set transport and thus causing mass conservation problems. These problems are discussed in the next section.

In contrast, [fig. 5.10b](#) shows more viable results as far as the level set transport is concerned. From 200 s to 800 s, the local flow instability (discussed earlier in [fig. 5.8](#)) is sustained, even until after solidification is complete. However, in regions of 100% metal and 100% air the computed velocity is nearly the same order of magnitude as predicted for all three simulations. Finally, in [fig. 5.10b](#), we notice a recirculating air flow in the vicinity of the interface as no metal shrinkage may further occur once solidification is complete, thus air flows freely in and out of the upper boundary with a very low magnitude ($\sim 10^{-7} \text{ m s}^{-1}$), while impinging on the air-metal surface. Regarding the CPU times, cases A1 ran for 14 hours, case A2 took only 2 hours while case R ran for 23.3 hours.

Mass conservation study

The previous computations showed that the mass conservation, which is the consequence of the level set transport, can be lost. In order to better understand the process, we define the metal's mass as a function of the metal's average density and the Heaviside function relative to the metal subdomain, as follows:

$$m^M = \int_{\Omega} H^M \langle \rho \rangle^M \, d\Omega \quad (5.43)$$

Then, the mass conservation can be monitored by processing [eq. \(5.43\)](#) at each time step, and computing the relative mass change by writing:

$$m_{\%}^M = \frac{m^M - m_i^M}{m_i^M} \times 100 \quad (5.44)$$

The relative mass change gives us information on the level set transport. As the current case is 1D and phase densities are constant throughout the simulation, mass conservation can be checked by a much simpler than by checking [eq. \(5.44\)](#). Since we know the initial metal's column length, l_0^M , and the expected solidification shrinkage is 7.14 %, we should expect a final length of $l_f^M = (1 - \beta_{SS}) l_0^M = 0.09286 \text{ m}$. How-

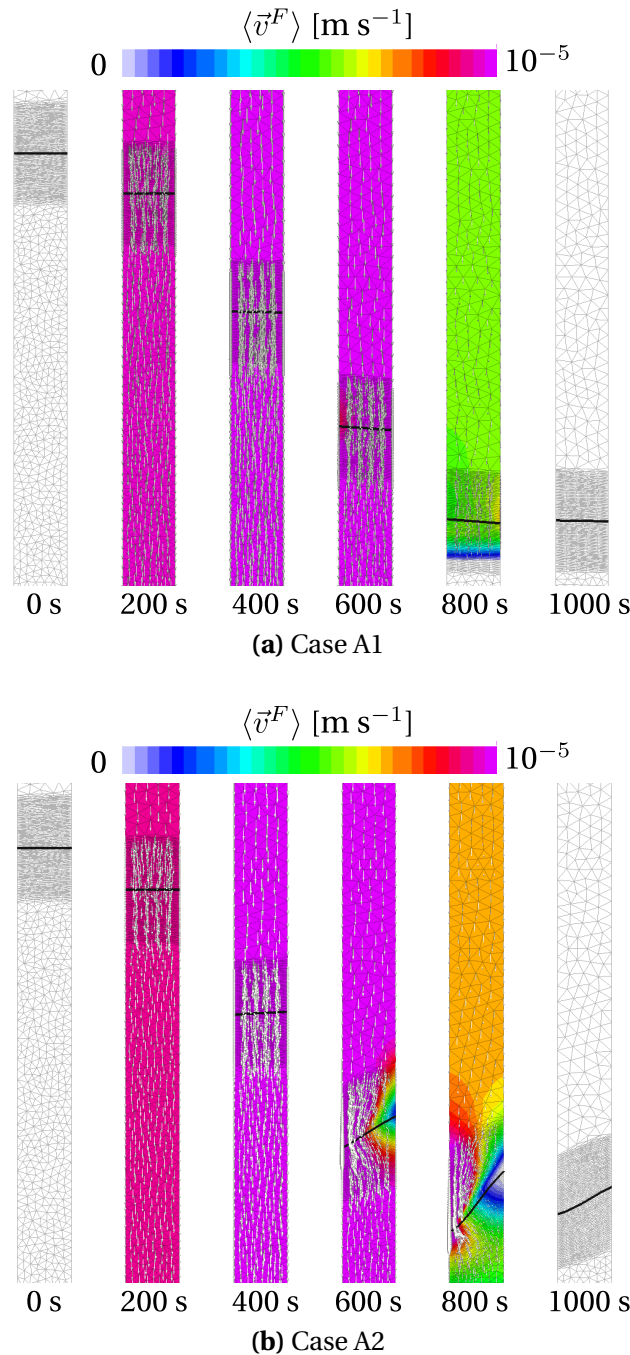


Fig. 5.9 – Comparison of two simulations in several stages of solidification ending shortly after 800 s. The results shows the influence of density and viscosity properties across the level set interface. The plotted field is the average fluid velocity, on which the corresponding nodal vectors are superimposed, pointing towards the solidification front. The thick black line represents the zero isovalue of the distance function.

5.6. 1D application: solidification with inverse segregation

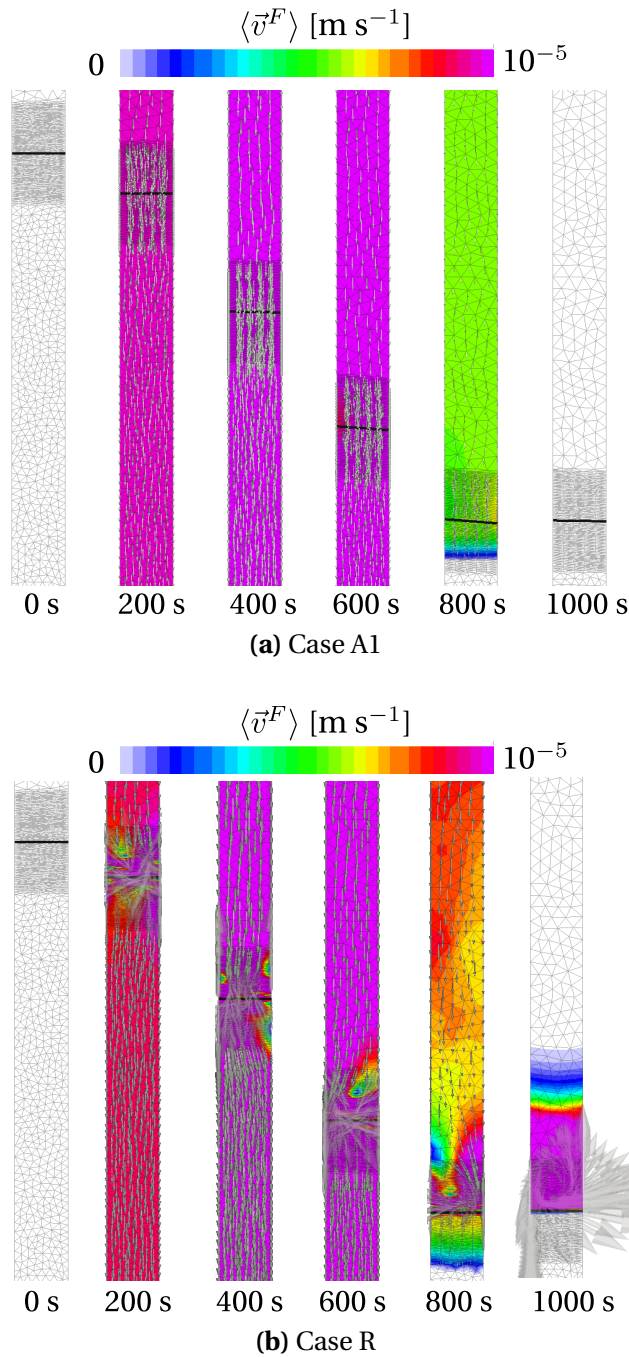


Fig. 5.10 – Comparison of two simulations in several stages of solidification ending shortly after 800 s. The results shows the influence of density and viscosity properties across the level set interface. The plotted field is the average fluid velocity, on which the corresponding nodal vectors are superimposed, pointing towards the solidification front. The thick black line represents the zero isovalue of the distance function. The vectors were made transparent in the transition zone so as not to hide the interface level.

ever, this equation is very useful and applicable in 2D and 3D cases of solidification shrinkage.

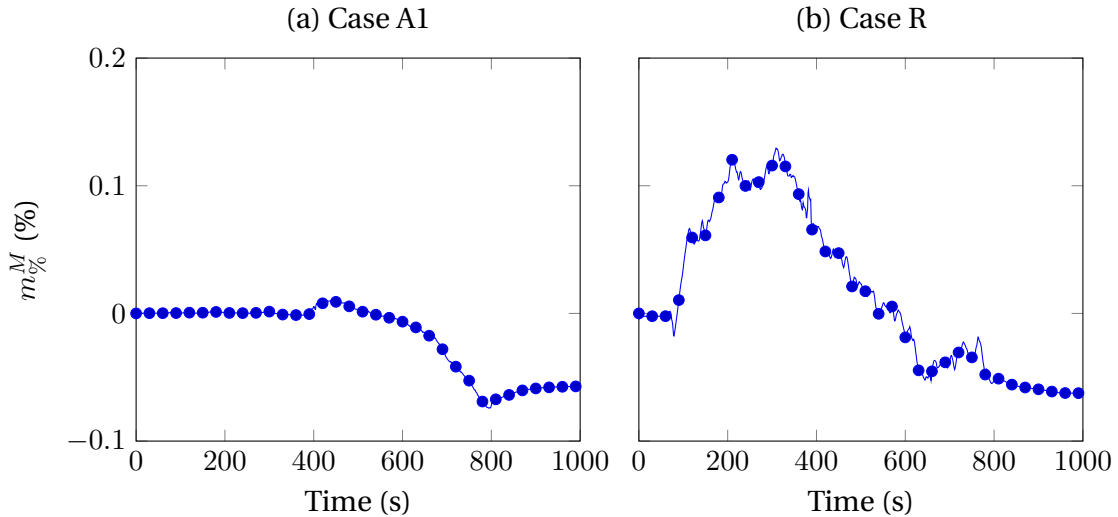


Fig. 5.11 – Variation of the metal’s mass versus solidification time in cases A1 and R.

In the previous section, we observed transport problems taking place around 400 s of cooling. Although it was clearly seen in [fig. 5.9b](#), it applies for both cases, whether air properties are equal or different than the liquid’s properties across the interface. The mass variation plots in [fig. 5.11](#) confirm these observations. Therefore, we can deduce that regardless of the time step and the level set mixing of properties, transport problems may occur.

The level set method is known to have poor mass conservation properties. However, the mass variation we see in the previous plots is more related to a physical problem: **at which velocity does the interface move?** In our simulations, we systematically considered the Navier-Stokes solution $\langle v^F \rangle$, to transport the metal-air interface. This solution is equal to $\langle v^l \rangle = g^l v^l$ in the metal subdomain. However in reality, between the metal and the air, two interfaces exist: the liquid-air ($l-a$) and solid-air ($s-a$) interfaces, and these interfaces move at different velocities as solidification proceeds. The liquid-air interface exists at early stages of solidification where only liquid is in contact with the air. In later stages, the mushy zone delimited by dendrite tips, reaches the free liquid surface, creating hence these distinct interfaces: a first interface separating interdendritic liquid from the air, and a second interface that separates the dendrites also from the air. The $l-a$ interface is driven by solidification shrinkage and therefore by the real microscopic velocity of the interdendritic liquid, v^l . According to [Dantzig and Rappaz \[2009\]](#), this velocity is constant when the solidification shrinkage and the

5.6. 1D application: solidification with inverse segregation

isotherms velocity v_T are constant, as states the equation:

$$v^l = -\beta_{SS} v_T \quad (5.45)$$

As for the $s-a$ interface, its motion is induced by a mechanical deformation of the solid phase either due to thermal shrinkage or external mechanical stresses. The first factor is ubiquitous in any solidification process, while the second factor is process-dependent. In the present work, we remind that the solid phase is assumed fixed and rigid, therefore we consider dendrites to be undeformable during their growth. Unfortunately, this assumption is contradictory with our current situation where the metal keeps shrinking, until an overlap between the level set's diffuse interface and the mushy zone overlap, as shown in fig. 5.12). At this stage, tracking a single interface induces concept errors, because we are not sure which of the previously mentioned interfaces is being tracked, and hence failing to determine an adequate transport velocity field.

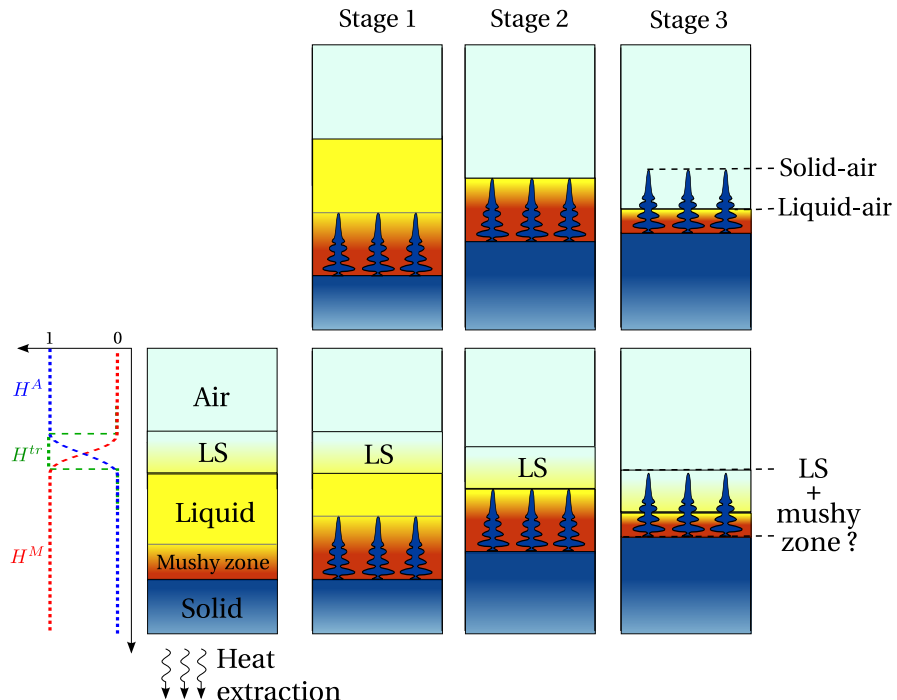


Fig. 5.12 – Schematic describing the physical (first row) and numerical (second row) process of moving an interface between air and metal subdomains, in three intermediate stages of solidification.

In the light of these facts, we will try to limit as much as possible the interface motion, once the mushy zone has reached the diffuse interface. To do so, we firstly advise to keep a very small thickness interface, in order to delay the previously explained

overlap. Moreover, we suggest computing the transport velocity, used in eq. (2.60), at each node j as follows:

$$v = \begin{cases} \langle v^l \rangle_j & \text{if } g_j^l > g^{BL} \\ 0 & \text{otherwise} \end{cases} \quad (5.46)$$

where g^{BL} is the threshold for the liquid fraction, below which we consider that the interface should not be transported. Figure 5.13 shows the mass variation for three blocking fractions: 0, 50, 75 and 99 percent. The first value corresponds the case where the Navier-Stokes solution is directly passed to the transport solver. For the last value, the portion of the interface in contact with the low solid fraction part of the mushy zone becomes immobile. It is clearly seen that the consequence on the mass conservation is not very good, as the mass increases up to 3% while the eutectic front is consuming the liquid within the mushy zone, while no further shrinkage is allowed.

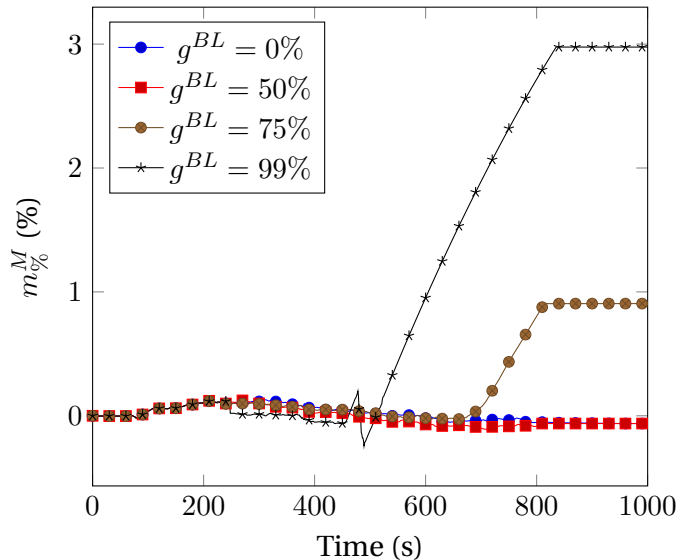


Fig. 5.13 – Relative mass change versus time for different blocking fractions g^{BL} in the transport solver.

In fig. 5.14, we plot again the same curves as in fig. 5.13, but keeping the values of $g^{BL}=0\%$ and $g^{BL}=50\%$. We notice that both values produce the same results until about 300 s. Then, when the mushy zone reaches the interface region, differences appear as a consequence of the reduced transport for the higher blocking fraction. However, it should be pointed out that the differences between 300 s and 800 s are not important because the permeability predicted by the Carman-Kozeny model, falls to zero quickly for liquid fractions less than about 60%.

In the current application, it is not clear whether the idea of the blocking fraction is

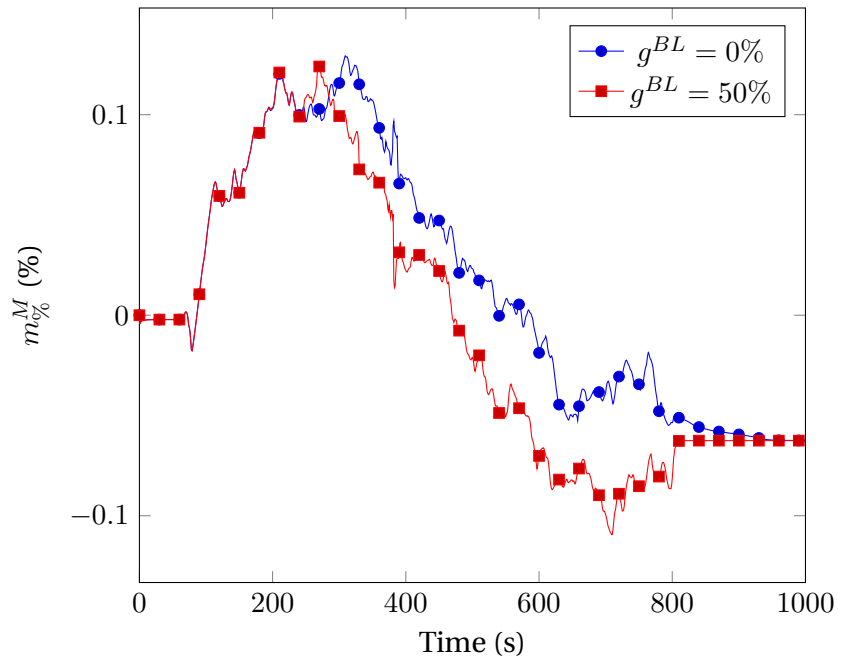


Fig. 5.14 – Relative mass change versus time only for 0% and 50% blocking fractions.

useful or not, since the feeding flow occurs in a single direction and solidification takes place far from the interface. Therefore, it is interesting to test again in the coming 2D and 3D applications to see if it yields advantages on the final shape of the interface.

5.6.3 Shrinkage with macrosegregation

in this section, we consider species conservation equation, in addition to energy conservation and fluid momentum conservation equations, used in the previous section to predict solidification shrinkage. The interesting point here is to study the formation of macrosegregation in a one-dimensional configuration and the effect of solidification shrinkage on it. As shown in chapter 2, our approach to solve the energy equation relies on tabulations of various solidification paths. In this case, we will generate a simple tabulation based on a phase diagram with linear liquidus and solidus lines, whose properties are reminded in [table 5.3](#)

Using the values from [table 5.3](#), a python program generates a *CimLib* compatible tabulation assuming lever rule as microsegregation law, with a 0.1 wt.% step for average composition within an offset of 20% around the nominal value. For temperature, a cooling range between T_E and 630 °C is considered with a step of 1 °C. It is noted that for this application, the phase enthalpies are deduced from constant specific heat of each phase as well as constant latent heat.

Chapter 5. Macrosegregation with solidification shrinkage

Table 5.3 – Main properties of the linearised phase diagram for Al-Si alloys.

Parameter	Symbol	Value	Unit
Nominal composition	$\langle w \rangle_0$	7	wt.%
Liquidus temperature	T_l	618	°C
Eutectic temperature	T_E	577	°C
Segregation coefficient	k	0.13	—
Liquidus slope	m_l	-6.5	K wt.% ⁻¹

In order to understand better the effect of shrinkage combined with macrosegregation, we plot in [fig. 5.15](#), the cooling curves from 4 different simulations:

- Gray curve - case G0: pure diffusion solidification with $\langle \rho \rangle^l = \langle \rho \rangle^s$ (no level set) used previously in chapter 2 for validation; we use it as a reference case,
- Green curve - case G: convection-diffusion solidification with $\langle \rho \rangle^l = \langle \rho \rangle^s$ (with level set) at a constant average composition
- Blue curve - case B: convection-diffusion solidification with $\langle \rho \rangle^l \neq \langle \rho \rangle^s$ (with level set) at a constant average composition; this curve is plotted in [fig. 5.15a](#) and [fig. 5.15b](#),
- Red curve - case R (not to be confused with case R defined in the previous section): convection-diffusion solidification with $\langle \rho \rangle^l \neq \langle \rho \rangle^s$ (with level set) and macrosegregation.

Shrinkage effect on temperature

If we focus first on [fig. 5.15a](#), we first compare solidification cases G and G0, both with equal phase densities, hence no shrinkage. This first comparison shows that the introduction of the level set method, compared to a monodomain configuration, heats up the overall sample temperature by about 5 °C, causing solidification to finish a few seconds later than predicted in case G0. This is because we set a very high initial temperature in the air, 800 °C, to prevent a brutal diffusive flux that may lead to surface solidification in the metal. As the sample cools down, the air conductivity ($10^{-2} \text{ W m}^{-1} \text{ K}^{-1}$) is not low enough to prevent a small diffusion flux in the metal's direction. However, since in both cases the cooling trend is predicted, we will keep the same thermal diffusion properties in the air, so as not to use unreal conductivity values, but we keep in mind that the current approach delays the solidification.

The second comparison is done between cases G and B, both using the level set approach but only case B considers solidification shrinkage. We notice that blue curve

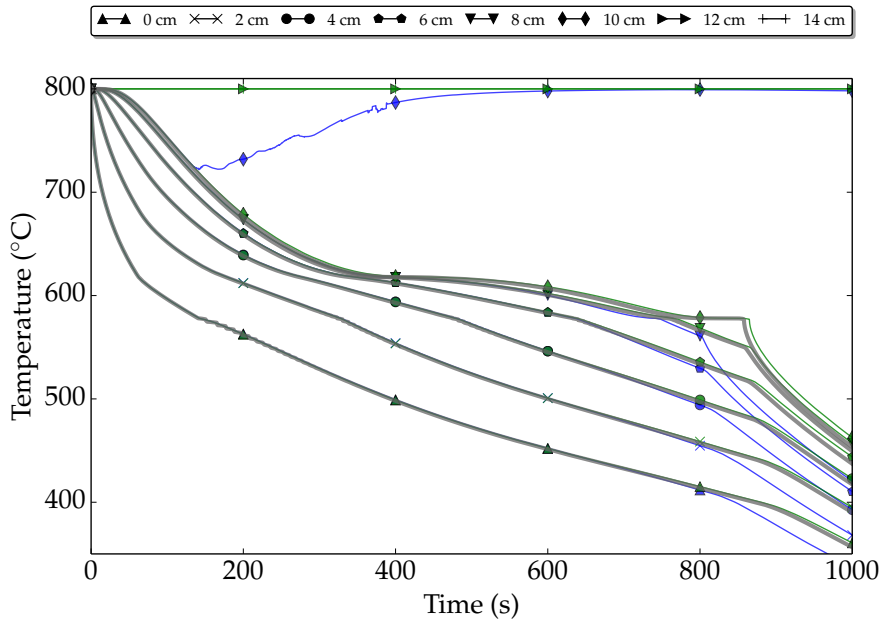
5.6. 1D application: solidification with inverse segregation

temperature of the sixth Eulerian sensor rises steadily from 180 s to 600 s reaching a constant temperature of 800 °C, the air's temperature. This rise confirms the metal has shrunk in length (volume in 3D), becoming less than 10 cm, hence replaced by air that entered through the open top boundary. The sensors at 12 cm and 14 cm are not shown in this figure as the simulation done for the pure diffusion without level set, the air subdomain does not exist. Another interesting difference resulting from shrinkage is that solidification ends sooner by about 70 s, compared to the pure diffusion case. As mass is almost perfectly conserved in both cases, cooling flux is the only factor that may accelerate the cooling. The imposed cooling boundary condition is a Fourier-type with the same heat transfer coefficient h_{ext} in both cases. However, a shrinkage flow transports energy in its direction, i.e. towards the solidification front, and thus raising slightly the temperature in regions close to the cool wall. Therefore, the Fourier flux proportional to the temperature difference $(T - T_{\text{ext}})$ increases and the sample solidifies earlier.

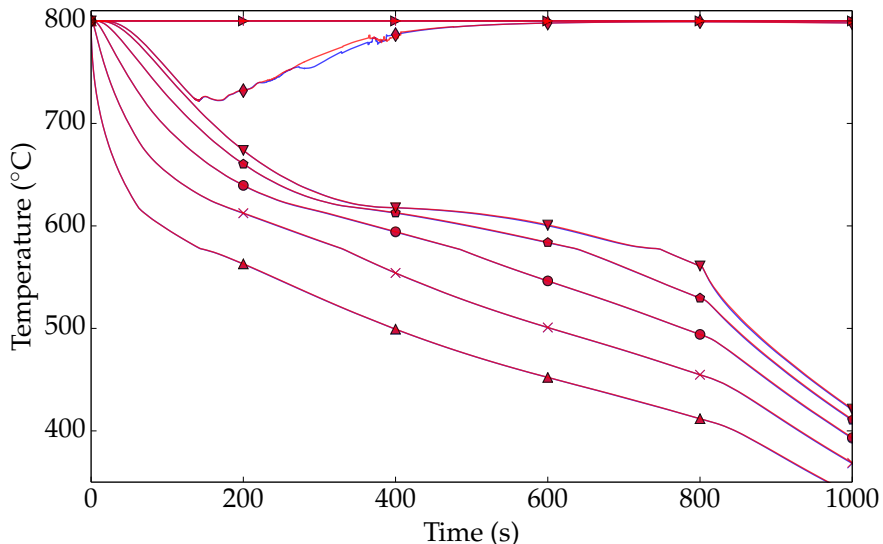
Finally, [fig. 5.15b](#) compares cases B and R, both with unequal phase densities but only predicting macrosegregation in the latter case. Differences are not striking, as temperatures along the metal sample are the same. We spot however a difference at the 10 cm probe, where a slight rise in temperature is observed with respect to the case without macrosegregation.

Shrinkage effect on average composition

[Figure 5.16](#) shows snapshots at different times of the shrinkage flow caused by the density difference between liquid and solid phases. By solid phases, we mean the primary solid phase assumed in a dendritic structure, then the primary and secondary solid phases form together the eutectic that we see starting at 150 s in [fig. 5.16](#). We can see that some solute segregation has already initiated in the mushy zone at 100 s. However, the average composition reaches a positive peak of $\langle w \rangle = \text{Al-7.5 wt.\% Si}$ (CHANGE VALUE ACCORDING TO PLOT) with the initiation and progression of the eutectic front. The sudden transformation of the remaining liquid in the mushy zone into eutectic solid, triggers a local velocity increase (real intrinsic velocity) as each node's density varies from $\langle \rho \rangle^l$ to $\langle \rho \rangle^s$ in a single time step, at eutectic temperature. The velocity increase, shown later in [fig. 5.18](#), causes species transport in the opposite direction of solidification, hence solute "freezes" in the eutectic structure leading to positive macrosegregation in the first solidified nodes. This phenomenon is better known as inverse segregation. As the transport continues in the same direction, solute is progressively depleted in the remaining liquid, causing negative macrosegregation at nodes located between 2 cm and 7 cm from the cold wall. [Figure 5.16](#) shows only the



(a) Solidification shrinkage effect: grey curves correspond to a pure diffusion in a metal monodomain case, green curves consider the latter case but with level set (metal and air subdomains) while blue curves correspond to a shrinkage-driven flow case. All cases are solved without macrosegregation.



(b) Macrosegregation effect: blue curves represent the same simulation corresponding to the shrinkage-driven flow without macrosegregation, while the red curves correspond to a simulation of shrinkage-driven flow with macrosegregation.

Fig. 5.15 – Cooling curves at different fixed positions from 0 to 10 cm (initial metal length) and from 10 cm to 14 cm (initial air length) where we show (a) the effect of solidification shrinkage on temperature history without any macrosegregation then we show (b) the effect of macrosegregation on temperature in the presence of solidification shrinkage.

5.6. 1D application: solidification with inverse segregation

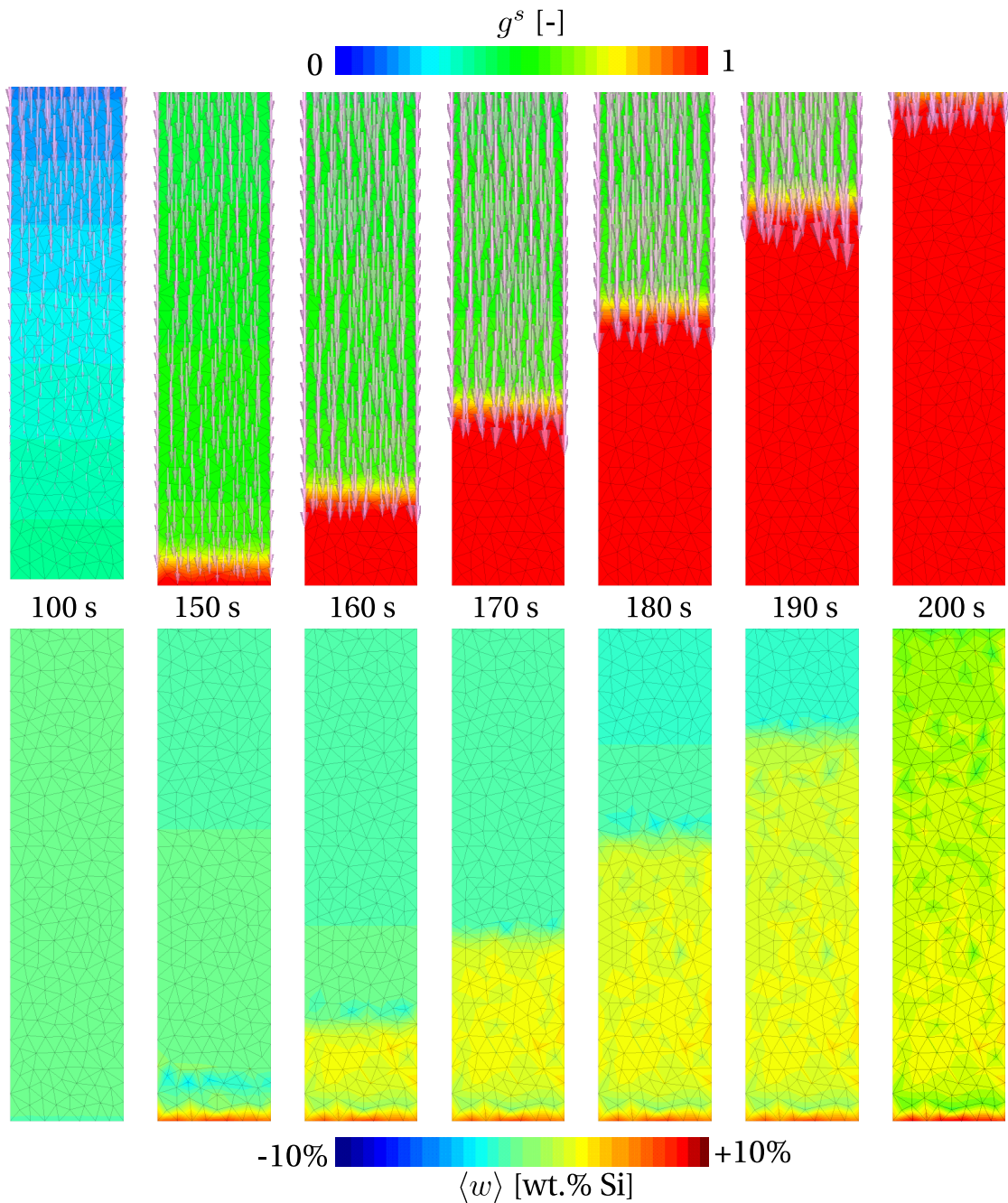


Fig. 5.16 – Zoom on the lower part, approximately 1.5 cm of the alloy close to the cooling boundary condition. The upper row of figures show the evolution of volume solid fraction, when eutectic transformation takes place. The vectors represent the direction of the average velocity field, with a length proportional to the magnitude. The lower row of figures show for the same time increments, the solute redistribution, clearly changing behind the eutectic front.

Chapter 5. Macrosegregation with solidification shrinkage

first 1.5 cm of the solidifying sample, therefore a complete segregation profile is plotted along the sample length in [fig. 5.17a](#), showing thus the negative macrosegregation as previously explained. However, from 7 cm to the metal-air interface, the average composition rises as clearly shown in [fig. 5.17a](#). This looks more like a numerical instability than a physical rise in concentration. Bearing in mind that a reduced solute diffusion coefficient is imposed in the air subdomain $1.5 \times 10^{-12} \text{ m}^2 \text{ s}^{-1}$ compared to $1.5 \times 10^{-9} \text{ m}^2 \text{ s}^{-1}$ in the metal, we investigate into this instability by proposing two test cases: first, we try to limit the solute advection in the transition zone where flow instabilities may form as seen previously in the segregation-free sample but keeping equal solute diffusion coefficients in both domains to $1.5 \times 10^{-9} \text{ m}^2 \text{ s}^{-1}$, while for the second test case, we combine both low solute diffusion and low solute advection. The average composition results of these two test cases are respectively plotted in [fig. 5.17b](#) and [fig. 5.17c](#). These results (second plot in [fig. 5.17](#)) clearly show that just by reducing solute advection in the mixing zone reduce the amplitude of the composition instability. In contrast, changing solute diffusion properties for the air coupled with reduced solute advection (third plot in [fig. 5.17](#)) offers no further stability in the segregation profile, which should normally stay below the nominal value near the interface.

5.6. 1D application: solidification with inverse segregation

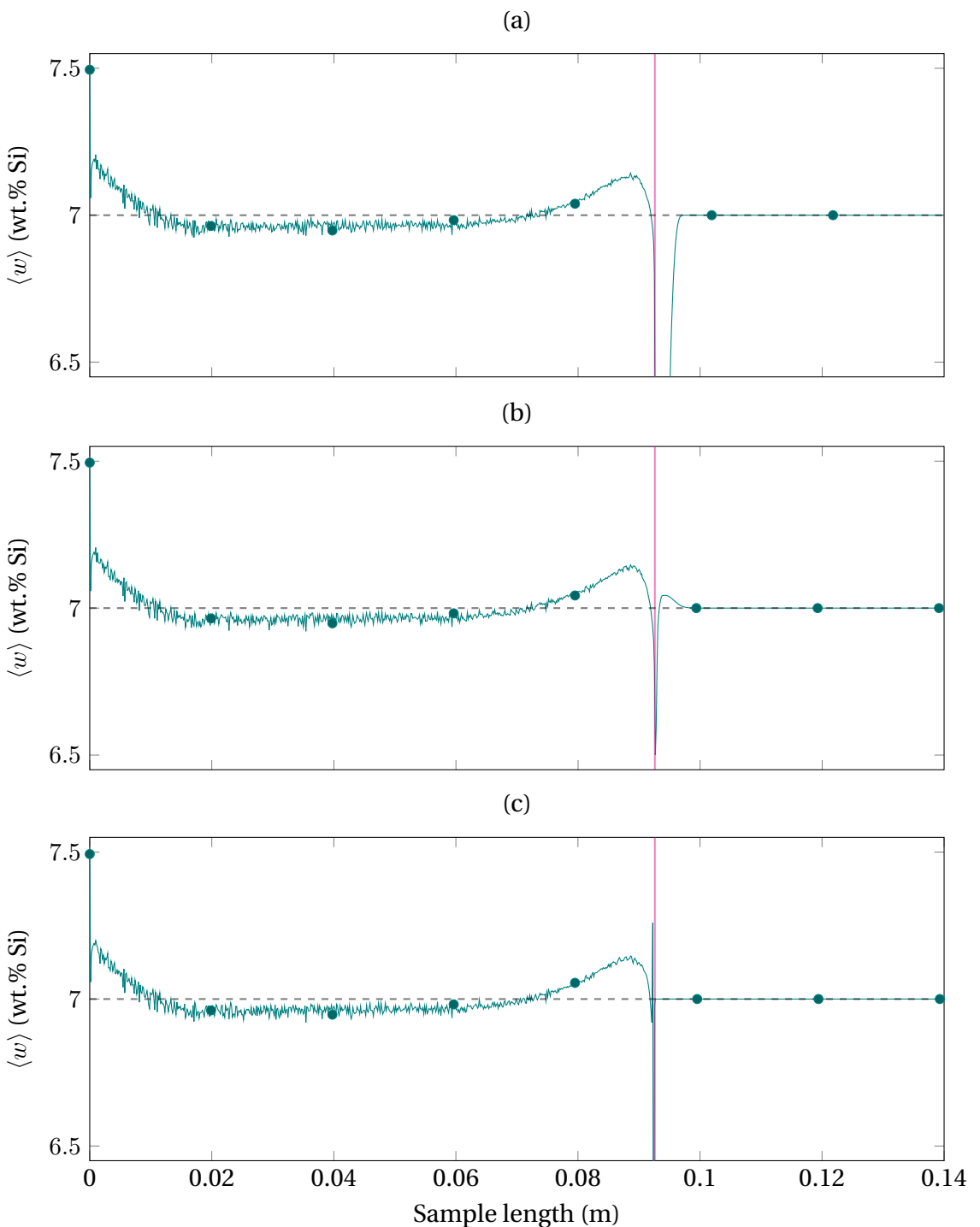


Fig. 5.17 – Plot of the average composition as function of length, along a vertical line passing through the centre of the sample at 1000 s, with (a) low solute solute diffusion in the air but unmodified solute advection (minimum composition reaches 2.2 wt.% Si but not shown), (b) reduced solute advection in the level set transition zone or (c) a combination of the previous techniques. The solid magenta line shows the position of the interface after solidification while the black dashed line shows the nominal average composition of the alloy.

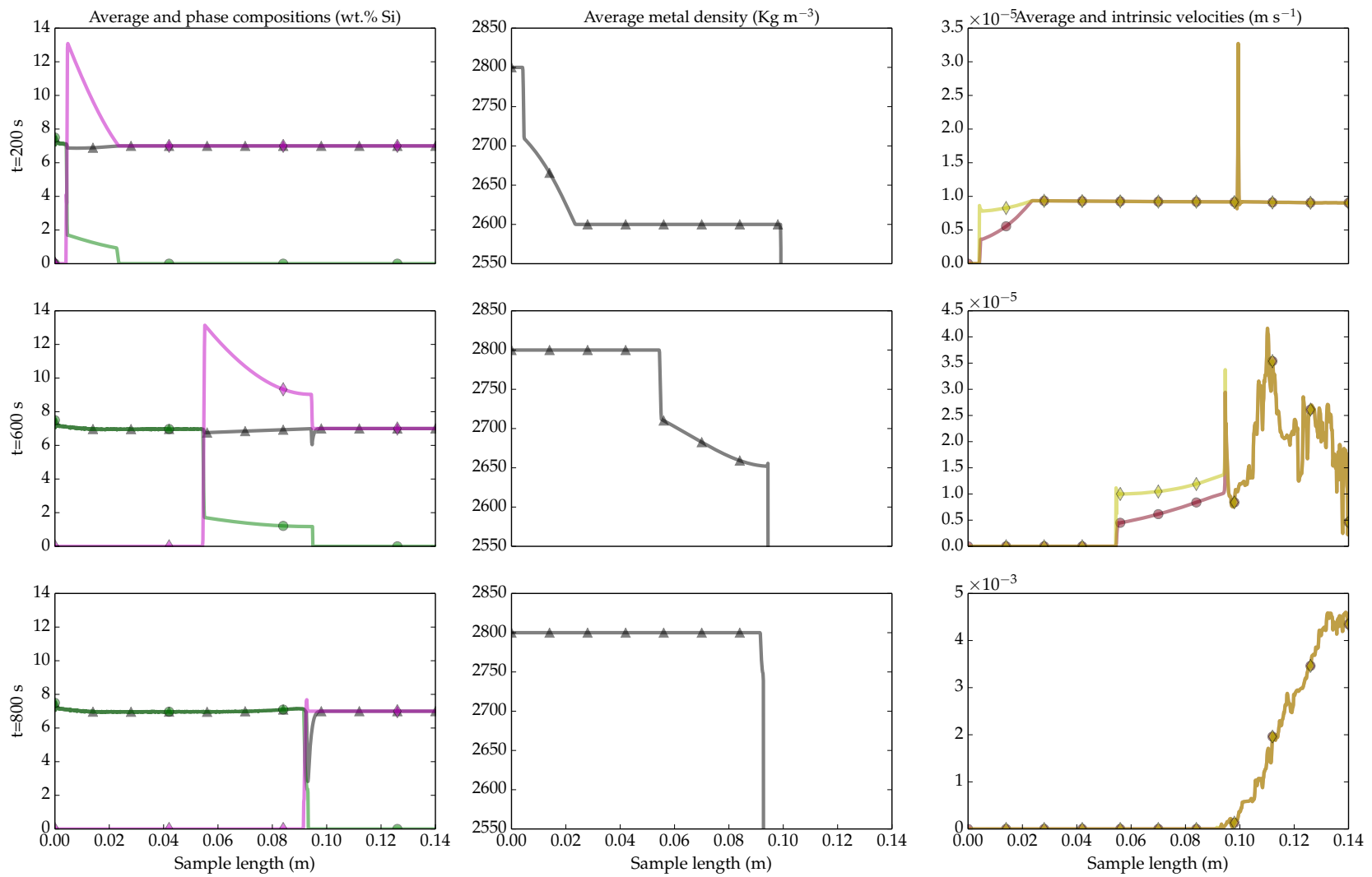


Fig. 5.18 – Group of plots where each row is a given time increment ($t=200\text{ s}$, $t=600\text{ s}$ and $t=800\text{ s}$) of the 1D solidification shrinkage simulation with macrosegregation, while each column one or more physical quantities are plotted along a vertical line passing through the centre of the sample. Plots are titled with the corresponding plotted quantities.

5.6. 1D application: solidification with inverse segregation

The plots in [fig. 5.18](#) give important information on the segregation shown in [fig. 5.16](#).
CONTINUE COMMENTING ON [fig. 5.18](#).

Solute mass conservation

Show solute mass conservation with equal or low solute diffusion in air

5.7 2D application: controlled solidification benchmark

In this application, we aim at predicting macrosegregation produced by liquid convection, in the presence of solidification shrinkage. A molten alloy is put in a rectangular crucible with controlled cooling flux on one or two sides to the crucible. The importance of the experiment lies in the thermal convection forces arising from temperature gradients, but also solutal buoyancy forces arising from liquid concentration gradients. The final macrosegregation pattern strongly depends on density variations caused by each chemical species, but also on the experimental conditions like the lateral thermal gradients as well the cooling rate, as shown in [fig. 5.19](#). Hebditch and Hunt [1974] suggested one of the first experiments working on Sn-Zn and Sn-Pb alloys. More recently, an experimental benchmark was performed by Hachani et al. [2012] to obtain more accurate composition results with various Sn-Pb and Pb-Sn alloys. In the current section, we are interested in the latter experiment, especially in the prediction of the metal's shrunk surface together with the final macrosegregation.

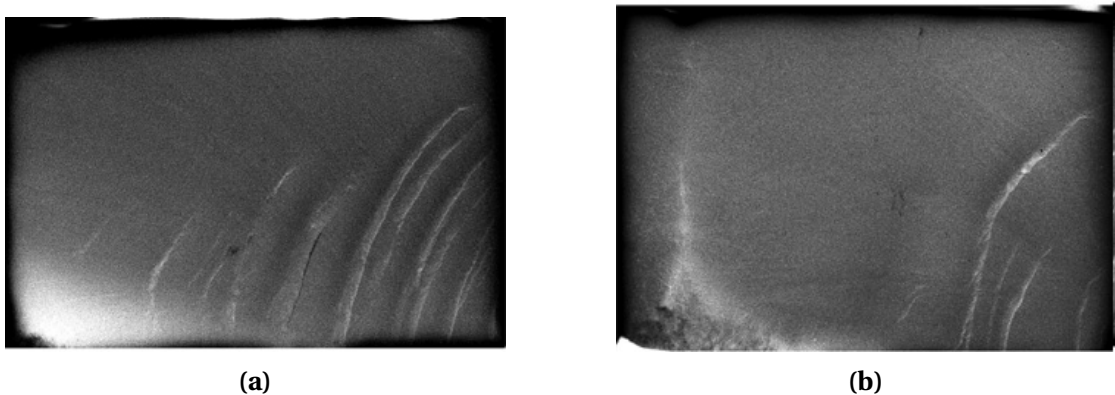


Fig. 5.19 – Final macrosegregation patterns obtained by solidifying a Sn-3 wt.% Pb alloy at (a) 0.02 K s^{-1} and (b) 0.04 K s^{-1} . The different cooling rates result in different lead segregation patterns, with a greater number of channel segregates in the latter. The X-rays show also a visible sign of volume shrinkage at the top of each ingot [Hachani et al. 2012].

5.7.1 Boundary condition effect

First, we want to understand the consequence of removing the no-slip boundary condition at the metal-air interface and compare the effect on macrosegregation. For computations without level set, as previously done in chapter 4 for the *Tsolver*'s validation in convection-diffusion regimes, a no-slip condition was applied for all domain boundaries including the interface. However, this is not readily implemented with the level set method which considers the local interface velocity for its transport. In

figs. 5.20 and 5.21, we compare at 2800 s and 7000 s the differences between a no-slip condition on the top boundary and a free-slip tangential condition, assuming zero normal velocity.

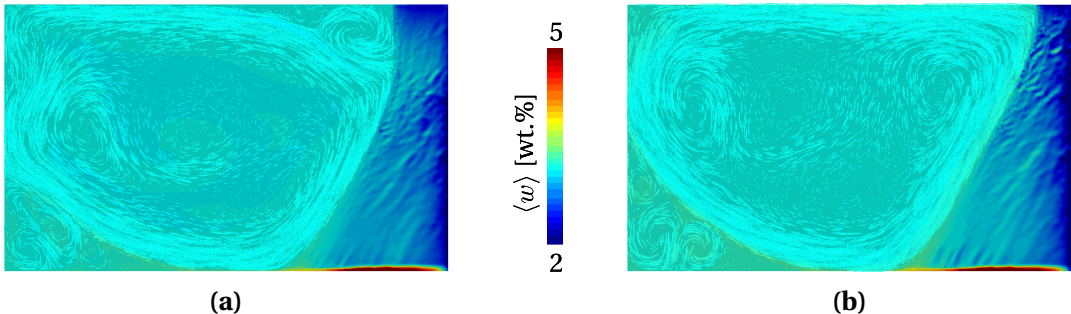


Fig. 5.20 – Comparison of two solidification with macrosegregation cases assuming (a) a no-slip condition on the upper boundary or (b) a tangential free-slip condition. The snapshots are taken at 2800 s.

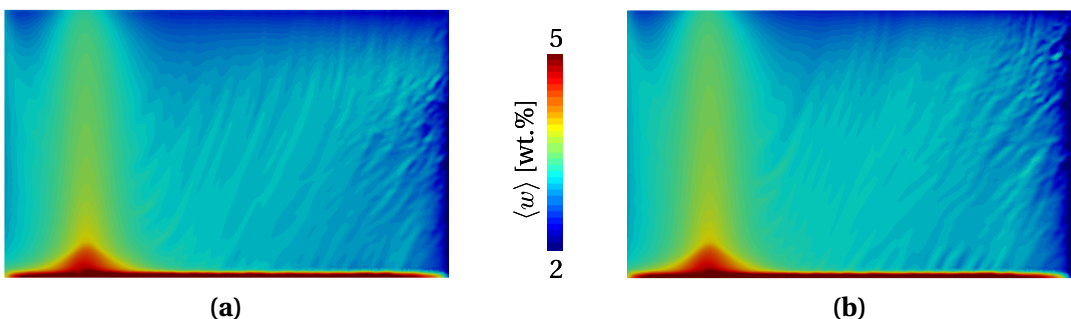


Fig. 5.21 – Comparison of two solidification with macrosegregation cases assuming (a) a no-slip condition on the upper boundary or (b) a tangential free-slip condition. The snapshots are taken at 7000 s.

In fig. 5.20, solidification is still at an early stage, at 2800 s. The main difference between fig. 5.20a and fig. 5.20b is the flow pattern near the top interface. The no-slip wall acts a brake for the vicinity flow, deviating it downwards and allow a quicker solidification rate for the right upper part of the metal. The flow near the slip wall in fig. 5.20b is not damped and therefore delays solidification of the upper corner where it impinges. The different flow pattern creates a more pronounced negative segregation in the upper right corner of fig. 5.20a, compared to the same location in fig. 5.20b. Later when solidification is complete at 7000 s (fig. 5.21), the overall macrosegregation is more visible: expect for the previously mentioned difference in the corner segregation, no big differences are observed. This means that when using the level set method, allowing the velocity to have non-zero values near the interface should not drastically change the predicted flow pattern and the subsequent macrosegregation.

5.7.2 Computational configuration

Mesh and adaptive remeshing

The case considers a 2D geometry having equivalent dimensions to the 3D case performed earlier (sample of 10 cm in length and 6 cm in height). To accommodate the air subdomain, an extra 2 cm are added to sample's height, which finally reaches 8 cm, the interface is thus kept at an elevation of 6 cm. The initial mesh consists of three different mesh sizes: isotropic meshes in the air and the metal, having respectively a uniform size of 2 mm and 1 mm. Regarding the interface, an anisotropic mesh adapts to the metal-air surface with a mesh size of 0.1 mm in the normal direction to the interface. The thickness of the anisotropic mesh spans 0.5 mm from each side of the interface.

To adapt the mesh, we use the *Remesh4* adaptive technique to maintain accurate predictions for velocity and interface transport. However as solidification proceeds, we also need to keep a relatively small mesh size in regions with noticeable composition gradients. Although this is possible with the *Remesh4* technique, it is more difficult to maintain a fine mesh size throughout the metal, especially in areas where solidification is almost complete and the velocity field has a low magnitude. The consequence is a loss of information when coarser elements are obtained by remeshing.

To avoid such unwanted effects, we use another uniform isotropic grid, named *grid B*, having a constant mesh size of 0.3 mm, that is three times smaller than the interface elements in the original mesh (named *grid A*). The strategy consists of scanning the liquid fraction of each node in *grid A*, if its value is located between 30% and 70%, then we consider that is a region of interest, since the flow velocity is still not zero and a relatively fine mesh is locally obtained. We consequently transport the average composition field exclusively for these nodes from *grid A* to *grid B*, keeping for all other nodes their respective average composition values. It should be noted that this transport is only one-way, hence no information feedback from *grid B* to *grid A*.

Initial and boundary conditions

The air initial temperature is the same as the initial liquid. This is only a hypothesis to prevent steep temperature gradients at the interface, which may lead to surface solidification. The initial and boundary thermal conditions used to cool down the metal are defined in chapter 4, given by the experimental data of [Hachani et al. \[2012\]](#). For the mechanical properties, the top wall allows free inflow/outflow of the air in all directions at an imposed atmospheric pressure. This allows the air to follow any volume changes in the metal upon solidifying and shrinking.

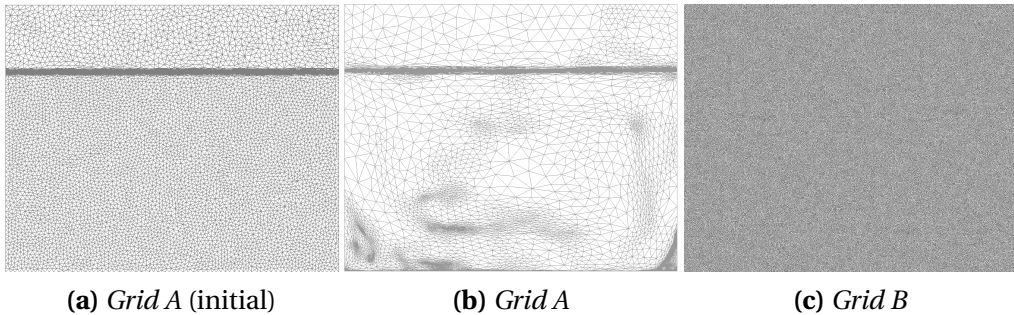


Fig. 5.22 – Snapshots of (a) the initial adaptive anisotropic *grid A* then (b) the same grid but at a given time increment with (c) the corresponding fixed isotropic *grid B* at the same time increment.

The side walls adjacent to the heat exchangers are given a free tangential slip boundary condition but with a zero normal velocity, which lets the transported level set function move vertically without being attached to the sides. Finally, a no-slip condition applies to the bottom wall.

5.7.3 Results

The results are recorded at two intermediate solidification stages, at 3050 s and 3550 s, knowing that solidification onset is around 1920 s. First, we look to the results in [fig. 5.23](#). The original average composition field obtained by *grid A*, shown in [fig. 5.23a](#), is almost free of composition gradients except for one segregated channel rising from the bottom by the action of thermal convection. On the other hand, the average composition transport from the adaptive grid to the fixed one, allows recording macrosegregation onto the latter at nodes where the solid exceeds 0.7 in volume fraction, depicted by the yellow region in [fig. 5.23c](#). This is why we observe in [fig. 5.23b](#) a number of channel segregates which are slightly below nominal composition but still richer in lead species with respect to the surrounding solid. The solid fraction distribution is shown in [fig. 5.23d](#), along with the flow pattern. Local vortices are observed in the metal, probably due to considering only a 2D geometry instead of the complete 3D, and this alters the computation stability by ignoring the boundary layers in the sample thickness, obtained otherwise in 3D. Nevertheless, the overall flow is driven by a thermosolutal driving force, with a compatible flow in the air side. We can observe how the solid fraction is modified in the segregated channel, as a result of macrosegregation. At this stage of solidification, the interface movement is still difficult to see, but 500 s later it becomes more visible.

We are now at 3550 s, and the decreasing left heat exchanger temperature has just gone below the local liquidus, triggering solidification from the left side. The average

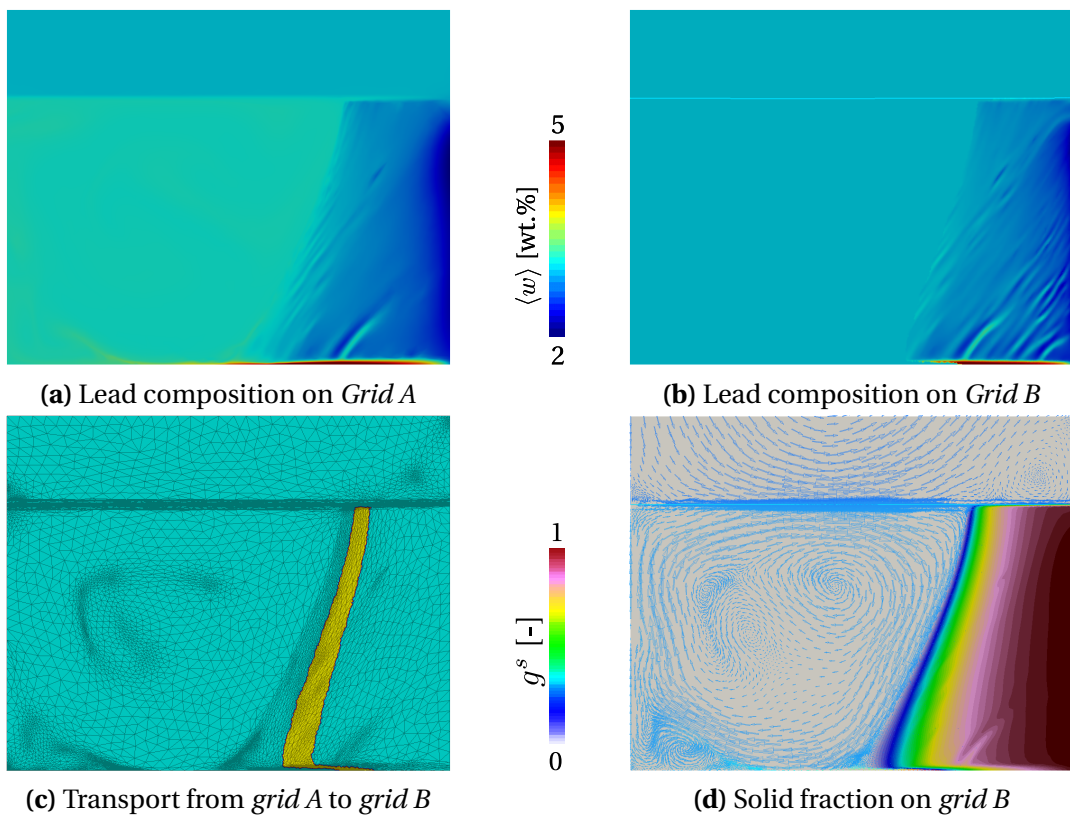


Fig. 5.23 – Snapshots at 3050 s of the average composition field shown on (a) *grid A* where the mesh gets coarser in fully solidified regions near the right side while and then on (b) *grid B* where the uniform fine mesh predicts a smoother composition field (line indicates the current interface level). The increased number of segregated channels on the right side of the metal is obtained by the successive transport operations performed in (c) a restricted area (yellow color) based on the nodal values of (d) the solid fraction field.

composition field presents noticeable differences between the adaptive *grid A* and the fixed *grid B*. The weak mesosegregation observed in [fig. 5.23a](#) are now lost in [fig. 5.24a](#), as the mesh got coarser on the metal's solidified right side. Fortunately, the macrosegregation distribution is stored in the fixed grid ([fig. 5.24b](#)) and shows more details with the advancement of solidification. The shrinkage due to phase density difference, is now clearly visible judging from interface shape, which still almost planar above the last liquid pool.

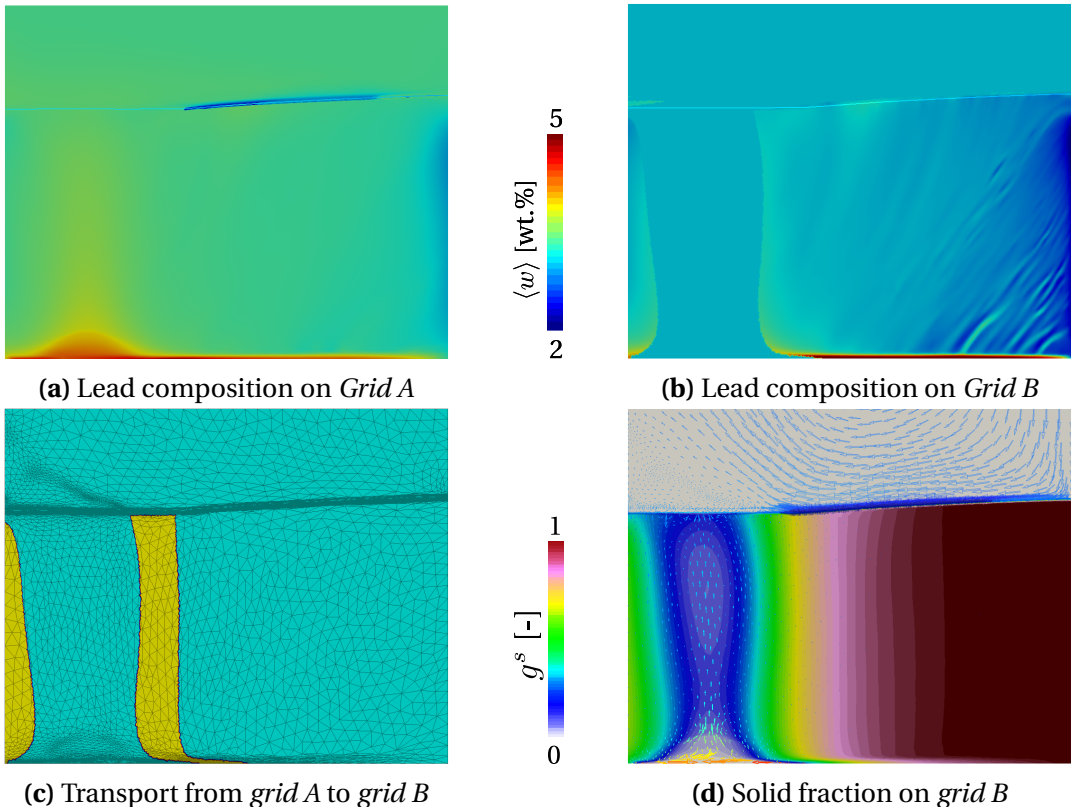


Fig. 5.24 – Snapshots at 3550 s of (a) the average composition result obtained on *grid A*, compared to (b) the composition field obtained on *grid B*, (c) theafter being transported in (c) a restricted area (yellow color) based on the nodal values of (d) the solid fraction field.

5.7. 2D application: controlled solidification benchmark

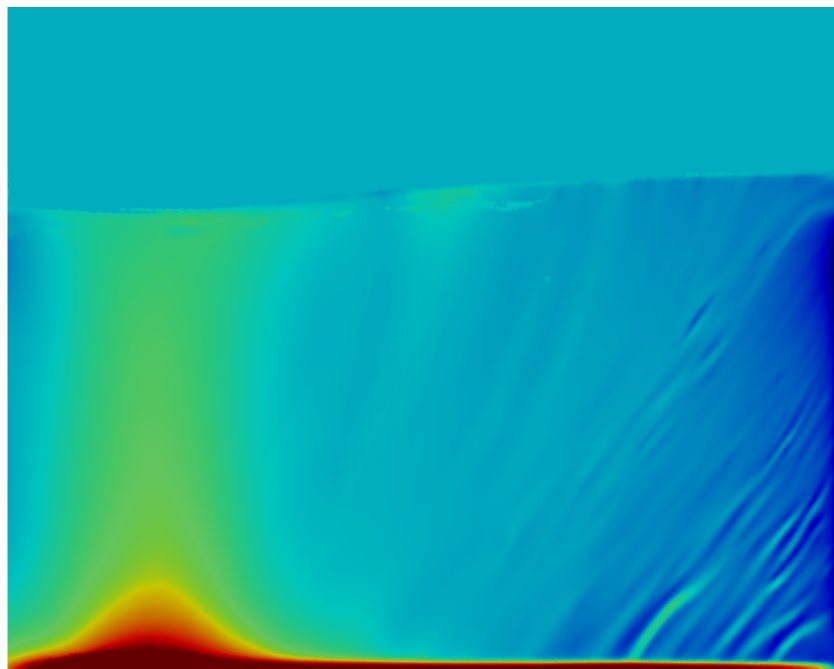


Fig. 5.25 – blabl

5.8 3D application: reduced-gravity solidification

As presented in the introductory chapter, the aim of the CCEMLCC project is to "reach a better understanding of surface defects formed during processing of steels from the liquid state" [Gandin 2014]. Among the several scientific topics being studied, the interaction between skin macrosegregation and thermomechanical deformation is investigated through chill cooling experiments. The idea is to have the molten steel in a containerless environment, which could be done by several ways: electromagnetic levitation, on-board parabolic flights or sounding rockets and finally in a real microgravity context as in the ISS. Heat is extracted from the sample by contact with a ceramic (Si_3N_4) substrate at room temperature (hence the term "chill cooling"), that collides into the alloy at a controlled speed. This contact situation generating high thermal gradients is comparable to casting processes between the molten alloy and the moulds. For ground-based experiments, EML is the exclusive technique to achieve a chill cooling experiment. However, it is technically difficult to achieve levitation without currents in the spherical sample, generated by means of electromagnetic stirring (Lorentz forces) on the one hand but also by thermal convection on the other hand. In reduced-gravity conditions, the dynamics of the phenomena behind fluid motion are less significant. The current application is therefore compared to chill cooling experiments performed in parabolic flights and sounding rockets with reduced gravitational forces ($\|g\| \in [10^{-1}; 10^{-5}] \text{ m s}^{-2}$).

5.8.1 Previous work

TEMPUS experiment on parabolic flight

The TEMPUS experiment came as a first alternative for EML experiments in which accurate thermophysical and rheological characterisation were difficult to achieve. The flight consists of several cycles of free fall, a reduced-gravity environment is hence created, allowing to use only a single RF coil to stabilise the position of the droplet, while the substrate comes into contact with the molten sample from above it. An axial pyrometer measures the sample temperature during the process. Also, a high-speed camera records the solidification process, producing frames as shown in [fig. 5.27](#). This is useful to measure the front growth speed. Each parabola cycle lasts for 50 s, offering an effective low gravity ($\|g\| \approx 10^{-1} \text{ m s}^{-2}$) for about 20 s.

TEXUS sounding rocket

TEXUS-46 is the name of the sounding rocket mission that carries the experimental setup, but for simplicity we will refer to the latter as being the TEXUS experiment. The setup is shown in [fig. 5.26](#). The main difference with respect to parabolic flight experiments, TEXUS features solidification in near-zero gravitational fields and for extended periods of time (3 minutes). We do not have an exact measurement of the gravitational field magnitude, but it is several orders less than Earth's gravity magnitude ($\|g\| \in [10^{-5}; 10^{-8}] \text{ m s}^{-2}$).

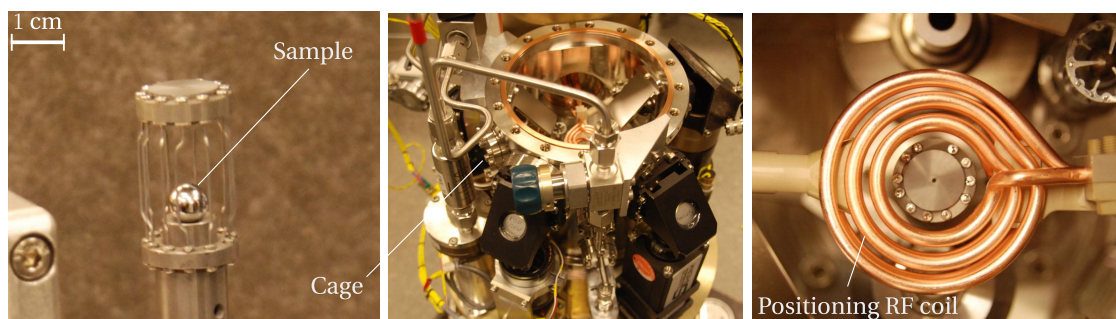


Fig. 5.26 – Three frames describing the experimental setup used to achieve reduced-gravity solidification on-board a sounding rocket flight, showing the initial alloy sample, the cage and the positiong coil. The setup is similar to the one used for TEMPUS experiments.

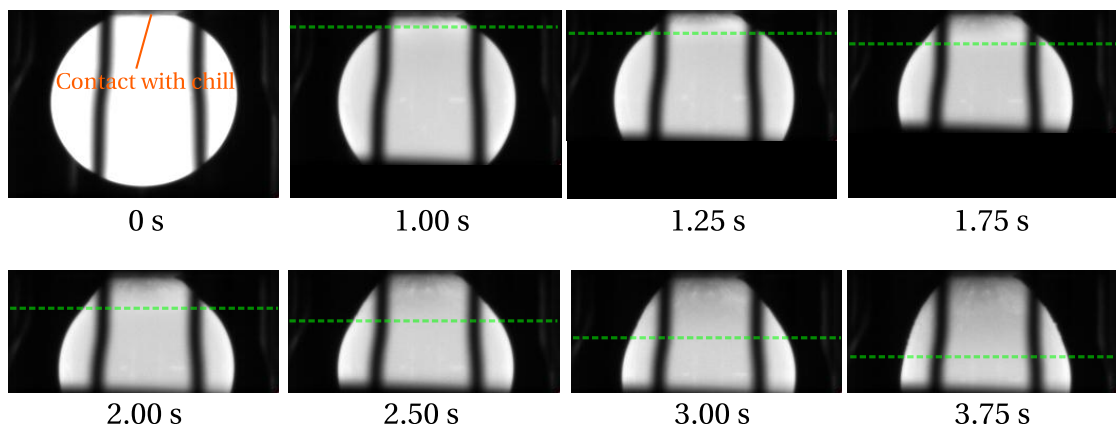


Fig. 5.27 – Image sequence given by a high speed camera on-board a TEMPUS parabolic flight, showing the solidification progress between 0 s (when contact with the chill is initiated) to 3.75 s in a Fe-0.9 wt.% C-0.2 wt.% Si steel droplet. The progress of the solidification front is marked by the green dashed line. In some frames, the droplet is partially hidden by the narrow opening of the sample holder facing the camera.

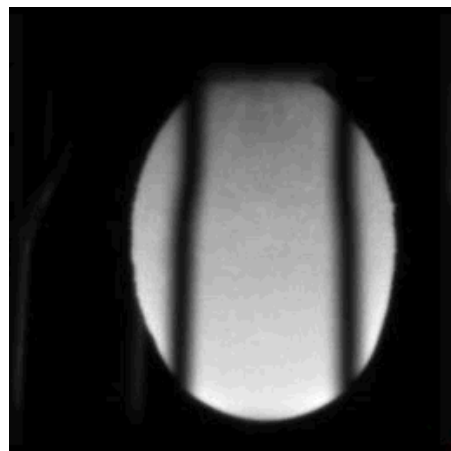


Fig. 5.28 – Camera image from the TEMPUS 2014 experiment, showing the fully solidified droplet with a deformed shape after 10 s.

Numerical contribution

A former numerical contribution was done by [Rivaux \[2011\]](#) at CEMEF, as mentioned in the first chapter. His model considered both the steel droplet and the ceramic chill in a Lagrangian formulation, i.e. each object is modelled using a separate deformable mesh. Conservation equations of mass, energy, chemical species and momentum were solved in the metal domain, while the energy conservation was the sole equation solved on the chill mesh. The mechanical problem was divided into two parts: fluid and mechanics and solid mechanics. For the first part, the momentum conservation in the liquid phase was solved using an incompressible P1/P1 SUPG-PSPG formulation of Navier-Stokes equations, i.e. without any contraction for the liquid phase neither solidification shrinkage at the solid-liquid interface. The second part, solid mechanics, was solved using P1+/P1 formulation to predict solid deformation caused by the solid's thermal contraction as well as solidification shrinkage, using an elastic-viscoplastic behaviour.

The simulation results showed that the total droplet deformation that has been observed in the experiments is not primarily due to solid deformation. The density jump between the solid and liquid phases at the solidification front is actually predominant. High speed camera images endorse this observation, where the droplet underwent a continuous spherical-to-elliptic shape change while the solidification front travelled away from the contact point. Another interesting point to comment is the computation of solidification shrinkage in the solid resolution, although this type of shrinkage does not generate stresses in the solidifying alloy, compared to thermal shrinkage for instance.

5.8.2 Computational configuration

Geometry and mesh

The simulation considers only 1/4 of the droplet-substrate-gas system, given the axial symmetry of the problem. Furthermore, the substrate is implicitly taken into account via a boundary condition, explained in the next section. This is sufficient in the current context, because we are only interested in the energy transfer from the droplet to the substrate.

The steel sample is not perfectly spherical initially as surface oscillations perturb the equilibrium shape. Such perturbations may be attributed to Lorentz forces creating by the positioning coil. The droplet hence is compared to an ellipsoid having a vertical minor axis of 5.68 mm and a horizontal major axis of 6.6 mm, as shown in [fig. 5.29](#). The bottom is a planar surface (diameter of 2 mm, where the contact is initiated). Also in [fig. 5.29](#), the alloy is immersed in a gas medium (argon), such that both subdomains form together 1/4 of a cylinder having 8 mm in radius and 8 mm in height (not fully shown in the figure).

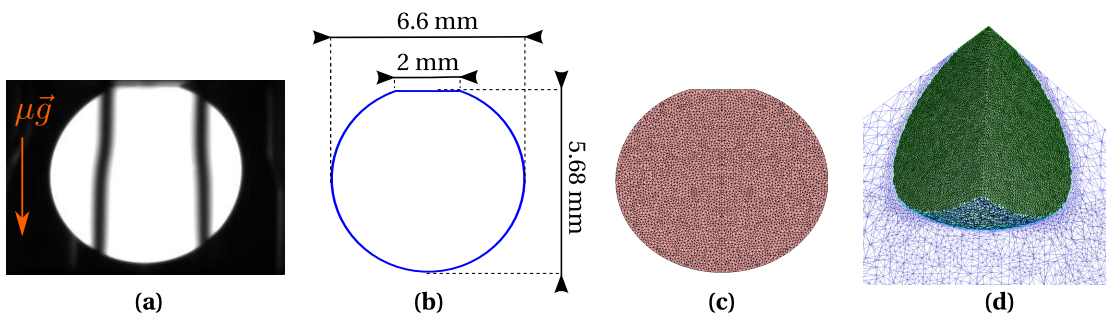


Fig. 5.29 – (a) The camera frame before the onset of solidification gives the essential information to (b) rebuild the droplet geometry then (c) a standalone 2D mesh used to obtain (d) the final immersed 3D mesh.

The mesh is then automatically adapted to the moving interface using *Remesh2*. We adopt the same remeshing strategy applied for 1D cases, whereby a fixed mesh size is imposed in the metal subdomain to limit as much as possible information diffusion due to remeshing, this is specially important for the average composition field. The corresponding parameters are given by [table 5.4](#). Remeshing is performed each second.

Initial and boundary conditions

The thermal boundary conditions are set as follows: Heat loss by radiation is experimentally avoided, therefore it is not considered in our model, hence all boundaries

Table 5.4 – Summary of the different mesh sizes used to generate an adaptive isotropic mesh, along with the level mixing thickness, ε . Refer to section 2.6.2 for the definition of each mesh parameter.

Mesh parameter	Size [m]
ε	1.5×10^{-4}
$h_n = h_\tau$	2×10^{-5}
h_M	1×10^{-4}
h_A	6×10^{-4}

are considered adiabatic, except for the metal-substrate contact area, as previously mentioned. This surface is modelled by a Fourier condition with $T_{\text{ext}}=25^\circ\text{C}$ and an effective exchange coefficient h_{ext} of $6 \times 10^4 \text{ W m}^{-2} \text{ K}^{-1}$. The h_{ext} coefficient's value has been determined by running multiple simulations with different values in the aim of predicting a front speed as closer as possible to the experimental measurements plotted in fig. 5.30, as explained in the coming sections.

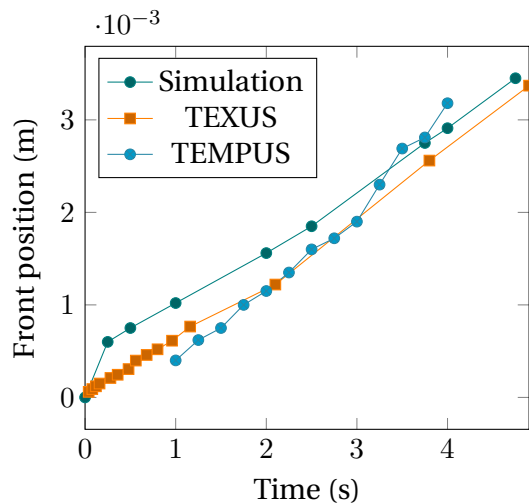


Fig. 5.30 – Position of solidification front versus time for the binary alloy simulation compared to the experimental findings of the TEXUS-46 flight in 2009 and TEMPUS 2014 measurements [Gandin 2014].

For the velocity-pressure boundary conditions, fig. 5.32 shows that a no-slip condition is imposed on the droplet-substrate surface, since this area solidifies in the first place without further fluid motion, as shows fig. 5.27. It is noted that the first solidified shell may experimentally deform under thermal contraction stresses, but we do not consider it hereafter. For the rest of the domain, we impose the normal velocity component to zero on both symmetry faces, while keeping free tangential components. The remaining boundaries, namely the top and the outer surface of the argon gas

(cylinder generatrix), have free velocity components. However, such condition may cause instability in the level set transport solver, as seen in [fig. 5.31](#). This problem has been reported by [Basset 2006], showing a limitation in the imposed boundary conditions between Navier-Stokes solver and level set transport. Therefore, we limit these instabilities by imposing a no-slip condition, thus allowing the argon to flow in the computational domain through the generatrix. The cylinder height was taken big enough to prevent any flow damping near the droplet's north pole, which may spuriously alter its final shape. The pressure condition for the argon gas is left free for all boundaries. The adopted time step is 0.01 s.

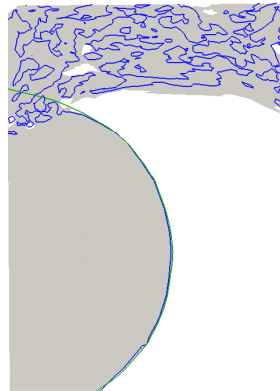


Fig. 5.31 – 2D view showing a transport instability at the top. The green line is the initial metal-gas interface, while the blue line represents the transported zero-level of the distance.

Table 5.5 – Nominal composition (wt.%) of the experimental *b1* steel and its simulation equivalent binary, ternary and quaternary alloys, respectively *b1Bin*, *b1Tern* and *b1Quat*.

Alloy	C	Si	Mn	Al	S	P
<i>b1</i>	0.105	0.268	0.636	0.0067	0.009	0.0189
<i>b1Bin</i>	0.105	-	-	-	-	-
<i>b1Tern</i>	0.105	0.268	-	-	-	-
<i>b1Quat</i>	0.105	0.268	0.636	-	-	-

Choice of alloy

Various steel grades were considered in the CCEMLCC project. Each grade was assigned to a specific experiment. We limit our study to the steel assigned for TEXUS missions, the grade is designated as "*b1*" alloy. Its nominal composition is given in [table 5.5](#). As our approach relies on thermodynamic tabulations, we show in the next section that we can take into account the multicomponent alloy to predict segregation, by considering first only one species, hence a binary Fe-C alloy, refer to as *b1Bin*

5.8. 3D application: reduced-gravity solidification

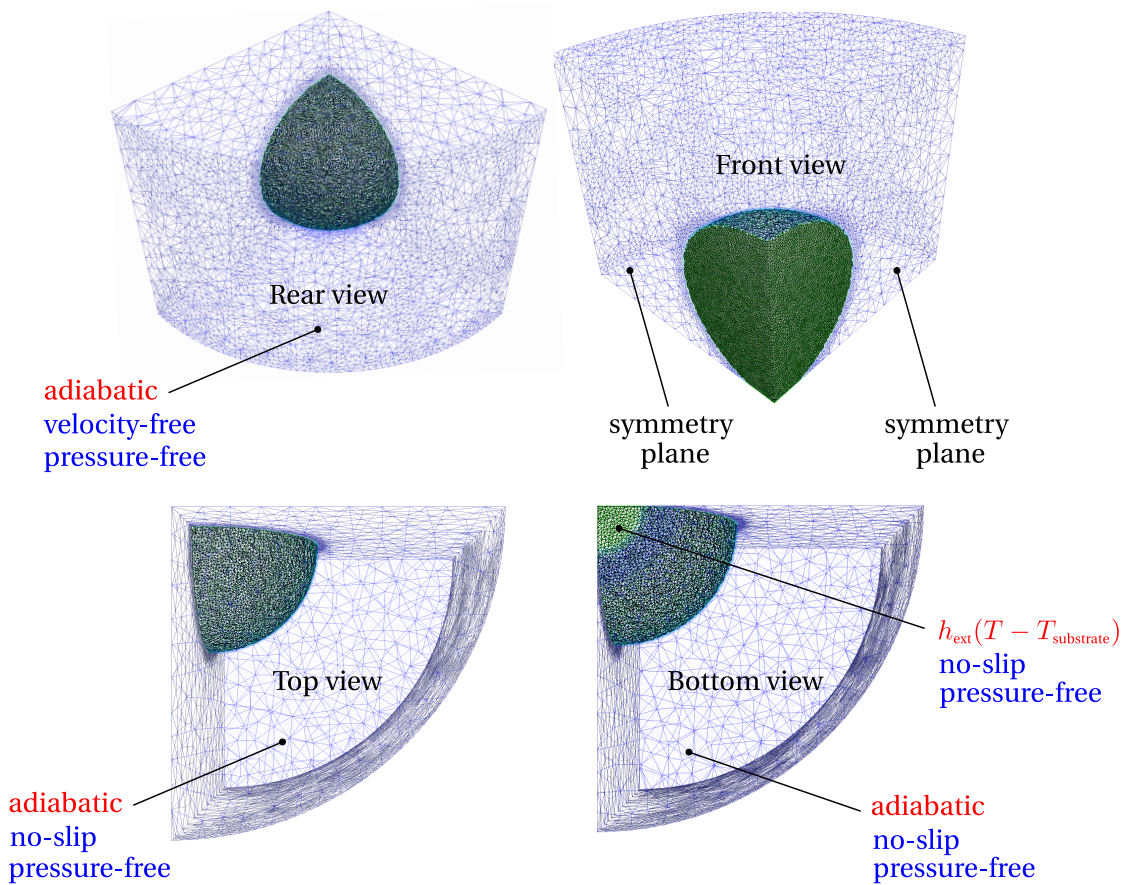


Fig. 5.32 – 3D views showing the thermal (in red) and mechanical (in blue) boundary conditions used in reduced-gravity simulations.

alloy. In a later step, we consider a ternary Fe-C-Si alloy, *b1Tern*. Finally, we consider a quaternary Fe-C-Mn-Si alloy, *b1Quat*.

By performing the same reduced-gravity simulation while varying the alloy from binary to quaternary, we can study how the varying solidification paths (as a consequence of macrosegregation) may affect the final droplet shape, as the shrinkage profile is directly related to the solid fraction and its evolution with time.

Parametric study: final shape prediction

In this subsection, we focus on obtaining a comparable finale shape of the droplet between the experiment and simulation. To do so, we vary 2 main important parameters: first, the heat transfer coefficient of the metal-substrate contact surface controls the heat extraction and hence the solidification rate. Second parameter is the magnitude of the gravitational field, which has a great influence on the fluid flow inside the molten droplet. The importance of this parametric study is two-fold:

1. in our model, the energy equation solved with the level set methodology considers only heat conduction and advection in the gas subdomain, hence no account for the heat dissipated by radiation (which is an ongoing PhD project at CEMEF). Therefore a trial-and-error strategy is necessary to determine an optimal value of h_{ext} to ensure that the solidification rate is the same as in the experiment,
2. from a hydrodynamics perspective, a containerless molten droplet levitated under reduced-gravity conditions is maintained nearly spherical under the action of surface tension forces. Other forces due to tangential surface tension gradients (Marangoni force) or Lorentz force may also exist. Although possible to implement by the CSF method, accounting numerically for surface tension adds complexity to the model by imposing a time step constraint. However, if we neglect this force, the droplet will tend to collapse if gravity acceleration is fast enough. Consequently, a parametric study helps us determine this gravity threshold, in the absence of surface tension.

A series of test simulations were launched in the aim of getting comparable results with the experiment. Several values of h_{ext} were tested in the interval $[10^2; 10^6]$, while the gravity acceleration influence was tested for values lying in the interval $[10^{-6}; 10^{-2}]$. The best match for the final shape while preserving a front propagation speed close to 0.7 mm s^{-1} , was obtained by setting simultaneously $h_{\text{ext}} = 6 \times 10^4 \text{ W m}^{-2} \text{ K}^{-1}$ and $\|g\| = 5 \times 10^{-5} \text{ m s}^{-2}$. To demonstrate the effect of varying these parameters, we present a parametric study in [table 5.6](#), where only the most relevant cases are studied with a binary alloy, Fe-0.105 wt.% C.

5.8. 3D application: reduced-gravity solidification

Table 5.6 – Summary of the parametric study for the conductive heat transfer coefficient (H) and the magnitude of the gravity vector (G , not to be confused with thermal gradient). The cases are defined by fixing each parameter to a reference value then varying the latter parameter. The reference values, $H_0=6 \times 10^4$ and $G_0=5 \times 10^{-5}$, ensure a good compromise when compared to the experimental solidification rate and final droplet shape.

Case	h_{ext} [W m ⁻² K ⁻¹]	$\ g\ $ [m s ⁻²]
H1G0	10^3	5×10^{-5}
H2G0	10^4	5×10^{-5}
H3G0	10^5	5×10^{-5}
H4G0	10^6	5×10^{-5}
H0G1	6×10^4	10^{-3}
H0G2	6×10^4	10^{-4}
H0G3	6×10^4	10^{-5}
H0G4	6×10^4	10^{-6}

We start the analysis by observing the results in [fig. 5.34](#), where the parameter h_{ext} increases from case H1G0 to H4G0, while maintaining a constant gravity acceleration at 5×10^{-5} m s⁻². In the first case, H1G0, the heat coefficient is at its lowest between the droplet and the chill. As this contact is the only way to dissipate heat from the droplet, a low heat exchange coefficient means a slow cooling. Therefore, contact area of the droplet solidifies first. As we consider a fixed solid in our model, any solidified part can no longer move or deform. As time passes, solidification is slow, such that the droplet starts collapsing at about 10 sec, undergoing a significant shape change under the gravity's action. In reality, such microgravity conditions are not sufficient to deform the droplet as seen in case H1G0. However, it should be noted that at such small gravity accelerations, surface tension forces play a central role in stabilising the sample shape, by minimising its surface energy. As we neglect it in our simulations, the droplet tends naturally in the direction of the gravity vector. We can make the same conclusion for case H2G0, while taking note of the smaller overall vertical deformation. We may also see that the solid shell base is thicker in the horizontal direction, featuring also necking around the droplet axis mid-height, showing a competition between solidification shrinkage and gravity effect. It should be noted that in both cases H1G0 and H2G0, solidification is not complete at 15 s.

More interesting results are obtained in case H3G0 where the heat coefficient is two orders of magnitude higher than that in the first case. The high solidification rate allows the mushy front to capture liquid nodes before deformation occurs by gravity. We see a global deformation which is qualitatively comparable to the experimental results: an ellipsoid form with a longer vertical axis with respect to the initial shape,

while the horizontal axis decreases compared to the original sample diameter. Finally, we observe the same deformation tendency if we compare cases H3G0 and H4G0. However, the latter shows less deformation on the sides, which is the direct result of the fast cooling rate.

In order to have a clear idea on the effect varying the cooling rate parameter on mass conservation, we plot in [fig. 5.33a](#) the mass variation versus time for all four cases. We can notice that mass variation for case H4G0 occurs between 2% and -1% near the solidification end, recording the least variations compared to other cases. On the other hand, cases H1G0 and H2G0 show an important mass loss before solidification comes to end, reaching -11%. We are particularly interested in case H3G0, which shows a good compromise between the deformation magnitude and mass loss, the latter being at -3% of mass metal.

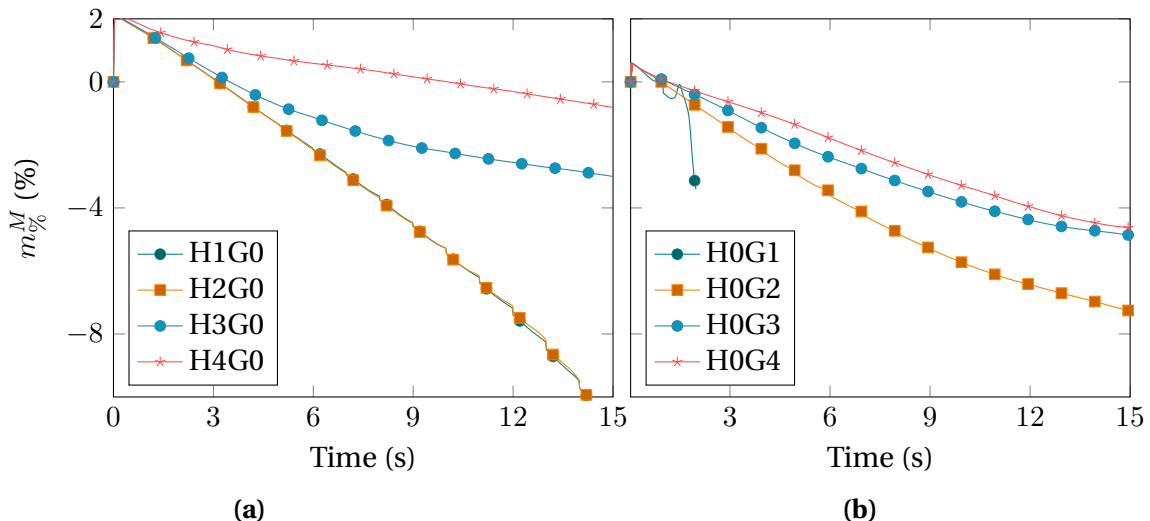


Fig. 5.33 – Mass conservation analysis for (a) cases HxG0 ($x=1,2,3,4$) and (b) cases H0Gx ($x=1,2,3,4$).

Now, we study the effect of varying the gravity parameter and its influence on the final deformation. We observe first the results for case H0G1 where gravity magnitude is about four orders less than the Earth gravity at zero altitude. While the base solidifies, the remaining part falls down deforming severely by its weight and leading to a non-converging level set transport. The last recorded time is 1.75 s. For case H0G2, the droplet is less solicited by its weight, and therefore solidifies while having a vertically elongated shape. It should be reminded that in the current global numerical model does not account for the metal's surface tension, which may clearly have a drastic influence on the final shape, especially at higher gravity magnitudes, such as for cases H0G1 and H0G2. Moving on to cases H0G3 and H0G4, the weight driving force

becomes negligible compared to the shrinkage driving force. Therefore, the sample shows significant lateral deformation, while in the central vertical plane of the droplet, the droplet has shrunk when compared to the initial profile. This is more visible in case H0G4, where the final shape is overall smaller than the initial volume, which is not the same as found in cases H3G0 and H4G0. The mass conservation analysis corresponding to the gravity magnitude variation are plotted in [fig. 5.33b](#). The plots show, as expected, better mass conservation for decreasing gravity acceleration, i.e. from case H0G1 to H0G4. We think however that surface tension would change this analysis, and non-convergence obtained in case H0G1 may be prevented.

5.8.3 Texus binary alloy

The optimal computational configuration is now known, thus we proceed to simulate the solidification of the binary alloy given previously in [table 5.5](#). The nominal composition for this alloy is Fe-0.105 wt.% C. In order to obtain accurate segregation results, a fine resolution mapping was performed from equilibrium calculations, using 20 values of composition between a minimum of 0.01 wt.% and 1 wt.%. This is equivalent for a composition step of 0.0495 wt.%, with a temperature step of 1 °C varying in the interval [20 °C;1600 °C]. The importance of choosing small steps in composition and temperature is to predict accurate solidification paths during mesosegregation (relative to the droplet scale), which is the main input of solidification shrinkage. Therefore, less accurate mappings may result in false shrinkage profile prediction, as will be shown henceforth.

Using the initial and boundary conditions defined earlier, 15 seconds of simulation give the final shrinkage profile given in [fig. 5.36](#). We notice that the predicted overall deformation of the droplet is in a good agreement with the experimental shape after solidification. This agreement is still not perfect as some key input parameters are still missing in the model, namely the real gravity acceleration on-board the parabolic flight (which should be much greater than value used in the simulation), and the correct heat flux between the sample and the substrate. It is emphasized that for higher gravity accelerations, surface tension is of central importance since it counters the gravitational force by stabilising the air-metal interface.

Three solid phases are considered for the *b1Bin* alloy: a primary BCC phase, a peritectic FCC phase and a cementite phase. The latter can be obtained by cooling the sample at low temperatures to achieve solid-state transformation. The next point to discuss is segregation and fluid flow. With the chosen gravity acceleration, the liquid metal moves in the downward direction when the ceramic substrate comes from above the droplet. As soon as solidification takes place right after the metal-substrate contact, a

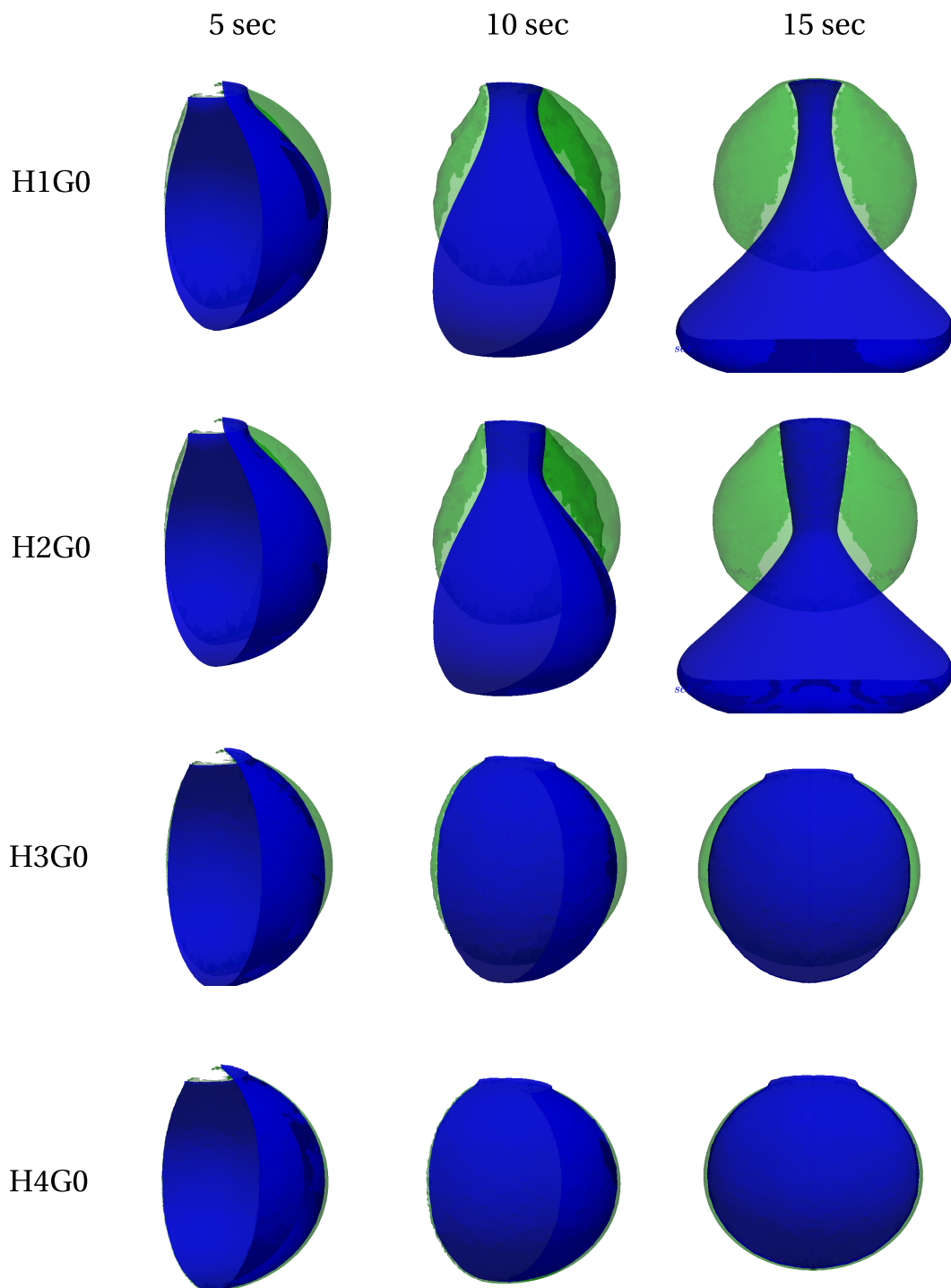


Fig. 5.34 – 3D snapshots of a droplet (only half shown for symmetry) undergoing solidification shrinkage where the heat exchange coefficient increases from H1 to H4 according to [table 5.6](#). The green surface is the initial droplet profile while the blue surface is the deforming droplet profile. The camera rotation over time allows observing deformation from different angles. The gravity vector points downwards.

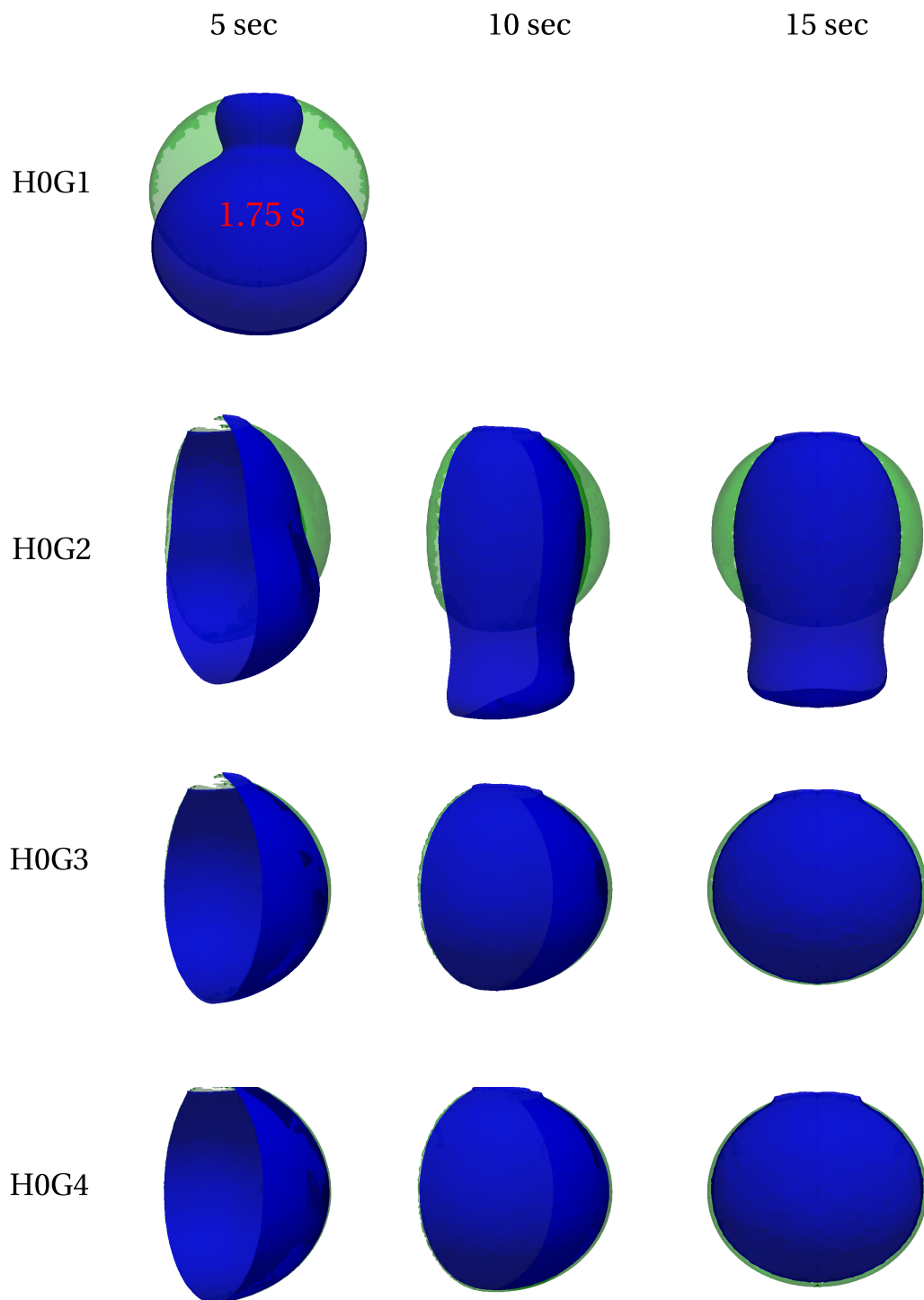


Fig. 5.35 – 3D snapshots of a droplet (only half shown for symmetry) undergoing solidification shrinkage where the magnitude of the gravitational field decreases from G1 to G4 according to **table 5.6**. The green surface is the initial droplet profile while the blue surface is the deforming droplet profile. The camera rotation over time allows observing deformation from different angles. The gravity vector points downwards.

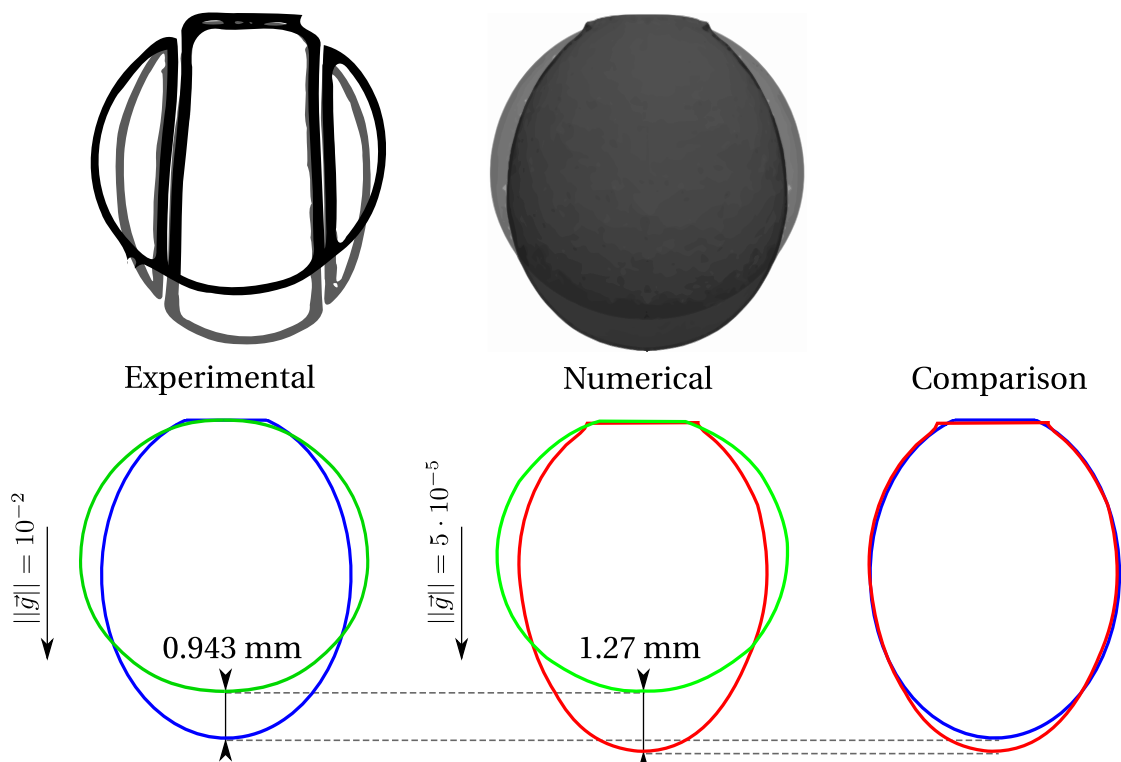


Fig. 5.36 – Comparison of experimental (blue) and numerical (red) shrinkage profiles, compared to their respective initial shapes (green). A vector image processing algorithm is used to extract the droplet outlines from the experimental images. The experimental displacement at the top of the droplet was estimated by scaling the initial numerical profile to the experimental one, and then comparing the final profiles. The direction of the gravitational fields points downwards, depicted by the arrow (note that the vector length is not scaled to its magnitude).

BCC-rich mushy zone forms near the contact surface. The abrupt phase change imposes a fast shrinkage rate, which tends to straighten the interface near the substrate, as we can observe in [fig. 5.36](#). A part of the flow thus deviates towards the solid front to compensate for the density increase, as shown in [fig. 5.37](#). This flow pattern in the sample shows distinct regions at 0.25 s and 1 s in the previous figure: upward flow driven by solidification shrinkage contributes to a slight enrichment by inverse segregation, while a downward flow driven by gravity redistributes species in the containerless melt. Upon completely solidifying, the droplet forms a rigid and fixed solid, surrounded by natural argon flow.

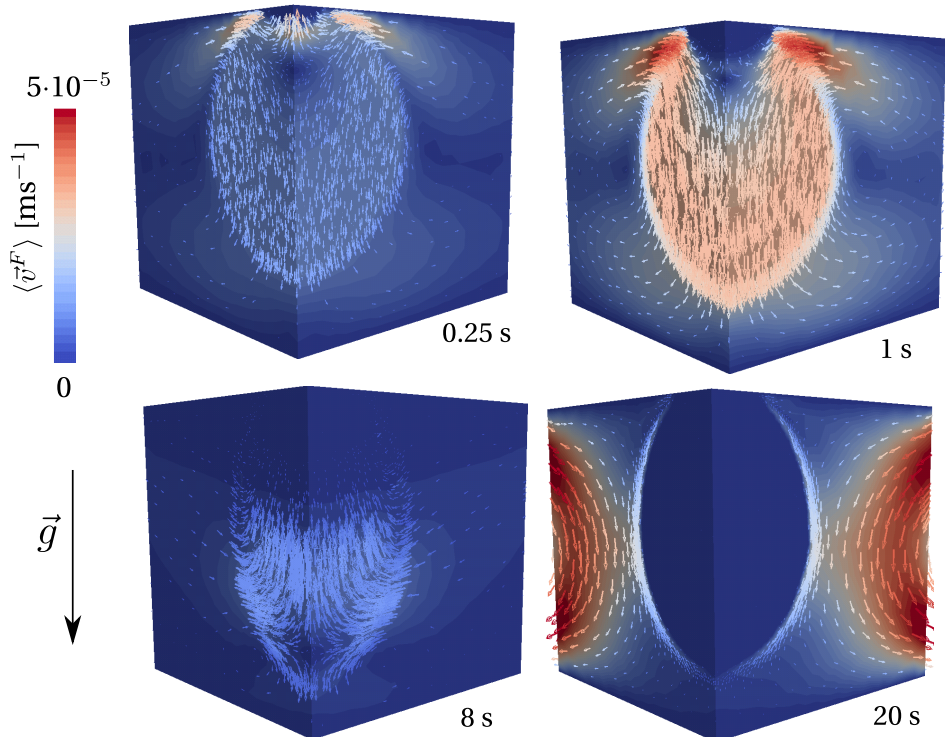


Fig. 5.37 – Flow patterns in reduced-gravity solidification with shrinkage: deviation towards the solidification front at 0.25 s and 1 s, contributing to solute transport in gravity's opposite direction. At 8 sec, the mushy zone reaches the droplet vertex marking a flow pattern change. At 20 s, the argon flows freely in the domain around the completely solidified and rigid sample. Please note that the scale of latter snapshot has a maximum magnitude of 10^{-6} m s^{-1} , not shown for illustrative simplicity.

The fluid flow is behind the reduced-gravity segregation shown at different stages in [fig. 5.38](#). We may call it mesosegregation, as the droplet is small and considered as a laboratory-scale sample. As earlier mentioned, a restricted region of positive segregation settles at the contact area with the substrate, from the first second after the contact. Later, between 2 s and 8 s, the solid front advances in the melt, creating a noticeable negatively segregated area, about 4% less than the nominal composition,

Chapter 5. Macrosegregation with solidification shrinkage

just below the positive segregation zone. Normally, we would expect that the composition decreases gradually once the solid front advances in time, as confirm the 1D segregation profiles in [fig. 5.17](#). To interpret this unusual observation, we refer to the fluid flow shown earlier in [fig. 5.37](#). At 0.25 s, a velocity zero-level isovolume (i.e. depicting a volume with null velocity magnitude) forms between the two distinct regions of upward and downward flow. The strong negative divergence that settles in this area results in solute depletion in the two directions and due to the various driving forces.

However, at 1 s, the zero isovolume clearly shrinks in a matter of only 0.75 s. That is because the initial temperature gradient is the highest during the process, then it decreases gradually. Since a higher temperature gradient produces a greater cooling flux according to the Fourier model, solidification is faster in the beginning and the volume shrinkage is fast, hence the shrinkage flow coexists with the gravity flow. As the transformation progresses, shrinkage flow becomes insignificant compared to the latter, therefore the negative segregation intensity decreases gradually from 2.2 mm to 4.3 mm from the chill, corresponding to the first seconds of contact ($t < 8$ s). This result is also shown in [fig. 5.39](#) where we plot the relative segregation profile along the vertical rotation axis of the droplet. At 8 s, [fig. 5.37](#) shows the zero-velocity isovolume moved down the vertical revolution axis by following the solidification front, then vanishing at about 10 s. It means that from this point in time, the flow is so dissipated by the mushy zone's low permeability, hence the low-magnitude shrinkage flow dominates again. We may correlate this flow pattern once again to the segregation profile in [fig. 5.39](#): As of 4.3 mm and down to the tip of the deformed sample, we observe a steady rise in solute content caused by the shrinkage-dominated flow between dendrites compensating for density differences. This rise in solute content is however not strictly correct, says the species mass conservation study, shown in FIG.

In [fig. 5.39](#), the final phase distribution along the vertical revolution axis is plotted. The plots show that in the upper part of the droplet close to the chill, a eutectoid product (we may not speak of eutectoid microstructure as the current approach is only macroscopic, without information on the smaller scale) that results from the hypoeutectoid composition, consisting of 98% of α -BCC phase together and 2% of CEM between 0 and 2.9 mm away from the substrate. Beyond this point, the austenitic γ -FCC phase is gradually replaced by α -BCC, which represents the proeutectoid α phase, taking place before temperature reaches the eutectoid isotherm at 727 °C.

A better global visualisation of the transformation is given in [fig. 5.40](#), at different time stages. Each column depicts a definite time with temperature and phase distribution.

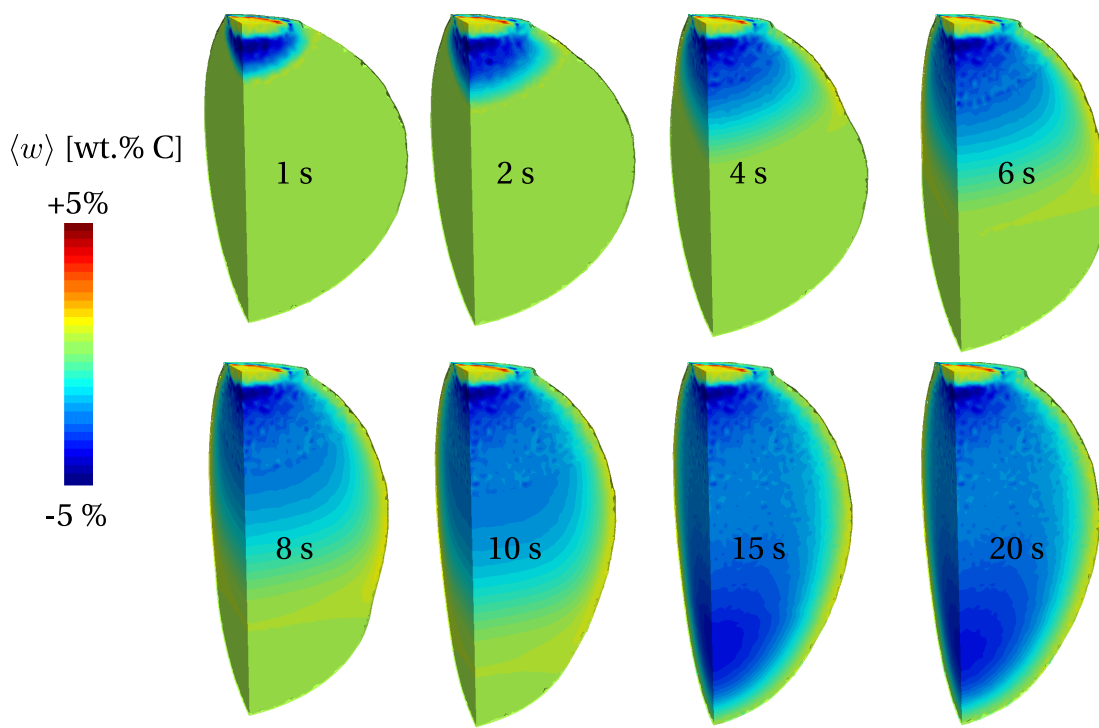


Fig. 5.38 – Evolution of the average composition with solidification time, showing evidence of mesosegregation and shape deformation between 0 s and 20 s. (check animation in the PDF file).

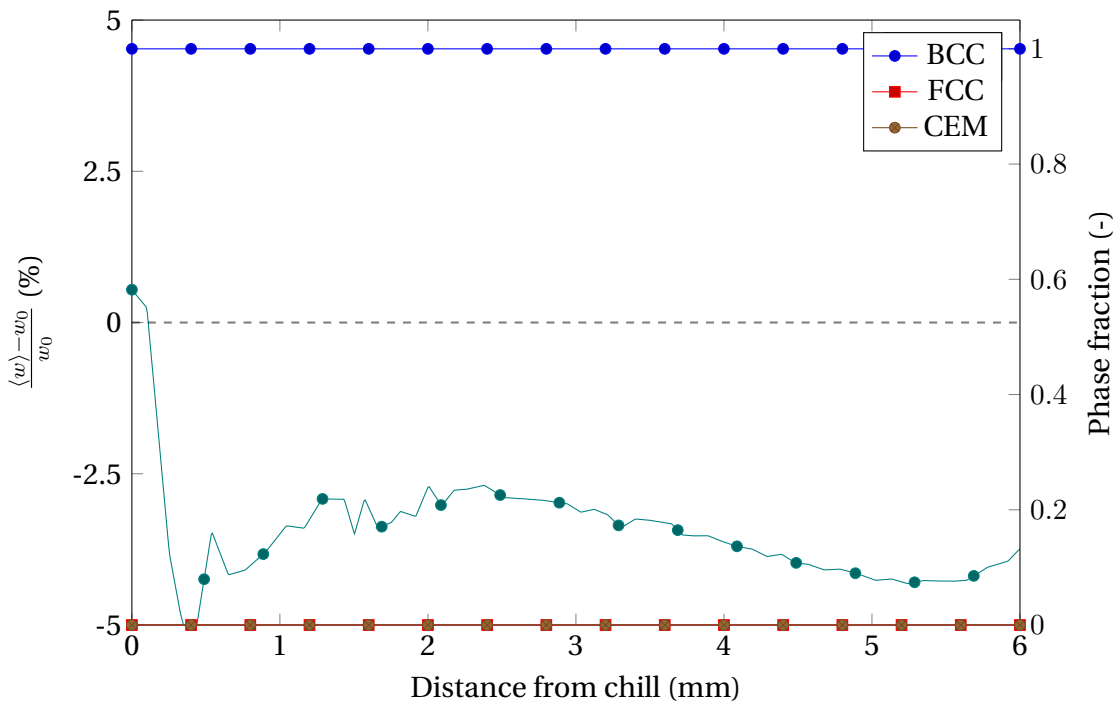


Fig. 5.39 – Segregation profile in percent with respect to the nominal composition, along the vertical revolution axis of the solidified sample.

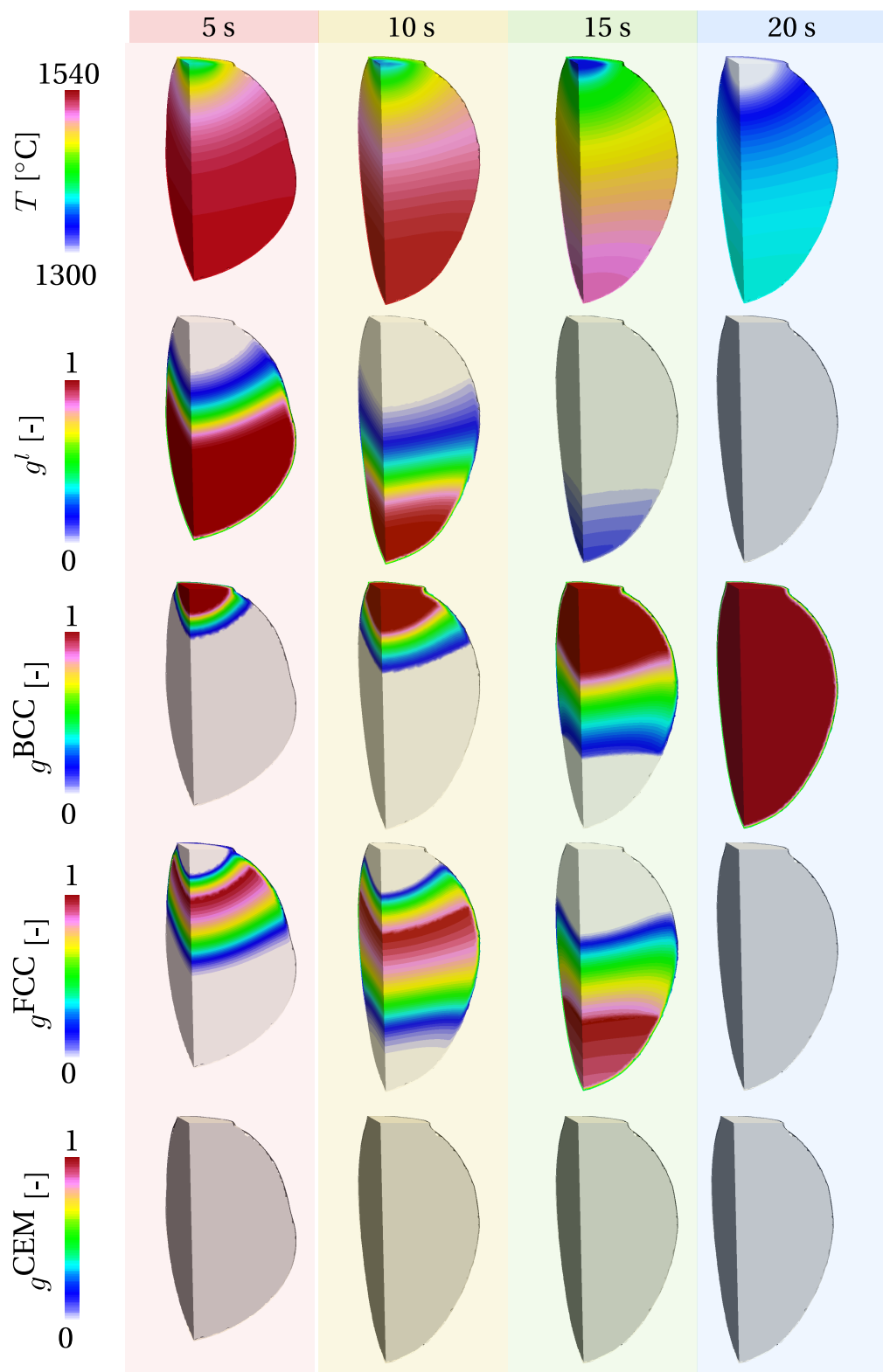


Fig. 5.40 – Solidification progress at 5, 10, 15 and 20 s showing the effect of segregation on the transformation paths, from liquid to solid and solid-state.

5.8.4 Texus ternary and quaternary alloys

In this section, the aim is to predict mesosegregation in reduced-gravity solidification of the *b1* alloy, the latter being considered as a ternary and then as a quaternary alloy (cf. [table 5.5](#)). We want to show that, on the one hand our model handles multicomponent alloys (based on equilibrium equilibrium conditions), while on the other hand, how transformation paths vary by adding additional components, thus changing the shrinkage kinetics, hence the final sample shape. The first visible sign of different paths during solidification is given in [fig. 5.41](#). We can see that upon adding additional chemical species while applying the same cooling conditions, a different liquid fraction remains after 15 s, showing evidence of slower solidification as we go from binary to quaternary. With multicomponent alloys like *b1Tern* and *b1Quat*, an additional solid phase may appear, that is the M_7C_3 carbide. Slower cooling rates result in more elongated droplet shapes due to weight force, whereas shrinkage forces tend to counter this effect. Therefore the final predicted shape is different, as shown earlier in the parametric study.

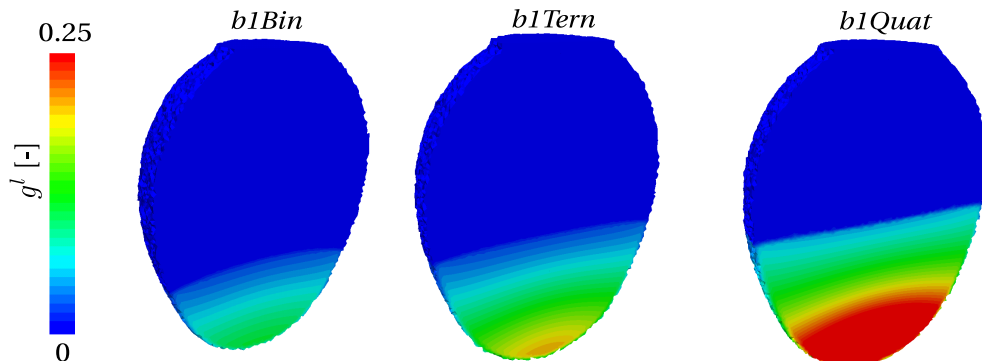


Fig. 5.41 – Snapshots showing the remaining volume fraction of liquid at 15 s in each sample of the binary, ternary and quaternary *b1* alloy.

In [fig. 5.42](#), we focus on the final droplet profile caused by varying the number of solute elements. We clearly notice that the multicomponent solidification results in an elongated shape. All cases were obtained using the optimal simulation parameters determined previously by the parametric study, i.e. an thermal exchange coefficient, h_{ext} , of $6 \times 10^4 \text{ W m}^{-2} \text{ K}^{-1}$ and a gravitational acceleration, $\|g\|$, of $5 \times 10^{-5} \text{ m s}^{-2}$. The clear difference in solidification paths requires to do the same parametric study to get better simulation-vs-experiment prediction. However, as we have shown earlier the effect of varying these parameters on the final profile, we do not perform parametric studies for *b1Tern* and *b1Quat* alloys.

The vertical elongation obtained by the *b1Tern* sample is almost the double of the

b1Bin result. Moreover, the final ternary and quaternary profiles are almost overlapping, indicating that the prediction accuracy is very close for these alloys. This reveals the importance of simulating solidification processes with real alloy compositions instead of binary simplifications where the transformation path is not complex as a result of the smaller number of phases forming at equilibrium.

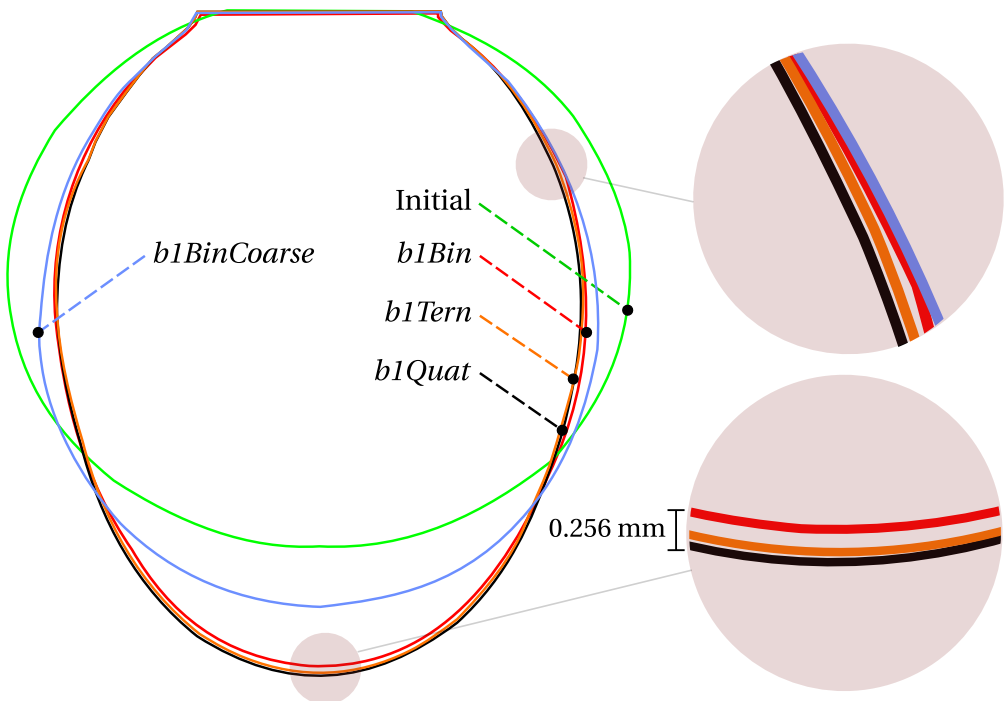


Fig. 5.42 – Comparison of final droplet profiles obtained by solidifying *b1Bin*, *b1Tern* and *b1Quat* samples, with respect to the initial profile. The *b1BinCoarse* sample is obtained using coarser composition steps.

Nevertheless, it should be mentioned that the mapping resolution plays an important role in the accuracy of thermodynamic conversions. Therefore, tabulations size easily increases with the increasing number of solute elements, because of the greater number of temperature-composition combinations to scan while computing equilibrium. To test the effect of changing the mapping resolution, we repeated the binary sample solidification but with a composition step of 0.0495 wt.% instead of 0.0052 wt.% used for the *b1Bin* sample, i.e. about 10 times coarser. The corresponding profile in fig. 5.42, *b1BinCoarse*, shows less vertical elongation than predicted by the finer *b1Bin* tabulation. This is clearly due to inaccurate calculation of the solidification path, revealing the importance of mappings accuracy in predicting transformation-related physics. In order to test the effect of the tabulation file size on computation time, we simulate again the quaternary solidification case but this time with a lightweight tabulation where all successive line with similar phase fractions outside the solidification range

5.8. 3D application: reduced-gravity solidification

are deleted, giving what we call *b1QuatLite*. The resulting file is three time smaller than the original tabulation file. Surprisingly, the computation time for *b1QuatLite* shows no significant acceleration compared to *b1Quat*. The file size, proportional to the number of tabulated lines, is important as it causes a search overhead each time the conversion module is called. However, [table 5.7](#) reveals that the multi-variable interpolation overhead is even more important, resulting in longer computation times. This is may be considered as a limitation of the thermodynamic mapping approach.

Table 5.7 – Information table showing the tabulations size for each alloy obtained by the same mapping resolution for temperature and composition, depending on the number of solute elements and phases. The computation time corresponds to the CPU time of a simulation running on 20 cores.

Alloy	Nb solutes	Nb phases	Tabulation lines	Size (MB)	Computation time (s)
<i>b1Bin</i>	1	4	185 010	4.37	59 461.5
<i>b1Tern</i>	2	5	220 250	10.18	62 644.4
<i>b1Quat</i>	3	5	1 101 250	66.89	85 476.7
<i>b1QuatLite</i>	3	5	326 014	20.93	84 104.8

Finally we are interested in comparing the mesosegregation levels obtained in all three solidification cases. Segregation maps for the three cases are presented in [fig. 5.43](#) on a symmetry plane section. First, we compare the carbon segregation as it is the common species among the presented alloys. The first difference is a remarkable positive mesosegregation of 3.5% at the chill contact of the *b1Tern* and *b1Quat* samples, while being less prominent for *b1Bin* which shows a relative segregation of 1.2%. As we explained earlier, this positive mesosegregation taking place at the beginning of solidification is related to the shrinkage flow (cf. [fig. 5.37](#)) created by the strong thermal gradient in the contact zone. As the thermal gradient in this zone is almost the same for all three cases at solidification onset, the higher velocity which is responsible for the noticeable positive mesosegregation in both multicomponent samples, is related to the solidification path varying with the number of species. Two regions of negative mesosegregation are observed across the samples, with various amplitudes. The first region lies just below the positive segregation contact surface. It corresponds to the solute depletion caused by an upward shrinkage flow and a downward gravity flow. With the advancement of the solidification front, the gravity flow dominates creating a radial outward negative segregation pattern where

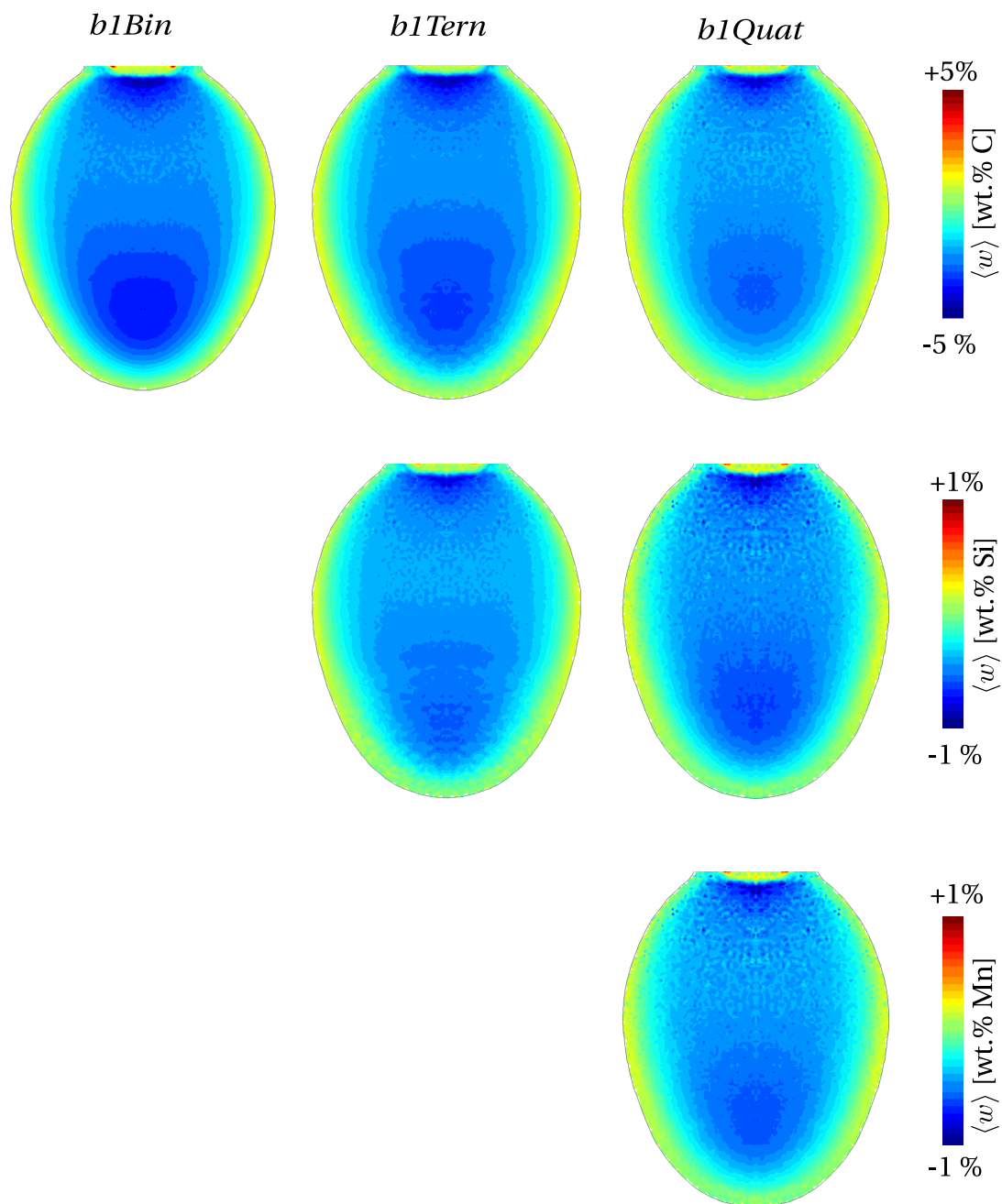


Fig. 5.43 – Segregation maps relative to each alloy, showing positive and negative mesosegregations of each chemical species for *b1Bin*, *b1Tern* and *b1Quat* samples.

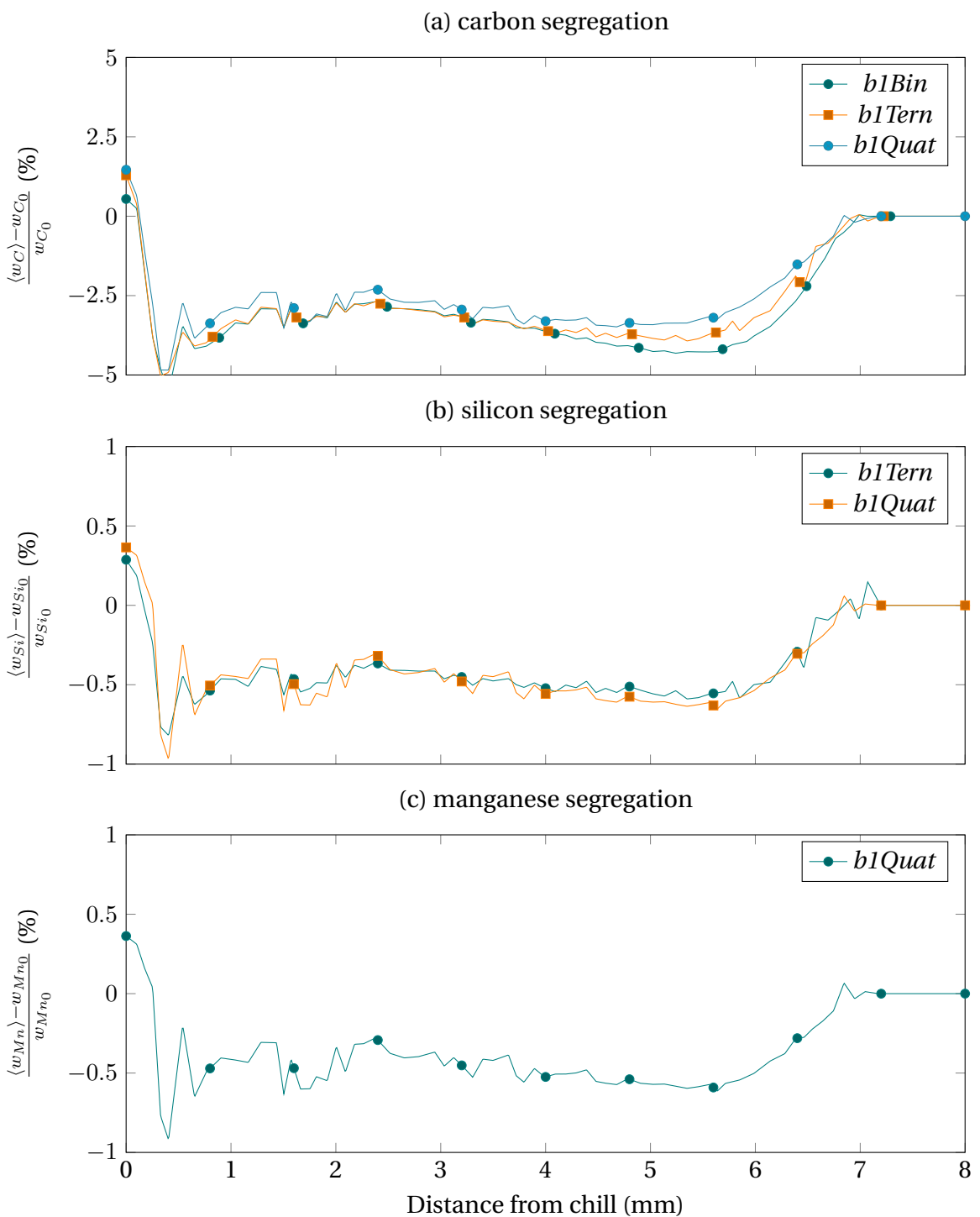


Fig. 5.44 – Relative mesosegregation profiles as functions of the distance from the chill, plotted for (a) carbon (b) silicon and (c) manganese elements along the vertical revolution axis of the solidified sample.

Résumé chapitre 5

Ce dernier chapitre est dédié à la prise en compte du retrait à la solidification à l'origine de la déformation de la surface libre métal-air, en présence des phénomènes de ségrégation. Pour ce faire, le modèle de solidification utilisé précédemment pour prédire la macroségrégation induite par convection thermosolutale en monodomaine, est enrichi par une méthode de suivi direct d'interface, la level set. Les équations du modèle sont alors reformulées dans un contexte eulérien multidomaine-multiphasé, i.e. où deux domaines multiphases sont séparés par une interface mobile, l'aspect multiphasé dans chaque domaine étant géré par la méthode de prise de moyenne volumique.

Un premier cas d'application 1D est ensuite présenté. C'est un cas qui avait fait l'objet de validation du *Tsolver* dans le chapitre 3, et qui est refait avec des masses volumiques solide et liquide différentes. Cette application simple permet toutefois de comprendre le phénomène de ségrégation inverse résultant de l'écoulement du liquide dans la direction du front de solidification pour compenser la différence des masses volumiques des phases, ce qui enrichit en solutés la partie du métal en contact avec le refroidisseur. Ce phénomène est souvent observé aux surfaces des lingots en contact avec les moules. Des courbes de refroidissement ainsi qu'un bilan de conservation de masse de métal sont présentés pour permettre de comprendre l'effet de l'introduction de la méthode level set sur la physique de la solidification.

La seconde application est aussi un cas de validation utilisé dans un chapitre précédent, issu d'une simulation sans retrait présente dans la littérature [CAROZZANI et al. 2013]. Cependant, le but en est maintenant de tester la robustesse du modèle en présence de convection naturelle, d'origine thermique dans l'air et thermosolutale dans le métal, avec suivi de déformation de l'interface par retrait à la solidification. Nous utilisons une méthode de remaillage adaptatif basée sur la projection sur les arêtes [COUPEZ et HACHEM 2013], permettant d'avoir une résolution de maillage fine autour des zones d'intérêts, notamment l'interface décrite par level set, le vecteur vitesse et la concentration moyenne. Ce couplage de techniques numériques permet de déterminer à la fois, la retassure en surface du lingot et la macroségrégation, présente sous forme de canaux.

Dans le dernier cas, il s'agit de la solidification d'une goutte d'acier en microgravité. Des essais expérimentaux de solidification déclenchée par contact avec un substrat sont présentés avec la forme finale de la goutte. Pour pouvoir prédire la déformation de la goutte en présence de mésoségrégations, nous considérons trois nuances issues du même alliage : un binaire (*b1Bin*) Fe-C, un ternaire (*b1Tern*) Fe-C-Si et finalement un quaternaire (*b1Quat*) Fe-C-Mn-Si. D'abord, une étude paramétrique est faite en se servant de l'alliage binaire, dans le but de déterminer les paramètres optimaux de vitesse de refroidissement et d'accélération gravitationnelle, pour se rapprocher du profil expérimental de la goutte déformée en fin de solidification. Ensuite, nous simulons la solidification de chaque alliage en montrant la déformation finale ainsi que la distribution finale des espèces chimiques.

Bibliography

[Basset 2006]

Basset, O. (2006). "Simulation numérique d'écoulements multi-fluides sur grille de calcul". PhD Thesis. École Nationale Supérieure des Mines de Paris. URL: <https://tel.archives-ouvertes.fr/tel-00376484> (cited on pages 37, 166).

[Beckermann et al. 1999]

Beckermann, C., Diepers, H. J., Steinbach, I., Karma, A., and Tong, X. (1999). "Modeling Melt Convection in Phase-Field Simulations of Solidification". *Journal of Computational Physics*, 154 (2), pp. 468–496. URL: <http://www.sciencedirect.com/science/article/pii/S0021999199963234> (cited on page 32).

[Boettinger et al. 2002]

Boettinger, W. J., Warren, J. A., Beckermann, C., and Karma, A. (2002). "Phase-Field Simulation of Solidification1". *Annual Review of Materials Research*, 32 (1), pp. 163–194. URL: <http://dx.doi.org/10.1146/annurev.matsci.32.101901.155803> (cited on page 30).

[Brackbill et al. 1992]

Brackbill, J. U., Kothe, D. B., and Zemach, C. (1992). "A continuum method for modeling surface tension". *Journal of Computational Physics*, 100 (2), pp. 335–354. URL: <http://www.sciencedirect.com/science/article/pii/002199919290240Y> (cited on page 32).

[Brooks and Hughes 1982]

Brooks, A. N. and Hughes, T. J. R. (1982). "Streamline upwind/Petrov-Galerkin formulations for convection dominated flows with particular emphasis on the incompressible Navier-Stokes equations". *Computer Methods in Applied Mechanics and Engineering*, 32 (1–3), pp. 199–259. URL: <http://www.sciencedirect.com/science/article/pii/0045782582900718> (cited on page 36).

[Carozzani et al. 2013]

Carozzani, T., Gandin, C.-A., Digonnet, H., Bellet, M., Zaidat, K., and Fautrelle, Y. (2013). "Direct Simulation of a Solidification Benchmark Experiment". *Metallurgical and Materials Transactions A*, 44 (2), pp. 873–887. URL: <http://link.springer.com/article/10.1007/s11661-012-1465-1> (cited on page 184).

[Chen et al. 1997]

Chen, S., Merriman, B., Osher, S., and Smereka, P. (1997). "A Simple Level Set Method for Solving Stefan Problems". *Journal of Computational Physics*, 135 (1), pp. 8–29. URL: <http://www.sciencedirect.com/science/article/pii/S0021999197957211> (cited on page 30).

Bibliography

[Chen 2014]

Chen, S. (2014). "Three dimensional Cellular Automaton - Finite Element (CAFE) modeling for the grain structures development in Gas Tungsten / Metal Arc Welding processes". PhD Thesis. Ecole Nationale Supérieure des Mines de Paris. URL: <https://pastel.archives-ouvertes.fr/pastel-01038028> (cited on page 30).

[Clyne and Kurz 1981]

Clyne, T. W. and Kurz, W. (1981). "Solute redistribution during solidification with rapid solid state diffusion". *Metallurgical Transactions A*, 12 (6), pp. 965–971. URL: <http://link.springer.com/article/10.1007/BF02643477> (cited on page 21).

[Combeau et al. 1996]

Combeau, H., Drezet, J.-M., Mo, A., and Rappaz, M. (1996). "Modeling of microsegregation in macrosegregation computations". *Metallurgical and Materials Transactions A*, 27 (8), pp. 2314–2327. URL: <http://link.springer.com/article/10.1007/BF02651886> (cited on page 21).

[Coupez and Hachem 2013]

Coupez, T. and Hachem, E. (2013). "Solution of high-Reynolds incompressible flow with stabilized finite element and adaptive anisotropic meshing". *Computer Methods in Applied Mechanics and Engineering*, 267, pp. 65–85. URL: <http://www.sciencedirect.com/science/article/pii/S0045782513002077> (cited on page 184).

[Coupez 1991]

Coupez, T. (1991). *Grandes transformations et remaillage automatique*. EMP. URL: <http://www.theses.fr/1991ENMP0615> (cited on page 42).

[Coupez 2000]

Coupez, T. (2000). "Génération de maillage et adaptation de maillage par optimisation locale". *Revue Européenne des Éléments*, 9 (4), pp. 403–423. URL: <http://www.tandfonline.com/doi/abs/10.1080/12506559.2000.10511454> (cited on page 42).

[Courtois et al. 2014]

Courtois, M., Carin, M., Masson, P. L., Gaied, S., and Balabane, M. (2014). "A complete model of keyhole and melt pool dynamics to analyze instabilities and collapse during laser welding". *Journal of Laser Applications*, 26 (4), p. 042001. URL: <http://scitation.aip.org/content/jia/journal/jla/26/4/10.2351/1.4886835> (cited on page 31).

[Dantzig and Rappaz 2009]

Dantzig, J. A. and Rappaz, M. (2009). *Solidification*. EPFL Press (cited on pages 21–23, 26, 140).

[Desmaison et al. 2014]

Desmaison, O., Bellet, M., and Guillemot, G. (2014). "A level set approach for the simulation of the multipass hybrid laser/GMA welding process". *Computational Materials Science*, 91, pp. 240–250. URL: <http://www.sciencedirect.com/science/article/pii/S092702561400278X> (cited on page 30).

[Dijkstra 1959]

Dijkstra, E. W. (1959). "A note on two problems in connexion with graphs". *Numerische Mathematik*, 1 (1), pp. 269–271. URL: <http://link.springer.com/article/10.1007/BF01386390> (cited on page 40).

Bibliography

[Du et al. 2001]

Du, Q., Li, D., Li, Y., Li, R., and Zhang, P. (2001). "Simulating a double casting technique using level set method". *Computational Materials Science*, 22 (3–4), pp. 200–212. URL: <http://www.sciencedirect.com/science/article/pii/S0927025601001902> (cited on page 30).

[Ettrich et al. 2014]

Ettrich, J., Choudhury, A., Tschukin, O., Schoof, E., August, A., and Nestler, B. (2014). "Modelling of transient heat conduction with diffuse interface methods". *Modelling and Simulation in Materials Science and Engineering*, 22 (8), p. 085006. URL: <http://iopscience.iop.org/0965-0393/22/8/085006> (cited on page 35).

[Flemings and Nereo 1967]

Flemings, M. C. and Nereo, G. E. (1967). "Macrosegregation: Part I". *Transactions of the Metallurgical Society of AIME*, 239, pp. 1449–1461 (cited on page 134).

[Gada and Sharma 2009]

Gada, V. H. and Sharma, A. (2009). "On Derivation and Physical Interpretation of Level Set Method-Based Equations for Two-Phase Flow Simulations". *Numerical Heat Transfer, Part B: Fundamentals*, 56 (4), pp. 307–322. URL: <http://dx.doi.org/10.1080/10407790903388258> (cited on page 32).

[Gandin 2014]

Gandin, C.-A. (2014). *Project ESA-MAP CCEMLCC phase #2 – Final Report* (cited on pages 161, 165).

[Gibou et al. 2003]

Gibou, F., Fedkiw, R., Caflisch, R., and Osher, S. (2003). "A Level Set Approach for the Numerical Simulation of Dendritic Growth". *Journal of Scientific Computing*, 19 (1–3), pp. 183–199. URL: <http://link.springer.com/article/10.1023/A%3A1025399807998> (cited on page 30).

[Gruau and Coupez 2005]

Gruau, C. and Coupez, T. (2005). "3D tetrahedral, unstructured and anisotropic mesh generation with adaptation to natural and multidomain metric". *Computer Methods in Applied Mechanics and Engineering*, Unstructured Mesh Generation 194 (48–49), pp. 4951–4976. URL: <http://www.sciencedirect.com/science/article/pii/S0045782505000745> (cited on page 42).

[Hachani et al. 2012]

Hachani, L., Saadi, B., Wang, X. D., Nouri, A., Zaidat, K., Belgacem-Bouzida, A., Ayouni-Derouiche, L., Raimondi, G., and Fautrelle, Y. (2012). "Experimental analysis of the solidification of Sn–3 wt.%Pb alloy under natural convection". *International Journal of Heat and Mass Transfer*, 55 (7–8), pp. 1986–1996. URL: <http://www.sciencedirect.com/science/article/pii/S0017931011007009> (cited on pages 153, 155).

[Harlow and Welch 1965]

Harlow, F. H. and Welch, J. E. (1965). "Numerical Calculation of Time-Dependent Viscous Incompressible Flow of Fluid with Free Surface". *Physics of Fluids (1958-1988)*, 8 (12), pp. 2182–2189. URL: <http://scitation.aip.org/content/aip/journal/pof1/8/12/10.1063/1.1761178> (cited on page 30).

[Hebditch and Hunt 1974]

Hebditch, D. J. and Hunt, J. D. (1974). "Observations of ingot macrosegregation on model systems".

Bibliography

Metallurgical Transactions, 5 (7), pp. 1557–1564. URL: <http://link.springer.com/article/10.1007/BF02646326> (cited on page 153).

[Hirt 1971]

Hirt, C. W. (1971). “An arbitrary Lagrangian-Eulerian computing technique”. *Proceedings of the Second International Conference on Numerical Methods in Fluid Dynamics*. Ed. by M. Holt. Lecture Notes in Physics 8. Springer Berlin Heidelberg, pp. 350–355. URL: http://link.springer.com/chapter/10.1007/3-540-05407-3_50 (cited on page 29).

[Hirt and Nichols 1981]

Hirt, C. W and Nichols, B. D (1981). “Volume of fluid (VOF) method for the dynamics of free boundaries”. *Journal of Computational Physics*, 39 (1), pp. 201–225. URL: <http://www.sciencedirect.com/science/article/pii/0021999181901455> (cited on page 30).

[Hysing et al. 2009]

Hysing, S., Turek, S., Kuzmin, D., Parolini, N., Burman, E., Ganesan, S., and Tobiska, L. (2009). “Quantitative benchmark computations of two-dimensional bubble dynamics”. *International Journal for Numerical Methods in Fluids*, 60 (11), pp. 1259–1288. URL: <http://onlinelibrary.wiley.com/doi/10.1002/fld.1934/abstract> (cited on page 37).

[Jannoun 2014]

Jannoun, G. E. (2014). “Space-Time accurate anisotropic adaptation and stabilized finite element methods for the resolution of unsteady CFD problems”. PhD thesis. Ecole Nationale Supérieure des Mines de Paris. URL: <https://pastel.archives-ouvertes.fr/tel-01146245/document> (cited on page 42).

[Karma and Rappel 1996]

Karma, A. and Rappel, W.-J. (1996). “Phase-field method for computationally efficient modeling of solidification with arbitrary interface kinetics”. *Physical Review E*, 53 (4), R3017–R3020. URL: <http://link.aps.org/doi/10.1103/PhysRevE.53.R3017> (cited on page 30).

[Khan et al. 2014]

Khan, M. I., Mostafa, A. O., Aljarrah, M., Essadiqi, E., and Medraj, M. (2014). “Influence of Cooling Rate on Microsegregation Behavior of Magnesium Alloys”. *Journal of Materials*, 2014, e657647. URL: <http://www.hindawi.com/journals/jma/2014/657647/abs/> (cited on page 21).

[Kobayashi 1988]

Kobayashi, S. (1988). “Solute redistribution during solidification with diffusion in solid phase: A theoretical analysis”. *Journal of Crystal Growth*, 88 (1), pp. 87–96. URL: <http://www.sciencedirect.com/science/article/pii/S0022024898900100> (cited on page 21).

[Maitre 2006]

Maitre, E. (2006). “Review of numerical methods for free interfaces”. Les Houches, France. URL: <http://goo.gl/Re6f3a> (cited on page 30).

[Martorano et al. 2003]

Martorano, M. A., Beckermann, C., and Gandin, C.-A. (2003). “A solutal interaction mechanism for the columnar-to-equiaxed transition in alloy solidification”. *Metallurgical and Materials Transactions A*, 34 (8), pp. 1657–1674. URL: <http://link.springer.com/article/10.1007/s11661-003-0311-x> (cited on page 21).

[Ni and Beckermann 1991]

Ni, J. and Beckermann, C. (1991). "A volume-averaged two-phase model for transport phenomena during solidification". *Metallurgical Transactions B*, 22 (3), pp. 349–361. URL: <http://link.springer.com/article/10.1007/BF02651234> (cited on pages 21, 22, 24).

[Onodera and Arakida 1959]

Onodera, S. and Arakida, Y. (1959). "Effect of Gravity on the Macro-Segregation of Larger Steel Ingots", pp. 358–368. URL: <http://eprints.nmlindia.org/3079/1/358-368.PDF> (cited on page 119).

[Osher and Fedkiw 2003]

Osher, S. and Fedkiw, R. (2003). "Signed Distance Functions". *Level Set Methods and Dynamic Implicit Surfaces*. Applied Mathematical Sciences 153. Springer New York, pp. 17–22. URL: http://link.springer.com/chapter/10.1007/0-387-22746-6_2 (cited on page 41).

[Osher and Sethian 1988]

Osher, S. and Sethian, J. A. (1988). "Fronts propagating with curvature-dependent speed: Algorithms based on Hamilton-Jacobi formulations". *Journal of Computational Physics*, 79 (1), pp. 12–49. URL: <http://www.sciencedirect.com/science/article/pii/0021999188900022> (cited on pages 30, 31).

[Peng et al. 1999]

Peng, D., Merriman, B., Osher, S., Zhao, H., and Kang, M. (1999). "A PDE-Based Fast Local Level Set Method". *Journal of Computational Physics*, 155 (2), pp. 410–438. URL: <http://www.sciencedirect.com/science/article/pii/S0021999199963453> (cited on pages 33, 39).

[Prosperetti 2002]

Prosperetti, A. (2002). "Navier-Stokes Numerical Algorithms for Free-Surface Flow Computations: An Overview". *Drop-Surface Interactions*. Ed. by M. Rein. CISM International Centre for Mechanical Sciences 456. Springer Vienna, pp. 237–257. URL: http://link.springer.com/chapter/10.1007/978-3-7091-2594-6_8 (cited on page 30).

[Rappaz et al. 2003]

Rappaz, M., Bellet, M., and Deville, M. (2003). *Numerical Modeling in Materials Science and Engineering*. Springer Series in Computational Mathematics. Springer Berlin Heidelberg (cited on page 121).

[Rivaux 2011]

Rivaux, B. (2011). "Simulation 3D éléments finis des macroségrégations en peau induites par déformations thermomécaniques lors de la solidification d'alliages métalliques". PhD Thesis. École Nationale Supérieure des Mines de Paris. URL: <http://pastel.archives-ouvertes.fr/pastel-00637168> (cited on page 163).

[Sethian 1996]

Sethian, J. A. (1996). "A fast marching level set method for monotonically advancing fronts". *Proceedings of the National Academy of Sciences*, 93 (4), pp. 1591–1595. URL: <http://www.pnas.org/content/93/4/1591> (cited on page 40).

[Shakoor et al. 2015]

Shakoor, M., Scholtes, B., Bouchard, P.-O., and Bernacki, M. (2015). "An efficient and parallel level

Bibliography

set reinitialization method - Application to micromechanics and microstructural evolutions". *Applied Mathematical Modelling (submitted)*, (cited on page 41).

[Stratos et al. 2008]

Stratos, G., Gavaises, M., Theodorakakos, A., and Bergeles, G. (2008). "Numerical investigation of the cooling effectiveness of a droplet impinging on a heated surface". *International Journal of Heat and Mass Transfer*, 51 (19–20), pp. 4728–4742. URL: <http://www.sciencedirect.com/science/article/pii/S001793100800149X> (cited on page 35).

[Sun and Beckermann 2004]

Sun, Y. and Beckermann, C. (2004). "Diffuse interface modeling of two-phase flows based on averaging: mass and momentum equations". *Physica D: Nonlinear Phenomena*, 198 (3–4), pp. 281–308. URL: <http://www.sciencedirect.com/science/article/pii/S0167278904003689> (cited on page 32).

[Sussman et al. 1994]

Sussman, M., Smereka, P., and Osher, S. (1994). "A Level Set Approach for Computing Solutions to Incompressible Two-Phase Flow". *Journal of Computational Physics*, 114 (1), pp. 146–159. URL: <http://www.sciencedirect.com/science/article/pii/S0021999184711557> (cited on pages 37–39).

[Tan and Zabaras 2007]

Tan, L. and Zabaras, N. (2007). "A level set simulation of dendritic solidification of multi-component alloys". *Journal of Computational Physics*, 221 (1), pp. 9–40. URL: <http://www.sciencedirect.com/science/article/pii/S0021999106002737> (cited on page 30).

[Tourret and Gandin 2009]

Tourret, D. and Gandin, C. A. (2009). "A generalized segregation model for concurrent dendritic, peritectic and eutectic solidification". *Acta Materialia*, 57 (7), pp. 2066–2079. URL: <http://www.sciencedirect.com/science/article/pii/S1359645409000184> (cited on page 21).

[Vigneaux 2007]

Vigneaux, P. (2007). "Méthodes Level Set pour des problèmes d'interface en microfluidique". PhD thesis. Université Sciences et Technologies - Bordeaux I. URL: <https://tel.archives-ouvertes.fr/tel-00189409/document> (cited on page 40).

[Ville et al. 2011]

Ville, L., Silva, L., and Coupez, T. (2011). "Convected level set method for the numerical simulation of fluid buckling". *International Journal for Numerical Methods in Fluids*, 66 (3), pp. 324–344. URL: <http://onlinelibrary.wiley.com/doi/10.1002/fld.2259/abstract> (cited on page 39).

[Voller et al. 1989]

Voller, V. R., Brent, A. D., and Prakash, C. (1989). "The modelling of heat, mass and solute transport in solidification systems". *International Journal of Heat and Mass Transfer*, 32 (9), pp. 1719–1731. URL: <http://www.sciencedirect.com/science/article/pii/0017931089900549> (cited on page 125).

[Wang and Beckermann 1993]

Wang, C. Y. and Beckermann, C. (1993). "A multiphase solute diffusion model for dendritic alloy solidification". *Metallurgical Transactions A*, 24 (12), pp. 2787–2802. URL: <http://link.springer.com/article/10.1007/BF02659502> (cited on page 21).